



HAL
open science

Coherent light sources with spin-polarized current

Tibor Fördös

► **To cite this version:**

Tibor Fördös. Coherent light sources with spin-polarized current. Optics [physics.optics]. Université Paris Saclay (COMUE); VŠB - Technical University of Ostrava, 2018. English. NNT: 2018SACLX043 . tel-01905188

HAL Id: tel-01905188

<https://pastel.hal.science/tel-01905188>

Submitted on 25 Oct 2018

HAL is a multi-disciplinary open access archive for the deposit and dissemination of scientific research documents, whether they are published or not. The documents may come from teaching and research institutions in France or abroad, or from public or private research centers.

L'archive ouverte pluridisciplinaire **HAL**, est destinée au dépôt et à la diffusion de documents scientifiques de niveau recherche, publiés ou non, émanant des établissements d'enseignement et de recherche français ou étrangers, des laboratoires publics ou privés.



Coherent light sources with spin-polarized current

Thèse de doctorat de l'Université Paris-Saclay
et de VŠB - Technical University of Ostrava
préparée à École Polytechnique

École doctorale n°573 Interfaces
Spécialité de doctorat: Physique

Thèse présentée et soutenue à Palaiseau, le 10/07/2018, par

TIBOR FÖRDÖS

Composition du Jury :

Jaromír Pištora Professeur, VŠB - TUO	Président
Mike Adams Professeur, University of Essex	Rapporteur
Josef Humlíček Professeur, Masaryk University	Rapporteur
Razvigor Ossikovski Professeur, École Polytechnique	Examineur
Henri-Jean Drouhin Professeur, École Polytechnique	Directeur de thèse
Kamil Postava Professeur agrégé, VŠB - TUO	Directeur de thèse
Henri Jaffrès Chargé de Recherche, CNRS	Co-directeur de thèse

Title : Coherent light sources with spin polarized current

Keywords : spin-lasers, VCSELs, Mueller matrix ellipsometry

Résumé : Spin-lasers are semiconductor devices in which the radiative recombination processes involving spin-polarized carriers result in an emission of circularly polarized photons. Nevertheless, additional linear in-plane anisotropies in the cavity generally lead in preferential linearly-polarized laser emission and to possible coupling between modes. In this thesis, a general method for the modeling of semiconductor laser such as vertical-(external)-cavity surface-emitting laser containing multiple quantum wells and involving anisotropies that may reveal *i)* a local linear birefringence due to the strain field at the surface or *ii)* a birefringence in quantum wells (QWs) due to phase amplitude coupling originating from the reduction of the biaxial D_{2d} to the C_{2v} symmetry group at the III-V ternary semiconductor interfaces. A novel scattering S-matrix recursive method is implemented using a gain tensor derived analytically from the Maxwell-Bloch equations. It enables to model the properties of

the emission (threshold, polarization, mode splitting) from the laser with multiple quantum well active zones by searching for the resonant eigenmodes of the cavity. The method is demonstrated on real laser structures and is used for the extraction of optical permittivity tensors of surface strain and quantum wells in agreement with experiments. The method is generalized to find the laser eigenmodes in the most general case of circular polarized pumps (unbalance between the spin-up and spin-down channels) and linear gain dichroism. In addition, the measurement of full 4×4 Mueller matrix for multiple angles of incidence and in-plane azimuthal angles has been used for extraction of optical permittivity tensors of surface strained layers and quantum wells. Such spectral dependence of optical tensor elements are crucial for modeling of spin-laser eigenmodes, resonance conditions, and also for understanding of sources of structure anisotropies.

Titre : Světelné koherentní zdroje se spinově polarizovaným proudem

Klíčová slova : spinové lasery, VCSELs, ellipsometrie Muellerových matic

Abstrakt : Spinové lasery jsou polovodičové zařízení v nichž zářivé přechody zahrnující spin nosičů vedou k emisi kruhově polarizovaných fotonů. Lokální anisotropie přítomné v rezonátoru však ovlivňují výslednou polarizaci a vedou k emisi lineárních nebo elipticky polarizovaných vlastních módů a k případné vazbě mezi nimi. V této práci je popsána obecná metoda modelování povrchově emitujících polovodičových laserů s vertikální geometrií zahrnující vícenásobné kvantové jámy a přítomné lokální anisotropie: *i)* lineární dvojlom a dichroismus na povrchu *ii)* anisotropie v kvantových jamách pocházející z fázově-amplitudové vazby vzhledem k redukci D_{2d} symetrie na C_{2v} symetrii na rozhraní III-V ternárních polovodičů. Nová metoda zahrnující S-maticový přístup a využívající tenzor zesílení odvozený z Maxwell-

Blochových rovnic umožňuje modelování vlastností spinového laseru (laserový práh, vyzářenou polarizaci, frekvenční rozestup módů) s vícenásobnými aktivními oblastmi. Metoda je demonstrována na příkladu reálné laserové struktury a je využita pro výpočet lokálních optických tenzorů permitivity na povrchu a v kvantových jamách. Metoda je dále zobecněna pro popis spinových laserů s elektrickým a optickým čerpáním a s lineárním dichroismem v zesílení. Pro výpočet anizotropních optických konstant bylo využito měření 4×4 Muellerovy matice pro různé úhly dopadu a různé azimutální úhly. Spektrální závislost optických konstant je klíčová pro modelování vlastních módů, podmínek rezonance a také pro pochopení rozdílných zdrojů anizotropie v laserových strukturách.



Acknowledgments

This PhD thesis has been carried out at École Polytechnique, Université Paris-Saclay and Technical University of Ostrava within the co-tutelle collaboration. I have had the pleasure of working alongside enthusiastic and friendly advisors and colleagues.

I am heartily thankful to my czech supervisor assoc. prof. Kamil Postava from Technical University of Ostrava, whose support and guidance enabled me to develop an understanding of this interesting part of physics. I owe my deepest gratitude to my french supervisors, prof. Henri-Jean Drouhin and Dr. Henri Jaffrès. You let me shape and sculpt my PhD project while providing wisdom, support, and guidance along the way. It has been a privilege to work with you. I am also grateful to prof. Pištora for including me in his research group and for financial supports from his research grants.

I would also like to thank my thesis committee members, prof. Mike Adams, prof. Michael Oestreich, and prof. Josef Humlíček for reviewing this thesis.

I feel extremely fortunate to be surrounded by so many friends. Zuzana, Jaroslav, Radek, Ondra, Huong, Giuseppe, Ikbal, Yen, and Benjamin helped me make my doctoral studies enjoyable. Above all, thank to my family, especially to my parents and my wife. Thank you Maja for your love and support. I am extremely fortunate to have you in my life and I look forward to sharing whatever is to come.

Declaration

I declare I elaborated this thesis by myself. All literary sources and publications I have used had been cited.

Contents

1	Introduction	3
1.1	The rise of semiconductor spin-lasers	3
1.2	Goal and motivation of thesis	6
1.3	Organisation of the thesis	8
2	Basic principles of spin vertical-cavity surface-emitting lasers and diodes	11
2.1	Conversion of spin state to polarization state of light	11
2.2	Spin injection into semiconductor: Pumping methods	13
2.2.1	Electrical pumping	13
2.2.2	Optical pumping	14
2.3	Design of the V(E)CSEL structure	17
2.4	Linear birefringence and circular gain dichroism	18
2.5	Conclusion of the chapter	23
3	Polarization state of light: Focus on ellipsometry of multilayer semiconductor lasers	25
3.1	Electromagnetic response of anisotropic structure	25
3.1.1	Electromagnetic field equations in anisotropic media	25
3.1.2	Wave equation	27
3.1.3	Plane electromagnetic wave in isotropic medium	28
3.1.4	Plane electromagnetic wave in anisotropic medium	29
3.1.5	Materials characteristics	29
3.1.6	Polarization states of light: Jones and Stokes vectors	31
3.1.7	Jones and Stokes-Mueller formalism	34
3.2	Electromagnetic field in anisotropic multilayer structure	37
3.2.1	Solution of the Maxwell equation in anisotropic medium	37
3.2.2	Boundary conditions at interfaces	38
3.2.3	Scattering matrix formalism	41
3.2.4	Reflection coefficients	41
3.2.5	Reflection coefficients with local anisotropic layers	42
3.2.6	Ellipsometric angles	44
3.3	Mueller matrix ellipsometry	45

3.3.1	Comparison of Mueller matrix ellipsometry with reflectance anisotropy spectroscopy (RAS)	45
3.3.2	Comparison of Mueller matrix ellipsometry with standard spectroscopic ellipsometry	47
3.4	Conclusion of the chapter	48
4	Experimental study of surface and interfacial optical anisotropy	49
4.0.1	Experimental setup	49
4.1	Sample description	50
4.2	Optical function of semiconductor layers	50
4.3	Fitting procedure and figure of merit	52
4.4	Results	54
4.5	Conclusion of the chapter	58
5	Theoretical and numerical techniques for the analysis of eigenmodes of spin-VECSELs with local linear birefringence and gain dichroism	61
5.1	Recent mathematical description: The 2×2 Jones matrix analysis of spin-VECSEL	62
5.2	Physics of spin-pumped gain medium with linear birefringence	65
5.2.1	Maxwell-Bloch Equations	65
5.2.2	Generalized Maxwell-Bloch Equations	69
5.2.3	Derivation of the optical gain including linear anisotropies	72
5.2.4	Source of linear birefringence in the optical cavity	77
5.3	Generalization for emission from multilayer spin-laser and spin-LED	78
5.3.1	Description of the optical gain in multilayers	78
5.3.2	Transfer and scattering matrix formalism for anisotropic cavity	79
5.3.3	Generalization to emission from multiple QW: Recursive formulas for multiple active QW regions	82
5.4	Conclusion of the chapter	83
6	Application of formalism to the real 1/2 (spin-) VECSELs and spin-LEDs	85
6.1	Model of realistic single-source spin-LED	85
6.2	Emission from 1/2-VECSELs structures with linear birefringence and gain dichroism: model vs. experiments	89
6.2.1	Main physical issues: From a single source to multiple QWs recursion	89
6.2.2	Modeling real VECSELs involving linear anisotropies.	91
6.3	Case of the circular pumps with local linear anisotropies	97
6.3.1	Effect of surface strain and polarization degree spin-injected current	97

6.3.2	Effect of linear gain dichroism and polarization degree spin-injected current	98
A	Lamb's model	111
B	Transfer matrix formalism for multilayer lasers and LED	113
C	Scattering matrix formalism for multilayer lasers and LED	115
D	Recursive calculation of the effective gain tensor	117

List of Figures

1.1	a) Monolithic VCSEL consists of distributed Bragg mirrors (DBR), which plays the role of mirrors. The active region, usually quantum wells (QWs) [17, 18] or quantum dots (QDs) [19, 20], are responsible for the emission of coherent light through electron-hole recombination [18]. Figure reprinted from [18]. b) The VECSEL configuration with an external cavity.	5
2.1	Selection rules in a) direct bulk semiconductor and (b) 2D quantum system [3, 17].	13
2.2	Concept of the optically-pumped VECSEL.	15
2.3	a) Lasing emission spectra of two orthogonal circular components, σ^+ and σ^- , from a VCSEL excited with σ^+ circularly polarized pump pulses. Figure reprinted from Ref. 24. b) Emission vs pump intensity for the determination of the VCSEL threshold intensity. Figure reprinted from Ref. 57.	16
2.4	The bucket model for a) conventional laser b) spin-laser proposed by Zutic <i>et al.</i> [55, 56].	17
2.5	Schematic description of the 1/2-VCSEL structure dedicated to the optical pumping.	17
2.6	Dependence of the Bragg mirror reflectivity on the incident wavelength for two different number of periods.	19
2.7	Origin of the natural interface asymmetry [59].	21
2.8	The surface reconstruction with its characteristic dimer-configuration and back-bonds.	22
2.9	Shift of emission spectrum at positive and negative applied voltages. Figure extracted from Ref. 68.	23
2.10	Experimental setup of the birefringence measurement. Figure extracted from Ref. 70.	24
3.1	Orthogonal orientation of \mathbf{E} , \mathbf{H} , and \mathbf{k} vectors of the plane wave in an isotropic medium.	29
3.2	The polarization state of light described by the azimuth θ and the ellipticity ϵ of the polarization ellipse.	33

3.3	The three Stokes vector components (S_1, S_2, S_3) are the Cartesian coordinates of the point on the Poincaré sphere (of unit radius) (w_1, w_2, w_3) = ($\cos 2\epsilon \cos 2\theta, \cos 2\epsilon \sin 2\theta, \sin 2\epsilon$). Points on the Poincaré sphere representing linearly (LP) and right circularly (RCP) polarized light are marked with black points.	34
3.4	The electric field of s -polarization is oriented perpendicularly to the plane of incidence, while p -polarization lies in the plane of incidence.	35
3.5	Multilayer structure embedded in isotropic halfspaces (0) and ($N + 1$). Each layer is characterized by the permittivity tensor $\hat{\epsilon}^{(n)}$ and the thickness $d^{(n)}$	39
3.6	Transfer matrix relates the proper polarization fields of amplitudes $A_j^{(n)}$ in the layer (n) and ($n + 1$).	40
3.7	Comparison between the transfer matrix and the scattering matrix formalism.	42
4.1	Configuration of the experimental measurement: light source (S), polarizer (P), dual-rotating compensator (RC), analyzer (A), and detector (D).	50
4.2	Schematic description of studied VECSEL structure.	50
4.3	Schematic of a single unbroadened CP structure in the Herzinger-Johs model.	52
4.4	Model of the bandgap and M_0 critical point of GaAs by using Herzinger-Johs and Tauc-Lorentz oscillators. Blue and red circles correspond to tabulated data, black solid curves describe model and grey solid curves correspond to model oscillators.	53
4.5	Measured and modeled Mueller matrix element spectra. The angle of incidence of $\theta^{(0)} = 40^\circ$ has been chosen.	54
4.6	The measured Mueller matrix elements as a function of the in-plane azimuth rotation angle ranging from 0 to 360 degrees for $E = 2.2$ eV and for the angle of incidence $\theta^{(0)} = 40^\circ$	55
4.7	a) The ordinary (blue curve) and extraordinary (red curve) optical constants and b) the permittivity differences of real $\Delta\epsilon_1$ and imaginary $\Delta\epsilon_2$ parts of GaAs	56
4.8	a) The ordinary (blue curve) and extraordinary (red curve) optical constants and b) the permittivity differences of real $\Delta\epsilon_1$ and imaginary $\Delta\epsilon_2$ parts of AlAs.	57
4.9	a) The ordinary (blue curve) and extraordinary (red curve) optical constants and b) the permittivity differences of real $\Delta\epsilon_1$ and imaginary $\Delta\epsilon_2$ parts of InGaAs quantum wells.	58
4.10	Electronic energy-band structure of GaAs calculated by density function theory (DFT) using Wien2K. The main interband transitions are indicated by the vertical arrows.	59
5.1	Schematic representation of the simplified laser cavity.	63
5.2	Evolution of the polarization state and the frequency detuning [33, 44].	65

5.3	The relaxation and pumping of a two-level system.	68
5.4	Scheme of the quantum well and barrier system with crystal axes. . .	70
5.5	Scheme of the two orthogonal laser eigenmodes $\boldsymbol{\eta}_{1,2}$ and dipolar source vectors \mathbf{A}_{\pm}^d . The dipolar source vectors are not necessarily orthogonal to each other depending on the dichroism into play. The non-orthogonality between \mathbf{A}_{\pm}^d is at the origin of a strong mode-coupling as discussed in the text.	74
5.6	Schematic description of the structure with a single active layer showing wave propagation inside the cavity.	78
5.7	Sketch of the phase matching in a 1/2 VCSEL structure involving multiple reflection, propagation, and amplification processes in the optical semiconductor cavity containing one effective active layer, the properties of which are derived by recursive method. \mathbf{S}_{du} and \mathbf{S}_{ud} correspond to propagation and reflection effects with respective N (top) and M (bottom) reflections processes. \mathbf{T}_{ud} and \mathbf{T}_{du} represent reflection after amplification in the effective active zone whereas \mathbf{T}_{uu} and \mathbf{T}_{dd} correspond to forward amplification.	81
6.1	Modeled spin-structure shown schematically including the gold capping layer (Au), magneto-optical spin-injector (Co), tunnel barrier (MgO), active layer GaAs with an active plane in the center and Bragg structure AlAs/InGaAs.	86
6.2	The effect of the electron spin polarization. Subplots show emission pattern for varying injected spin polarization $\mathcal{P}_s = 1$ (a), $\mathcal{P}_s = 0.5$ (b), and $\mathcal{P}_s = 0$ (c) with the magnetization of Co layer oriented in the $+z$ direction. Subplots d), e), and f) show emission pattern for varying injected spin polarization $\mathcal{P}_s = 0$, $\mathcal{P}_s = -0.5$ and $\mathcal{P}_s = -1$, respectively, with the magnetization of Co layer oriented in the $-z$ direction. . . .	87
6.3	The effect of the electron spin polarization in the case of the heavy hole transitions. Subplots show emission pattern for varying injected spin polarization $\mathcal{P}_s = 1$, $\mathcal{P}_s = 0.5$, and $\mathcal{P}_s = 0$ with the magnetization of Co layer oriented in the $+z$ direction.	88
6.4	Effect of thickness $d^{(n)} = d_{GaAs}$ in the case of the hh transitions. Subplot a) $d_{GaAs} = 4\lambda/n_{GaAs}$ and subplot b) $d_{GaAs} = 8\lambda/n_{GaAs}$	88
6.5	Sketch and geometry of the 1/2-VCSEL devices investigated in this study showing 1/2-VCSEL structure as the gain mirror, the optical pumping system, and the stable plano-concave-type optical cavity (air gap $L_c = 7.5$ mm) [70, 133, 134].	90
6.6	Description of the 1/2-VECSEL structures under study a) without (S1, left) and b) with (S2, right) the moderately reflective Bragg mirror. S1 is composed of an antireflection coating at the surface. . .	92

6.7	Experimental birefringence measurement, via orthogonal E-field polarization mode beating on a low noise photodiode with a laser beam passing through a polarizer rotated at 45° from $[110]$ axis: an example of measured RF-spectrum, obtained with Sample 1 in a 7.5 mm long cavity and a concave output coupler with $T = 0.7\%$. The absence of the peak in the red dashed curve, confirms that the observed beat note is due the orthogonal polarization mode [70].	92
6.8	Calculation of the resonance conditions of Sample 2 for two linearly polarized eigenmodes oriented along the $[110]$ and $[\bar{1}\bar{1}0]$ direction and $\Delta\varepsilon_s = 0.02$. Δ was taken equal to 0.95.	93
6.9	a) Calculation of multimode emission and mode splitting for $\Delta\varepsilon_{QW} = 0$ (solid blue line) and $\Delta\varepsilon_{QW} = 0.05$ (dashed red line with peak doublets), respectively, inside the QW of Sample 1. b) Calculation of mode splitting inside the QW of Sample 1. The solid blue curve ($\Delta f = 359$ MHz) and the dashed red curve ($\Delta f = 195$ MHz) describe the resonance conditions for models with and without off-diagonal elements \mathbf{T}_{du} and \mathbf{T}_{ud} , respectively.	95
6.10	Dependence of Δf between two orthogonal linear polarizations on linear gain dichroism Δ and surface anisotropy $\Delta\varepsilon_s$ of a) S1 and b) S2. 96	
6.11	Dependence of the Stokes vector components of two eigenmodes (with subscripts a and b) on the spin polarization \mathcal{P}_s and surface anisotropy $\Delta\varepsilon_s$ for $\alpha = 0$	99
6.12	a) Dependence of the frequency shift Δf on the the spin polarization \mathcal{P}_s and surface anisotropy $\Delta\varepsilon_s$ for $\alpha = 0$. In the region with linear eigen polarizations, both modes oscillate with different frequencies. On the other hand, circularly polarized eigenmodes are fully degenerated and oscillate with the same frequency. b) Scheme of the evolution of the output polarization state.	100
6.13	Dependence of the Stokes vector components and the spin polarization \mathcal{P}_s and surface anisotropy $\Delta\varepsilon_s$ for $\alpha = 1.5$	101
6.14	Dependence of the frequency shift Δf on the the spin polarization \mathcal{P}_s and surface anisotropy $\Delta\varepsilon_s$ for $\alpha = 1.5$	102
6.15	Dependence of the Stokes vector components on the linear gain dichroism Δ and the spin polarization \mathcal{P}_s	102
A.1	The evolution of the two eigenstates intensities as a function of the normalized gain dichroism for four values of the constant \mathcal{C} : 0, 0.3, 0.6, and 0.9.	112
D.1	Schematic description of the application of the recursive formula. . .	117

Résumé

Les spin-lasers sont des dispositifs semi-conducteurs dans lesquels les processus de recombinaison radiative impliquant des porteurs polarisés en spin résultent en une émission de photons polarisés circulairement. L'ajout du degré de liberté de spin fournit de nouveaux effets et de nouvelles fonctionnalités. Cela ouvre de nouveaux horizons à des dispositifs modernes combinant les propriétés de l'électronique mainstream à base de charges avec des processus dépendant du spin. De tels dispositifs émetteurs de lumière à commande de spin offrent de nombreux avantages aux futurs systèmes de communication optique tels que des interconnexions optiques reconfigurables pilotées par spin, une dynamique de modulation rapide, une commande de polarisation ainsi que des performances plus élevées, par exemple une réduction du seuil laser, une intensité laser améliorée et une stabilité de polarisation. D'un point de vue technologique, les lasers à géométrie verticale à semi-conducteurs III-V optiquement actifs sont considérés comme de bons candidats pour les dispositifs hautement implémentables à température ambiante. Dans de tels dispositifs, la propagation optique est normale à la surface du substrat et le gain est fourni par plusieurs puits quantiques pris en sandwich dans la cavité optique.

Néanmoins, des anisotropies linéaires supplémentaires dans la cavité conduisent généralement à une émission laser préférentiellement polarisée linéairement et à un éventuel couplage entre modes. Dans cette thèse, une méthode générale pour la modélisation de lasers à semi-conducteurs tels que le laser à surface verticale (externe) à cavité contenant des puits quantiques multiples et impliquant des anisotropies pouvant révéler (i) une biréfringence linéaire locale due au champ de déformation à la surface ou (ii) une biréfringence dans les puits quantiques due au couplage d'amplitude de phase provenant de la réduction de la symétrie D_{2d} biaxiale au groupe de symétrie C_{2v} aux interfaces semi-conductrices ternaires III-V. Pour les raisons mentionnées ci-dessus, une modélisation précise de l'émission et de la propagation de la lumière dans la structure active multicouche avec des anisotropies locales est requise. L'objectif principal de la thèse est de modéliser les propriétés optiques du rayonnement électromagnétique émis par les structures multicouches spin-LED et spin-VCSEL. L'approche proposée est basée sur deux étapes: (i) la représentation des couches de puits quantiques actives avec des sources dipolaires et (ii) la modélisation de la propagation de la lumière dans des structures multicouches résonantes en utilisant une approche matricielle appropriée respectant les équations de Maxwell dans chaque couche et les conditions aux limites aux interfaces.

Une nouvelle méthode récursive à matrices S de diffusion est mise en oeuvre

en utilisant un tenseur de gain calculé analytiquement à partir des équations de Maxwell-Bloch. Il permet de modéliser les propriétés de l'émission (seuil, polarisation, dédoublement de mode) du laser avec plusieurs zones actives à puits quantiques en recherchant les modes propres résonnants de la cavité. La méthode est validée sur des structures laser réelles et est utilisée pour l'extraction de tenseurs de permittivité optique de déformation de surface et de puits quantiques en accord avec des données expérimentales. La méthode est généralisée pour trouver les modes propres du laser dans le cas le plus général de pompes polarisées circulaires (déséquilibre entre les canaux de spin-up et de spin-down) et le dichroïsme à gain linéaire. De plus, la mesure de la matrice de Mueller 4×4 complète pour des angles d'incidence multiples et des angles azimutaux dans le plan a été utilisée pour l'extraction de tenseurs de permittivité optique de couches contraintes superficielles et de puits quantiques. Une telle dépendance spectrale des éléments tensoriels optiques est cruciale pour la modélisation des modes propres du laser à spin, des conditions de résonance, et aussi pour la compréhension des sources d'anisotropies de structure. L'ellipsométrie matricielle de Mueller est présentée comme la technique de choix pour l'étude des anisotropies locales dans les structures semi-conductrices multicouches telles que le 1/2 VCSEL dédié au pompage optique ou électrique.

L'approche proposée dans cette thèse convient au développement futur de la modélisation laser avancée. En particulier, la méthode peut être étendue à la description du comportement dynamique de spin-VCSELs avec plusieurs régions de puits quantiques actifs, y compris la modélisation du champ électrique dépendant du temps dans la cavité décrite par les équations de Maxwell-Bloch. L'une des généralisations les plus prospectives de l'approche repose sur l'implémentation d'une méthode numérique pour le calcul de structures laser avec des supports périodiques tels que des points quantiques, des fils quantiques, des cristaux photoniques et des réseaux.

Chapter 1

Introduction

Spin electronics, also called spintronics, refers to a branch of physics, in which charge and spin of an electron are considered together and not separately as in conventional electronics, which ignores spin. Adding the spin degree of freedom provides new effects and new functionalities. This opens new horizons for modern devices combining properties of mainstream charge-based electronics with spin-dependent phenomena. The perspective of spintronic devices and their application in technology was open in 1988 by Albert Fert and Peter Grunberg [1, 2] by discovering the giant magnetoresistance effect (GMR), which demonstrated the influence of the spin of electrons on the electrical properties in magnetic multilayers composed of alternate ferromagnetic and nonmagnetic layers. In the consecutive years, an intensive research effort in the investigation of spin injection, spin manipulation, and spin detection in metals has been stimulated. Since then, the GMR and more general spintronic effects like tunneling magnetoresistance (TMR) have been applied in hard disk drives, bio-sensors, micro-electro-mechanical systems, and many others. While metal spintronics has already found its role in industry, semiconductor spintronics is yet to demonstrate its full potential, in particular for specific optoelectronic properties like explained in this manuscript.

1.1 The rise of semiconductor spin-lasers

In the past decade, a continuous research effort has been devoted to the physics and development of a novel type of spintronic devices with possibility to control polarization states of emitted light. In such spin-polarized light sources, the radiative recombination of injected spin-polarized carriers results in emission of circularly polarized photons through the quantum optical selection rules [3]. The direct link between the polarization of the injected carriers and the emitted photons makes such spin-polarized sources suitable for many applications. A prerequisite for the realization of such devices has been the development of solid state spin-injectors at room temperature.

The first spin-polarized photoluminescence based on a semiconductor light emitting diode (spin-LED) was proposed by Fiederling *et al.* in 1999 [4]. He demon-

strated a successful high-degree spin injection (90 %) into nonmagnetic bulk GaAs by using a quaternary II-VI magnetic semiconductor $\text{Be}_x\text{Mn}_y\text{Zn}_{1-x-y}\text{Se}$ as a spin-aligner under the application of an external magnetic field along the normal direction of the growth layers at a low-temperature regime. A high degree of injected spin polarization was confirmed by the measurement of the circular polarization state of emitted light. This opened new horizons in a new research field called spin-optoelectronics. In the consecutive years, the spin-LEDs have been used in experimental spintronics for detection and characterization of spin-polarized carriers in a new generation of spintronic structures [4–11].

Achieving an effective spin-polarized electron injection into a semiconductor at room-temperature has been one of the most important challenges in spin-optoelectronics. Significant effort has been made to incorporate ferromagnetic metals in the semiconductor spintronic devices because they offer an effective source of spin-polarized electrons. It has been shown that the obstacle with the conductivity mismatch between the injecting ferromagnetic and receiving semiconductor materials can be overcome by a tunneling mechanism through a barrier [12–14]. In 2003 Habinski *et al.* observed an electron spin polarization of 32% at room-temperature in a GaAs quantum well due to electrical spin injection from Fe/AlGaAs Schottky contact, which provided a natural tunnel barrier between the metal contact and the semiconductor [15]. Two years later in 2005, Jiang *et al.* demonstrated an effective spin injection into AlGaAs/GaAs quantum well system resulting in a high-degree emitted circular polarization (47%) in a room-temperature regime by using CoFe/MgO metal tunnel junction [7]. Unfortunately, all these experiments required an out-of-plane applied external magnetic field due to the natural shape anisotropy of thin ferromagnetic films, which force the in-plane magnetization.

From a technological point of view, the spin-LED devices would be competitive in practical applications only if they operate in a room-temperature regime without the external magnetic field. Several groups have already achieved spin injection into semiconductors using spin injectors with a perpendicular magnetic anisotropy at magnetic remanence. Using both configuration with a Schottky contact and a MgO tunnel contact, respectively, Hovel *et al.* [9] has achieved spin injection at remanence while the maximum degree of circular polarization of the emitted light was 3% at room temperature. The maximal degree of emitted circular polarization (8%) at zero magnetic field has been accomplished by Liang *et al.* by using CoFeB/MgO metal tunnel junction spin-injector on a top of InGaAs/GaAs quantum well system. These types of ultrathin perpendicular spin injectors are of great interest to realize the electrical switching of the injector magnetization owing to the advanced spin-transfer torque properties of the CoFeB layer. Moreover such injector can be directly included in optical cavities for future spin-lasers due to their very low optical absorption loss [16].

Despite all above mentioned results with the spin-LEDs, such devices remain a wonderful tool for characterization and optimization of spin-injection in semiconductor, however, they are limited for practical application for the following reasons. i) A spontaneous emission regime limits the efficiency of spin conversion to emitted

light polarization, which is proportional to the ratio between a carrier recombination time and a spin-lifetime in an active medium. This leads to a low polarization degree of circularly-polarized photons, especially at room-temperature regime with reduced spin-lifetime. ii) Light emission from spin-LED is non-coherent and spatially unfocused with a polarization state, which depends on a direction of emission.

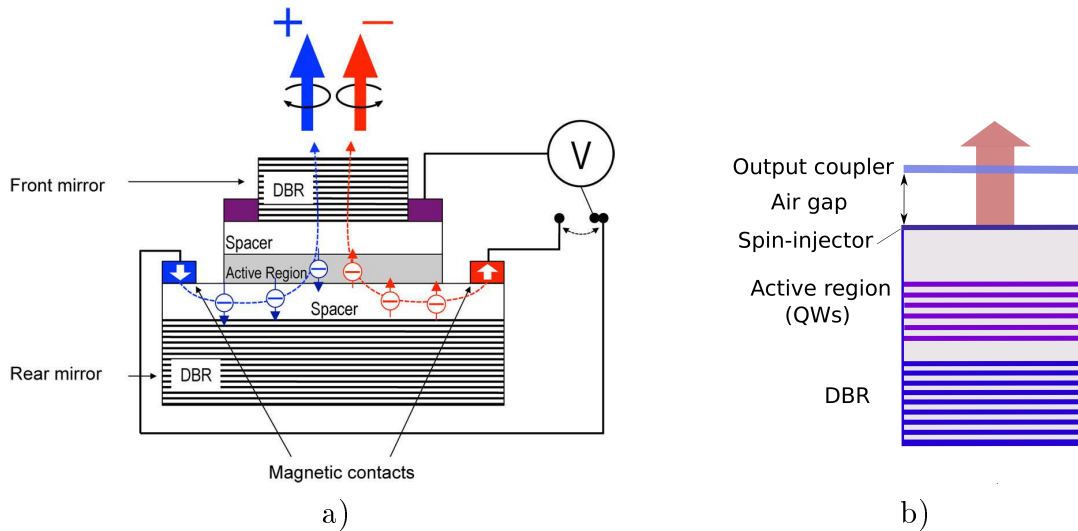


Figure 1.1: a) Monolithic VCSEL consists of distributed Bragg mirrors (DBR), which plays the role of mirrors. The active region, usually quantum wells (QWs) [17, 18] or quantum dots (QDs) [19, 20], are responsible for the emission of coherent light through electron-hole recombination [18]. Figure reprinted from [18]. b) The VECSEL configuration with an external cavity.

All above mentioned limitation can be overcome by combining a proper active medium with a resonant optical cavity leading to the stimulated emission regime. Such spin-laser would lead to a highly-coherent and spatially-focused emission with a high degree of emitted circular polarization even with a relatively low degree of injected spin-polarization due to the amplification effects in the cavity. Therefore maximal conversion efficiency between injected spin and easily switchable output circular polarization can be achieved. Such spin-controlled light-emitting devices provide many advantages for future optical communication systems such as spin driven reconfigurable optical interconnects [21], fast modulation dynamics [22, 23], polarization control [24, 25] as well as higher performances such as laser threshold reduction [26, 27], improved laser intensity, and polarization stability.

From a technological point of view, optically active III-V semiconductors based lasers with vertical geometry (VCSELs) are considered as a good candidates for room-temperature highly-implementable devices. In such devices, the optical propagation is normal to the substrate surface and the gain is provided by several quantum wells sandwiched in the optical cavity. It exists nowadays two kinds of surface-

emitting semiconductor lasers: monolithic micro-cavity-type VCSELs for highly-integrated devices and vertical-external-cavity surface-emitting lasers (VECSEL). Figure 1.1 shows the difference between both types of the laser structures. Monolithic VCSEL consists of distributed Bragg mirrors (DBR), which plays the role of internal mirrors in the resonator. The active region, usually quantum wells (QWs) [17, 18] or quantum dots (QDs) [19, 20, 28], are responsible for the emission of coherent light through electron-hole recombination [18]. Two magnetic contacts are used to achieve spin injection into the active region. In the past decade, spin-operation regime with an electroluminescence of circular polarization of 23% has been demonstrated e.g. by Holub *et al.* [17] with monolithic VCSEL by using electrical pumping in a low-temperature range (50 K). Considering electrical injection, the distance of the spin-injector and active medium plays a crucial role and must be optimized to reduce spin relaxation between injection and recombination. Despite impressive technological effort [17, 19, 20], highly efficient electrical spin-injection in VCSEL at room temperature and magnetic remanence without an external magnetic field remains to be demonstrated.

Alternatively, spin-polarized carriers can be injected optically by using circularly-polarized light [24, 26, 29–31]. In particular, experimental investigations showed that the output circular polarization degree can exceed the input one *via* non-linear gain effects [29]. Figure 1.1b shows vertical-external-cavity surface-emitting laser structure based on 1/2-VCSEL without upper Bragg mirror, which is replaced by high-reflective output coupler [32]. The configuration with the external cavity enables to benefit from an additional degree of freedom provided by the cavity adjustment. For example, it is possible to tune laser parameters by adjusting the cavity length or by adding additional intra-cavity optical components [33, 34]. Moreover, the external cavity of VECSEL enables to deposit an ultra-thin electrical spin-injector perpendicularly-magnetized at magnetic remanence close to the active quantum wells and thus the impact of the spin-relaxation mechanisms occurring during electron transport can be minimized [16]. In addition, the optical pumping is considered as a most effective method to maximize the efficiency of spin-injection into an active medium [29, 33, 34].

1.2 Goal and motivation of thesis

As already mentioned above, in spin-LEDs and spin-lasers, the optical polarization of the emitted photons is directly related to the spin polarization of the carriers through the quantum optical selection rules [3, 35]. Nevertheless, this is not the only factor, which determines the polarization state of the emitted light. The second factor is related to additional in-plane anisotropies in the multilayer semiconductor cavity, which strongly impact the performance and properties of spin-laser operation [36] and lead to complex polarization dynamics. Although the V(E)CSEL geometry exhibits theoretically good isotropic behavior, even a small local anisotropy in a cavity can break this in-plane symmetry and beat the emitted circular polarization result-

ing in preferential linearly-polarized laser emission.

Previous theoretical as well as experimental investigations [37] have allowed to separate between several different contributions: i) a linear birefringence originating from interfaces between ternary quantum wells and barriers (GaAsP/InGaAs/GaAsP), ii) possible local surface strain of III-V material after surface crystalline reconstruction [38, 39], iii) magneto-optical anisotropy originating from magnetized ferromagnetic spin injectors [40]. First contribution, the in-plane optical anisotropy of III-V quantum well structures, was found due to the reduction from D_{2d} to C_{2v} symmetry group when the host materials do not share any common atoms, [38, 39, 41] as well as chemical segregation [38] and strain effect in quantum well. The second contribution originating from the surface may have two different causes: a surface-bulk electro-optic effect due to the appearance of a significant electric field developing from the top surface by pinning of the Fermi level and an effect related to strain by surface reconstruction. [42] The last contribution is given by magneto-optical effects which causes a circular dichroism and birefringence in a magnetized ferromagnetic layer used as a spin-injector.

For the aforementioned reasons, a precise modeling of light emission and propagation in the multilayer active structure with local anisotropies is required. The main goal of the thesis is to model the optical properties of the electromagnetic radiation emitted from spin-LED and spin-VCSEL multilayer structures. It could be based on two steps: (i) representation of active quantum well layers with dipole sources and (ii) modeling of light propagation in resonant multilayer structures by using an appropriate matrix approach fulfilling Maxwell equations in each layer and boundary conditions at the interfaces.

We propose the approach, which (i) describes polarization of emitted photons related to the quantum optical selection rules and consider spin polarization of injected current or generally polarized optical pumping field, (ii) describes the propagation of emitted field in general anisotropic multilayer system consisting of locally anisotropic layers affected by the symmetry reduction on the III-V semiconductor interfaces, surface reconstruction, strain and magneto-optical effects, (iii) correctly defines phases of incoherent spontaneous emission (spin-LED) and coherent stimulated emission (spin-lasers), and (iv) describes the complete polarization state of emitted field from laser structure and conditions for laser resonance. In that mind, new recursive formulas derived in this thesis are used for calculation of the effective active region and enable to include the interference and reflection effects between both active regions together with amplification of multiple reflected light inside the multiple quantum wells (MQWs). Consequently, it enables to model the properties of the emission (threshold, polarization, mode splitting) from the laser with MQW active zones by searching for the resonant eigenmodes of the cavity. The method will be demonstrated on real laser structures and will be used for the extraction of optical permittivity tensors of surface strain and quantum wells in agreement with experiments.

In addition, the Mueller matrix ellipsometry will be applied to study anisotropic multilayer 1/2-VCSEL structure with anisotropic surface and multiple quantum well

region. We demonstrate that both surface and QWs birefringences are the origins of the optical frequency splitting, as observed in semiconductor laser measurement developed in Montpellier by the group of A. Garnache.

1.3 Organisation of the thesis

This thesis is organized as follows.

Chapter 2 introduces basic principles of spin-LED and spin-VCSELs. After a brief introduction of the optical selection rules, we will describe pumping methods, which enable spin injection in semiconductors. Multilayer spin-V(E)CSEL devices will be briefly described together with possible local anisotropies present in the laser structures.

Chapter 3 offers a brief review of the electromagnetic theory for the multilayer anisotropic structures together with the Mueller matrix experimental measurement and modeling of real VECSEL laser structure. After derivation of wave equation for generally anisotropic medium, we show the 4×4 matrix formalism for modeling of electromagnetic response of multilayer anisotropic structures. The change of a polarization state of light due to the local anisotropy is theoretically described using the Jones and the Mueller matrices.

Together with experimental measurements using the Mueller matrix ellipsometry for multiple angles of incidence and in-plane azimuthal angles and in combination with proper parametrization of optical functions, the optical permittivity tensors of surface strained layers and QWs are extracted. The Mueller matrix measurement and analysis are presented in Chapter 4 and have been submitted in the journal *Applied Physics Letters* [43].

Chapter 5 is dedicated to the detailed analysis of a general method for the modeling of semiconductor lasers such as spin-polarized vertical-cavity surface-emitting laser and vertical-external-cavity surface-emitting laser. In the beginning of this chapter we will describe the recent 2×2 Jones matrix analysis of spin-VECSEL developed by Alouini and described in Ref. 44. This simple model can describe evolution of the polarization eigen states in the cavity as a function of the effective linear birefringence and circular gain dichroism induced by the spin injected carriers. However, it is not suitable for description of more complex laser structures with multiple quantum wells (dipolar active sources) inside a cavity and with local anisotropies.

Moreover, the modeling method developed in this work contains description of the amplification processes in multiple quantum wells, multiple reflections, propagation between them, and involving anisotropies that may reveal *i)* a local linear birefringence due to the strain field at the surface or *ii)* a birefringence in quantum wells (QWs) due to phase amplitude coupling originating from the reduction of the biaxial D_{2d} to the C_{2v} symmetry group at the III-V ternary semiconductor interfaces. From a numerical point of view, a novel scattering S-matrix recursive method is implemented using a gain or amplification tensor derived analytically

from the Maxwell-Bloch equations. It enables to model the properties of the emission (threshold, polarization, mode splitting) from the laser with multiple quantum well (MQW) active zones by searching for the resonant eigenmodes of the cavity. The results have been published in the journal *Physical Review A* [37] and in Ref. 45.

Chapter 6 is focused on a numerical and experimental investigation of the local anisotropies in LED and VCSEL cavities. We start with a simple model of multilayer spin-LED structure, which includes magneto-optical spin-injector and we show the effect of magneto-optical effects on an emitted polarization state. Then we will use derived S-matrix recursive formalism for modeling of a frequency splitting and we will compare with experimentally measured values in order to extract anisotropic permittivity tensors of surface layers and quantum wells of a real VCSEL structure. The chapter is completed by numerical simulation of the polarization states of emitted eigenmodes including local anisotropies such as linear gain dichroism and surface strain. The results presented in this chapter have been published in the journal *Journal of Optics* [40].

Chapter 2

Basic principles of spin vertical-cavity surface-emitting lasers and diodes

This chapter introduces basic principles of spin-LED and spin-VCSELs. In the beginning we give a brief introduction of the optical quantum selection rules, which govern an emission from quantum well region. We will describe electrical and optical pumping methods, which enable spin injection in semiconductors. Multilayer spin-V(E)CSEL devices will be briefly described together with possible local anisotropies present in the laser structures. In the end of the chapter we describe an effective measurement method of the anisotropies in the laser structures. Details of VCSEL and V(E)CSEL devices fundamentals and functionalities are given in Coldren textbook [46] and in general review paper in Ref. 47.

2.1 Conversion of spin state to polarization state of light

We give a simple description of the optical selection rules in the dipolar Hamiltonian approximation, well documented in the literature [3, 48], in order to illustrate in the following chapters the power of our technical method to model the properties of light emission from quantum heterostructures. The optical selection rules are found by evaluating the dipole moment of the transition between the conduction band state $|c\rangle$ and the valence band state $|v\rangle$ at the center (Γ -point) of the Brillouin zone (BZ) using the transition matrix element

$$\mathbf{D}_{cv} = \langle c | \hat{\mathbf{D}} | v \rangle, \quad (2.1)$$

where $\hat{\mathbf{D}}$ stands for the dipole moment operator at first order of perturbation. The electronic Bloch states may be expressed as $|\mathbf{J}, m_j\rangle$, where \mathbf{J} denotes the total angular momentum and its projection onto the z axis described by the magnetic quantum number m_j . The conduction band is represented by two different electron

quantum states $|1/2, \pm 1/2\rangle$, while the valence band is represented by two heavy hole states $|1/2, \pm 3/2\rangle$ and two light hole states $|1/2, \pm 1/2\rangle$ in the center of the zone at the Γ_8^+ valley. The quantization axis for the angular momentum is fixed along the photon wavevector \mathbf{k} and the crystal axis of the cubic $A^{III}B^V$ crystal (001) in the z direction. The electron state of the conduction band can be described using the Bloch wave function

$$\psi_{km}^{CB} = u_m^{CB} e^{i\mathbf{k}'\mathbf{r}}, \quad (2.2)$$

where the Bloch amplitudes have the following form

$$u_{1/2}^{CB} = |S \uparrow\rangle, \quad u_{-1/2}^{CB} = |S \downarrow\rangle. \quad (2.3)$$

The $|S\rangle$ denotes the s -type wavefunction and arrows denote spin functions. The Bloch amplitudes of the valence band can be described using the p -type wavefunctions $|X\rangle$, $|Y\rangle$ and $|Z\rangle$ with the symmetry around x , y , and z axes, respectively

$$u_{3/2}^{HH} = -\frac{1}{\sqrt{2}} (|X \uparrow\rangle + i|Y \uparrow\rangle) \quad (2.4)$$

$$u_{-3/2}^{HH} = \frac{1}{\sqrt{2}} (|X \downarrow\rangle - i|Y \downarrow\rangle) \quad (2.5)$$

$$u_{1/2}^{LH} = \frac{1}{\sqrt{3}} \left[-\frac{1}{\sqrt{2}} (|X \downarrow\rangle + i|Y \downarrow\rangle) + \sqrt{2}|Z \uparrow\rangle \right] \quad (2.6)$$

$$u_{-1/2}^{LH} = \frac{1}{\sqrt{3}} \left[\frac{1}{\sqrt{2}} (|X \uparrow\rangle - i|Y \uparrow\rangle) + \sqrt{2}|Z \downarrow\rangle \right]. \quad (2.7)$$

The characteristic matrix elements given by the dipolar Hamiltonian coupling both the conduction and valence bands are in Table 2.1 [3].

Table 2.1: Matrix elements of the dipole moment \mathbf{D}_{cv}/D [3].

CB		$\langle 1/2, +1/2 $	$\langle 1/2, +1/2 $
HH	$ 3/2, +3/2\rangle$	$-\sqrt{1/2}(\hat{x} + i\hat{y})$	0
	$ 3/2, -3/2\rangle$	0	$\sqrt{1/2}(\hat{x} - i\hat{y})$
LH	$ 1/2, +1/2\rangle$	$\sqrt{2/3}\hat{z}$	$-\sqrt{1/6}(\hat{x} + i\hat{y})$
	$ 1/2, -1/2\rangle$	$\sqrt{1/6}(\hat{x} - i\hat{y})$	$\sqrt{2/3}\hat{z}$

We remind the main conclusions concerning dipole transitions. As required from the conservation of the angular momentum, radiative recombinations lead to an emission of right- (σ^+) and left-circularly polarized photons (σ^-) with a projection of angular momentum along the direction of their \mathbf{k}' wave-vector equal to ± 1 , respectively. Moreover, from intensity of dipoles follows, that the heavy hole (HH) transitions are three times larger than corresponding light hole (LH) transitions. Note, that the transition probability is proportional to $|D_{cv}|^2$. Let us define normalized transition probabilities according to

$$\xi_{HH} = 3/4 \quad \xi_{LH} = 1/4 \quad \xi_{HH} + \xi_{LH} = 1. \quad (2.8)$$

In bulk semiconductor, the HH and LH bands are degenerate at the Γ -point and the present rules are valid for any direction of the emission. In the case of QW structures, this bulk-degeneracy between the HH and LH valence bands is lifted due to quantum confinement or by biaxial epitaxial strain. Moreover, these selection rules are valid only in the vertical (Faraday) geometry where the carrier spin orientation and the photon emission are oriented perpendicularly to the QW plane. Figure 2.1 depicts the selection rules in direct bulk semiconductor and 2D quantum well system [3, 17]. Transitions for which $\Delta m_j = +1$ and $\Delta m_j = -1$ result in the emission of circularly polarized photons with negative (σ^-) and positive (σ^+) helicity, respectively. Moreover, transitions involving heavy holes (HH) are three times more probable than those involving light holes (LH). When we consider 2D quantum system (Fig 2.1b), the energetic splitting between HH and LH states appears as a consequence of the quantum confinement and epitaxial strain. In this case, the depicted selection rules are valid only for vertical geometry [3, 17]

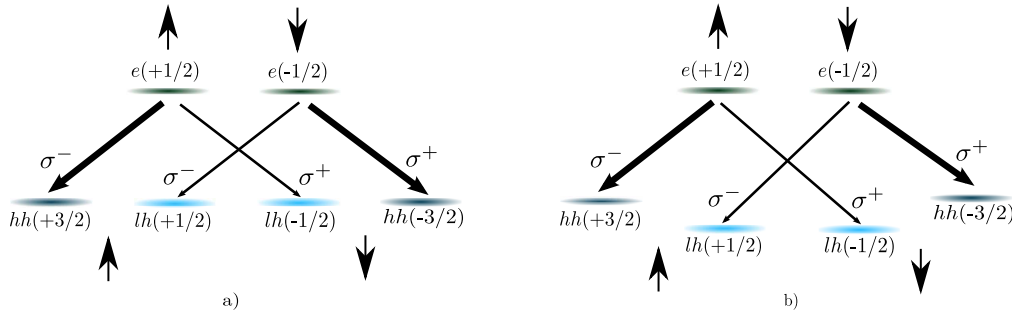


Figure 2.1: Selection rules in a) direct bulk semiconductor and (b) 2D quantum system [3, 17].

2.2 Spin injection into semiconductor: Pumping methods

Spin-polarized carrier populations are generated in semiconductor quantum wells via i) electrical, ii) optical pumping with circularly polarized light, and iii) mixed pumping by using both of them. The evolution of the electrical and optical injection in spin-LEDs and spin-VCSELs has been shortly described in previous chapter.

2.2.1 Electrical pumping

The electrical spin injection is preferred for many applications because of its ability to be integrated in the compact devices. Firstly, such type of injection requires a source of spin-polarized carriers. Under action of the magnetic field in paramagnetic

or ferromagnetic materials, the spin-up and spin-down bands are splitted leading to a different number of spin-polarized electrons at Fermi level. This leads to a net spin polarization which can be injected into an adjacent layer. However, it is well-known that the large conductivity mismatch between a ferromagnetic material and semiconductor leads to a negligible spin-injection efficiency [49]. The only way to match the boundary conditions is to introduce an additional resistance in only one of two spin channels, which compensates the splitting in the semiconductor, or by introducing a high resistance in both spin channels [12, 49]. Suitable solution for this kind of interfacial spin-dependent resistance is using tunnel contact in which the transmission is proportional to the product of the density of states on both sides. In that case the spin-dependent resistance is caused by the spin asymmetry in the density of states in the ferromagnet.

From a technological point of view the easiest way is by using the Schottky contact, which is naturally formed between a semiconductor and a metal. When the barrier is biased in the reverse direction, the carriers tunnel through it at the Fermi level and the density of states in the ferromagnet leads to a spin-dependent tunneling probability. The first experimental demonstration was realized by Zhu *et al.* in 2001. The circular polarization degree of the observed electroluminescence revealed the spin injection efficiency of 2% [5]. In the following year, the spin efficiency up to 32% has been achieved by Hanbicky *et al.* by using Fe/AlGaAs contact [15]. These observations provided conclusive evidence that tunneling is the dominant transport mechanism enabling significant spin injection across the metal/semiconductor interface. However, intermixing between a ferromagnetic and a semiconductor layer during growth can lead to reduced interface quality, which plays an important role in an effective spin injection.

Besides the possibility of using Schottky barriers, the oxide tunnel barriers such as AlO_x [50] and MgO [8] are suitable alternatives. Shortly after the demonstration of the spin injection using Schottky barriers, Al_2O_3 tunnel barriers were implemented into spin-LEDs [50]. Since that time, several devices have been presented that show a very high spin injection efficiency even at elevated temperatures. Typical values obtained with the AlO_x barriers on GaAs are about 21% and 16% at 80 and 300 K, respectively [50] while with (001)-grown epitaxial MgO the spin polarization reaches even 57% at 100 K and 47% at 290 K, respectively [7]. To conclude, using the MgO tunnel barrier seems to be the most attractive way for effective injection into a semiconductor as we will consider in calculations of the emitted polarization state in Chapter 5.

2.2.2 Optical pumping

Despite the preferable electrical spin injection for compact devices, the optical pumping is widely used for several advantages. I) Optically-pumped structures have a more simple design. They are usually electronically undoped and there is no need to deposit the spin injector. Thus preparation is much more simple. II) Optical pumping

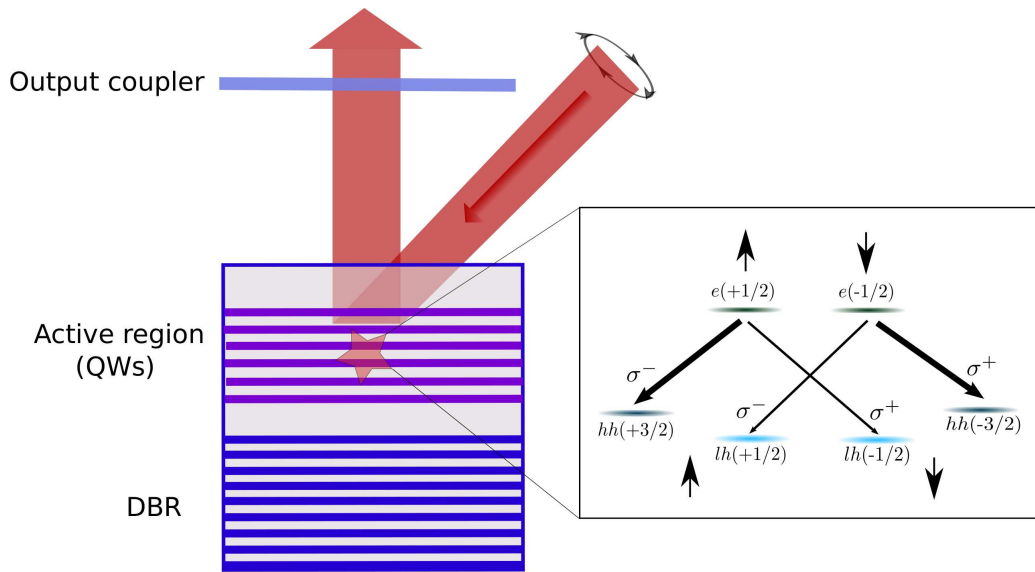


Figure 2.2: Concept of the optically-pumped VECSEL.

allows a uniform carrier excitation over a large area of active region and also absorption in a broad wavelength region. Moreover, cheaper pump diodes can be used due to the larger wavelength tolerance which is linked to the absorption range in semiconductors [51]. III) Optically-pumped lasers such as VECSELs benefits from their additional degree of freedom and enable using of intra-cavity optical elements such as Faraday rotators. The concept of optically-pumped semiconductor lasers with the vertical geometry has been developed in 1966 by Basov *et al.* [52], however, it took more than two decades to fully demonstrate this technique with optimized working structures [53] in a high-power regime [54].

Circularly-polarized pumping reveals as an effective way for spin injection in the semiconductor laser structures as depicted in Fig. 2.2. In that case, the absorption of the circularly-polarized light is the reverse mechanism of spin-polarized carriers recombination and follows the same selection rules. Ando *et al.* demonstrated in 1998 by using VCSEL structure based on the GaAs active region that the partial electron-spin alignment, created by pumping with circularly-polarized light, largely affects the polarization state of lasing output and generates the circular lasing output. Spin-up or spin-down electrons were found to provide greater gain for the left- or right-circularly polarized lasing modes, respectively. Figure 2.3a shows typical polarization characteristics of the VCSEL output slightly above the threshold obtained with the σ^+ circularly polarized pump light. Ando *et al.* found that for the σ^+ excitation the lasing output from the VCSEL mainly consists of σ^+ circularly polarized light even for partially spin-polarized electrons [24].

Since spin-polarized electrons couple selectively to either the left- or right-circularly

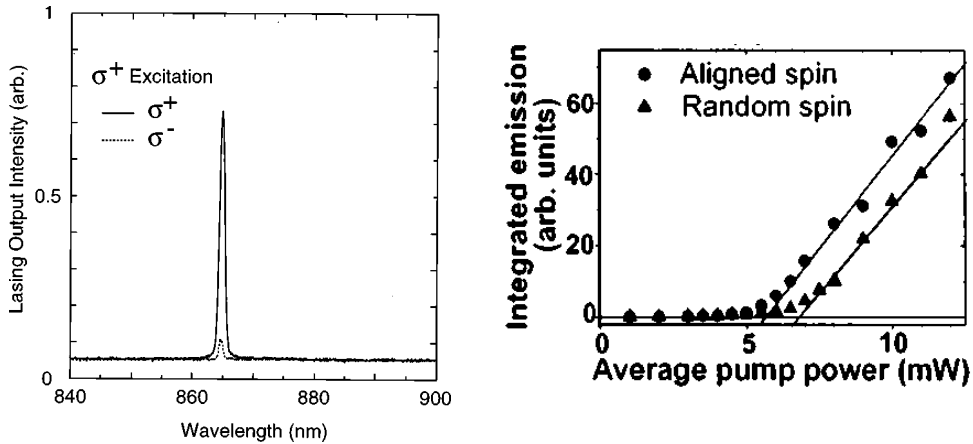


Figure 2.3: a) Lasing emission spectra of two orthogonal circular components, σ^+ and σ^- , from a VCSEL excited with σ^+ circularly polarized pump pulses. Figure reprinted from Ref. 24. b) Emission vs pump intensity for the determination of the VCSEL threshold intensity. Figure reprinted from Ref. 57.

polarized lasing mode in VCSEL, pumping with the 100% spin-polarized current should result in a laser featuring circularly polarized stimulated emission with half of the threshold current. This phenomena has been intuitively described by Zutic *et al.* using "the bucket model" [55, 56]. Figure 2.4 shows the bucket model for (a) a conventional laser and (b) a spin laser. Water added to the bucket represents the carriers, and the water coming out represents the emitted light. Small leaks depict spontaneous emission, and overflowing water reaching the large opening corresponds to the lasing threshold. One can observe two main properties of spin-lasers: i) In the case of spin-polarized laser less water needs to be pumped for it to reach the threshold which result in a stimulated emission with theoretical half of the threshold current and ii) even a small spin unbalance can lead to a pure circular polarization (case slightly above and below the opening). One should note that the boundary between both spin reservoirs is not perfect. This leads to a small spin-flip between them [55].

Threshold reductions have been observed by Rudolph *et al.* at both low and room-temperature regimes for an optically-pumped InGaAs/GaAs QW VCSEL structure [26, 57]. The results of an experiment in a low-temperature operation are depicted in Fig.2.3b. Rudolph *et al.* clearly demonstrated that the threshold is reduced by pumping with spin-polarized electrons under circularly-polarized excitation in comparison to unpolarized electrons with the linearly polarized excitation [57]. The same group demonstrated a 2.5% threshold current reduction at room temperature in an optically-pumped AlGaAs/GaAs QW VCSEL for injected electrons with 50% spin polarization [26].

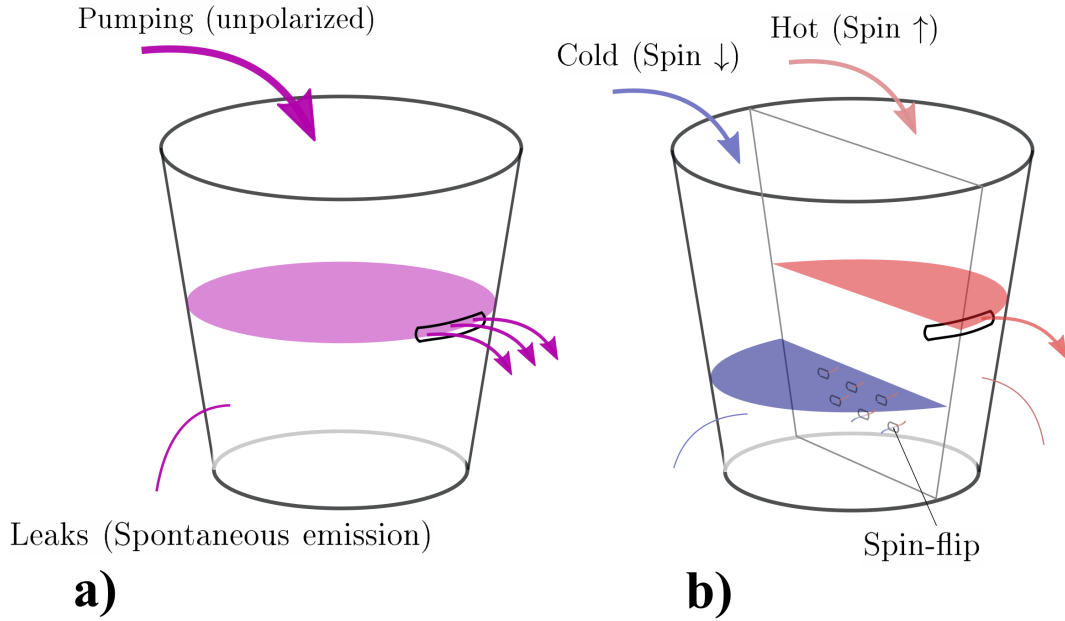


Figure 2.4: The bucket model for a) conventional laser b) spin-laser proposed by Zutic *et al.* [55, 56].

2.3 Design of the V(E)CSEL structure

Generally, the V(E)CSEL device is based on a laser resonator and the active gain medium: quantum wells or quantum dots. Figure 2.5 shows a schematic description of the 1/2-VCSEL semiconductor structure without top mirror dedicated for the optical pumping in the VECSEL configuration. The structures studied in this thesis have been grown on [0 0 1]-GaAs substrate by metalorganic vapour-phase epitaxy (MOCVD) by Dr. Isabelle Sagnes from C2N (LPN Marcoussis).

The $13\lambda/2$ thick active region is constituted of 6 strain-balanced 8 nm In-GaAs/GaAsP QWs with the emitting laser frequency at $\lambda \simeq 1\mu\text{m}$. The strain

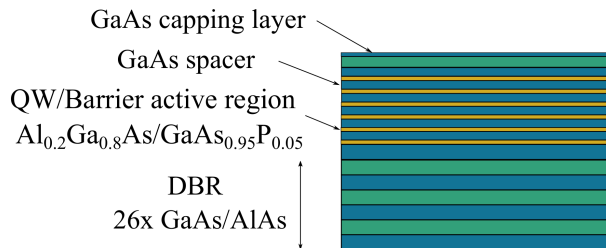


Figure 2.5: Schematic description of the 1/2-VCSEL structure dedicated to the optical pumping.

induced by adding 20% of indium in QW is compensated by inclusion of 5% of phosphorus in GaAsP barriers. Moreover, incorporation of the phosphorus increases the barriers gap from $E_g = 1.423$ eV to $E_g = 1.488$ eV, however, it also reduces the electron capture efficiency in the QW [33]. Each pair of QWs is separated by GaAs spacers, which size decreases when getting closer to the surface. Thicknesses of these spacers are designed to ensure QW placement in the maxima of the electromagnetic field in the cavity. A 30 nm thick insulating AlAs layer in-between the surface and the active medium is used as a carrier confinement layer in optical pumping experiments. The nominal thickness of GaAs capping layer is 10 nm.

The structure consists also of the epitaxial high-reflectivity (99.9%) bottom AlAs/GaAs Bragg mirror (DBR, 26 pairs) of the nominal thicknesses $t_{AlAs} = 85.37$ nm and $t_{GaAs} = 71.8$ nm, which acts as a laser feedback. Bottom DBR is designed to be highly reflective while top DBR (output coupler) is partially reflective. These reflectors act as a one-dimensional photonic crystal (with a photonic band-gap), which consists of epitaxially-grown semiconductor layers having the thicknesses of the quarter wavelengths and alternating with high and low-refractive indices. The principle of such dielectric mirrors is based on the interference of light reflected from the different layers of the dielectric stack. Each interface between the two materials e.g. AlAs/GaAs contributes to the partial reflection of an optical wave. Then if the optical path length difference between reflections from subsequent interfaces is half of the wavelength then all reflected components from the interfaces interfere constructively, which results in a strong reflection in a large spectral region called the bandgap. The achieved reflectivity is determined by the number of layer pairs and by the refractive index contrast between the layer materials.

Figure 2.6 shows the calculated dependence of the reflectivity from a Bragg mirror for two different numbers of layer pairs. The calculation is based on the matrix formalism, which is explained in the following chapter. This structure consists of GaAs/AlAs semiconductor pairs designed for central wavelength $\lambda = 1 \mu\text{m}$. The achieved reflectivity strongly depends on the number of layer pairs. For 5 pairs the maximal reflectivity is around 80 % (red curve). One can observe three main regions (green curve): i) the photonic bandgap with the high reflectivity around $\lambda = 1000$ nm surrounded by ii) the transparent region for $\lambda > 800$ nm with strong interference effects in multilayer structure, and iii) the absorbing region for $\lambda < 800$ nm, where the top GaAs layer absorbs the incident light. The peaks around $\lambda \approx 250$ nm and $\lambda \approx 400$ nm are given by the absorption of the top GaAs layer as can be seen from a comparison with the reflectivity of GaAs (blue curve).

2.4 Linear birefringence and circular gain dichroism

Additional linear in-plane anisotropies in the multilayer semiconductor cavity strongly impact the performance and properties of spin-laser operation [36] leading to complex polarization dynamics. Previous theoretical as well as experimental investiga-

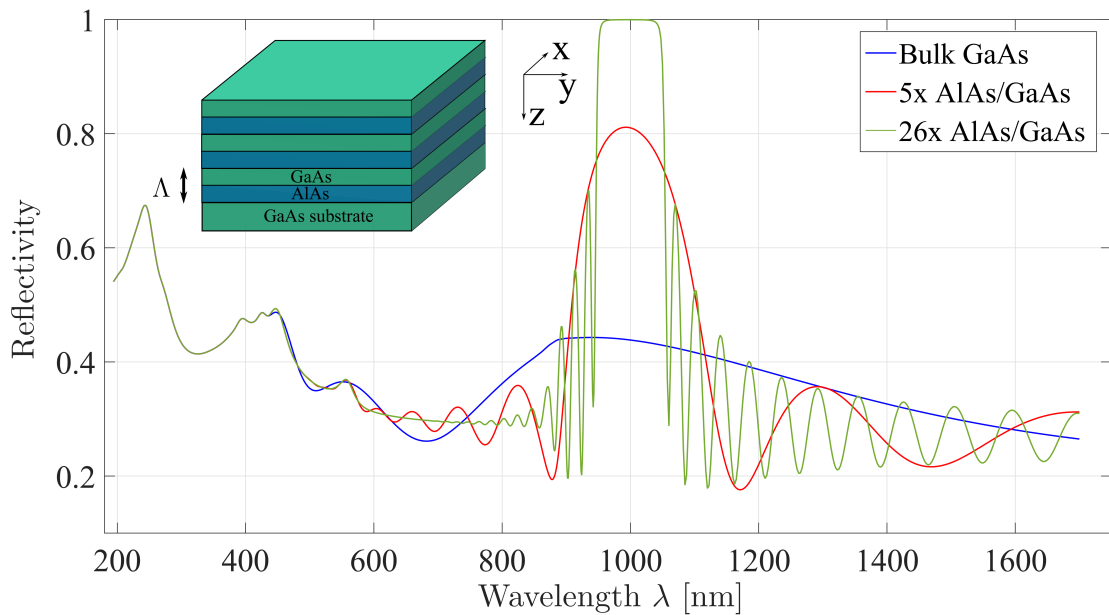


Figure 2.6: Dependence of the Bragg mirror reflectivity on the incident wavelength for two different number of periods.

tions [37] have allowed to separate between several different contributions: i) a linear birefringence originating from interfaces between ternary quantum wells and barriers (GaAsP/InGaAs/GaAsP) and ii) possible local surface strain of III-V material after surface crystalline reconstruction [38, 39], and iii) a magneto-optical anisotropy. First contribution, an in-plane optical anisotropy of III-V quantum well structures, was found due to the reduction from D_{2d} to C_{2v} symmetry group when the host materials do not share any common atoms [38, 39, 41], as well as chemical segregation [38] and strain effect in quantum well. The second contribution originating from the surface may have two different causes: a surface-bulk electro-optic effect due to the appearance of a significant electric field developing from the top surface and an effect related to strain by surface reconstruction [42]. The last contribution is given by magneto-optical effects, which causes the circular dichroism and birefringence in a magnetized ferromagnetic layer used as a spin-injector [40, 58]. The last contribution is discussed in details in Section 3.1.5, Chapter 3.

Natural interface anisotropy

The natural interface anisotropy is a form of an inversion asymmetry, which results from the structure of chemical bonding at the interfaces [59]. Such interface effect reduces the symmetry from D_{2d} to C_{2v} . This argument becomes clear from Figure 2.7, which depicts the atomic structure of zinc-blend type quantum wells along the $[110]$ axis grown on a $[001]$ -oriented substrates. Figure 2.7a shows the case of a

quantum well/barrier system with a common atom (Fig. 2.7a). While within each layer the anions (black circles) are surrounded by equivalent cations (white circles), the interfacial anion is bonded to different cations from the upper and lower layers. Example of such system is GaAs/AlAs structure depicted in Fig. 2.7d. The planes of the As-Al and As-Ga bonds involving a common anion are rotated by $\pi/2$ with respect to each other at each side of the interface. It results from this particular C_{2v} symmetry leading to a possible heavy to light hole mixing in the component of the wavefunction at interface leading to the optical anisotropy [60, 61]. Consequently, different optical properties are expected along the $[110]$ and $[\bar{1}\bar{1}0]$ directions. However, even if the top interface exhibits any anisotropy due to the symmetry reason, such anisotropy would be compensated at the bottom interface because the chemical bonds themselves are the same. The quantum well/barrier system thus remain symmetric [42]. On the other hand, a different situation is in the case when quantum well/barrier system does not share any common atoms as depicted in Fig. 2.7b and Fig. 2.7c. The anisotropy of top interface is not compensated at the bottom interface because the chemical bondings are different and thus the system is not symmetric.

The latter case has been clearly demonstrated by Hall *et al.* on binary InAs/GaSb superlattices with no common atoms [62]. Krebs *et al.* have examined and theoretically predicted the interface anisotropy in ternary semiconductor quantum well systems such as GaInAs/InP. Although both well and barrier materials contain the common atom indium (In), the "average" atom (GaIn) in quantum well is different from In in the barrier and therefore contributes to the interface asymmetry [59]. Two years later in 1998, Krebs *et al.* reported polarization-resolved optical transmission measurements performed on GaInAs/InP multi-quantum wells evidencing a large dichroism [63].

In the case of systems studied in this work, In(22%)Ga(78%)As/GaAs(95%)P(5%), quantum wells and barriers share the common atoms Ga and As. However, the "average" cation-type and anion-type atoms (InGa) and (As) in quantum wells are different from the "average" atoms (Ga) and (AsP) in the barriers. Therefore the symmetry breaking leading to the optical linear birefringence and dichroism is expected. Moreover, the local surface strain of III-V material due to even a small lattice mismatch after surface crystalline reconstruction as well as due to the chemical segregation can be present [38, 39]. The detailed origin of such optical interfacial anisotropies are currently under study in LSI-UM ϕ by advanced $k.p$ methods in a frame of the PhD study of Quang Duy To.

Anisotropy at surface

The linear birefringence and dichroism originating from the surface may have two different causes: the effect related to the strain by surface reconstruction [42, 64] and the surface-bulk electro-optic effect due to the appearance of a significant electric field at a surface.

One contribution to the overall anisotropy predicted and observed at clean (001)

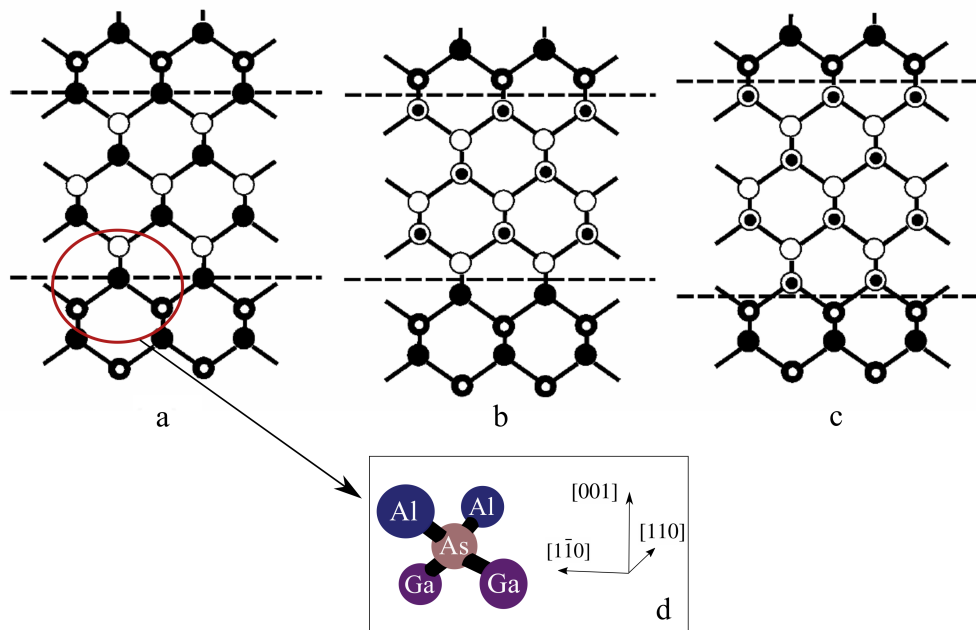


Figure 2.7: Origin of the natural interface asymmetry [59].

surfaces of binary III-V semiconductors is caused by the the surface reconstruction with its characteristic dimer-configuration and back-bonds as depicted in Fig. 2.8. This anisotropy could be understood on the basis of trigonally bonded overlayers leading to the strain and thus different optical properties along the $[110]$ and $[\bar{1}10]$ directions [65]. Typical examples are the As or Ga dimers found on the different reconstructions of the GaAs surface. Since the dimers have a preferential orientation, electronic transitions involving these states are expected to be highly anisotropic. Moreover, reconstruction induces small changes in atomic positions in the atomic layers close to the surface and thus produces a strain field [42, 64].

Another contribution to the surface linear anisotropy is due to the linear electro-optic, bulk-related effect induced by the sample surface electric field. Such effect originates from an electric charge exchange between the bulk and the surface states of the semiconductor, in order for the material to attain thermodynamic equilibrium. As a result of this process, the Fermi level becomes pinned at the semiconductor surface at an energy in the forbidden gap. The presence of the surface electric field results in the breaking of the symmetry of GaAs near the surface and in the loss of the optical isotropy in this region. A systematic study of this effect on n-type GaAs has been done by Acosta-Ortiz *et al.* by using reflectance-difference technique [66].

On the other hand, the electro-optic effects can appear also in the presence of the applied external electric field (electrically-injected VCSELs) or the electric field from high-power pumping laser (optically-pumped VCSELs). When an electric field is present along $[001]$ direction, the refractive indices along $[110]$ and $[\bar{1}10]$ can

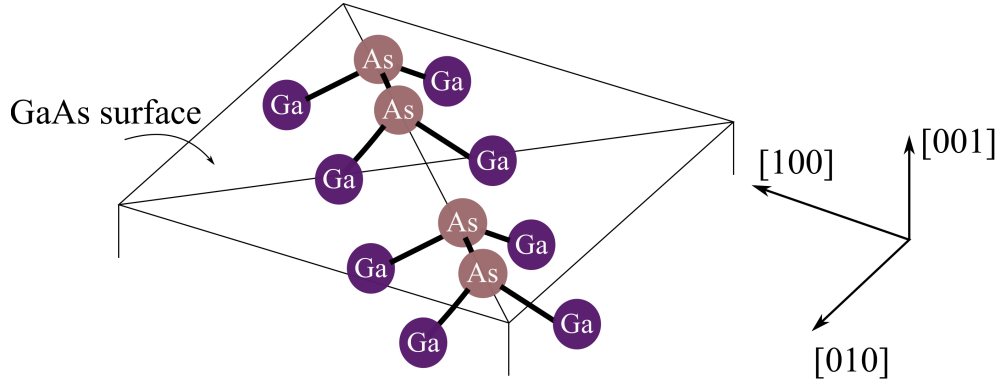


Figure 2.8: The surface reconstruction with its characteristic dimer-configuration and back-bonds.

be calculated as in Ref. [67]:

$$n_{[110]} = n_0 - \frac{n_0^3}{2} \tilde{r} E, \quad (2.9)$$

$$n_{[1\bar{1}0]} = n_0 + \frac{n_0^3}{2} \tilde{r} E, \quad (2.10)$$

where n_0 is the refractive index in the absence of an electric field E and \tilde{r} is the electro-optic coefficient. Such electro-optical birefringence can be used to control the cavity resonance of the polarized light along the $[110]$ and $[1\bar{1}0]$ directions, which are shifted to shorter and longer wavelength depending on the direction of the applied electric field [68]. Figure 2.9 shows the emission spectra of the VCSEL device investigated by Park *et al.*, where the birefringence has been induced at the top of DBR by applying an electric field along the $[001]$ direction. The emission spectrum measured in the absence of an electric field represents the $[1\bar{1}0]$ mode. For the $+10$ V applied voltage, the emission spectrum shifts to a longer wavelength because the $[1\bar{1}0]$ mode shows a red shift (dashed curve). On the other hand, for the -10 V applied voltage, the emission spectrum of the $[110]$ mode also shows a small red shift (dotted curve) so that the dominant polarization mode occurs along the $[110]$ or $[1\bar{1}0]$ direction for the negative or positive electric field application. By varying the direction and strength of the electric field, a wanted polarization mode can be selected [68].

Measurement of the linear birefringence in optically-pumped 1/2-VCSEL structure

The birefringence of the VCSEL structure can be generally measured and extracted from the induced frequency splitting between two emitted polarization states caused by the difference of their optical path. However, in the case of VCSEL with long cavities (cm), the frequency splitting is expected in the range of a few MHz and

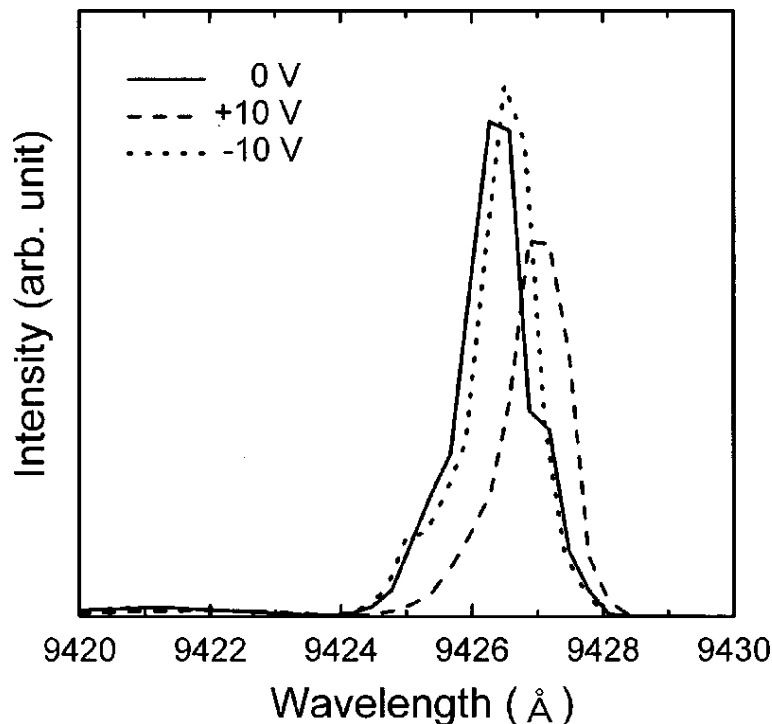


Figure 2.9: Shift of emission spectrum at positive and negative applied voltages. Figure extracted from Ref. 68.

therefore can not be observed with optical spectrum analyzers limited to GHz resolution. To overcome this difficulty, transferring the optical frequency detuning between the two laser modes into the electrical domain has been proposed by groups at Unite Mixte de Physique CNRS-Thales [69] and at IES Montpellier [70]. The measurement principle is shown in Fig. 2.10. The output orthogonally-polarized laser modes are equally projected to the polarizer axis oriented at 45° with respect to the polarization axis. The beam is then focused on a low noise detector with a fast photodiode and a low noise amplifier. The relative intensity noise (RIN) spectrum of the laser is measured with a radio-frequency (RF) spectrum analyzer [70]. Then the peak observed in RIN spectrum reflects the beat note due to the orthogonal polarizations which are splitted in a frequency. We will discuss results in details in Chapter 6. Together with a formalism derived in this work we will extract the linear permittivity tensors at surface and in the quantum wells.

2.5 Conclusion of the chapter

This chapter introduced basic principles of spin-V(E)CSELs. As has been shown, the emission of circularly-polarized light originates from the radiative recombination of spin-polarized carriers. We described the electrical and optical pumping methods, which enable the spin injection in semiconductor quantum wells. The advantages of

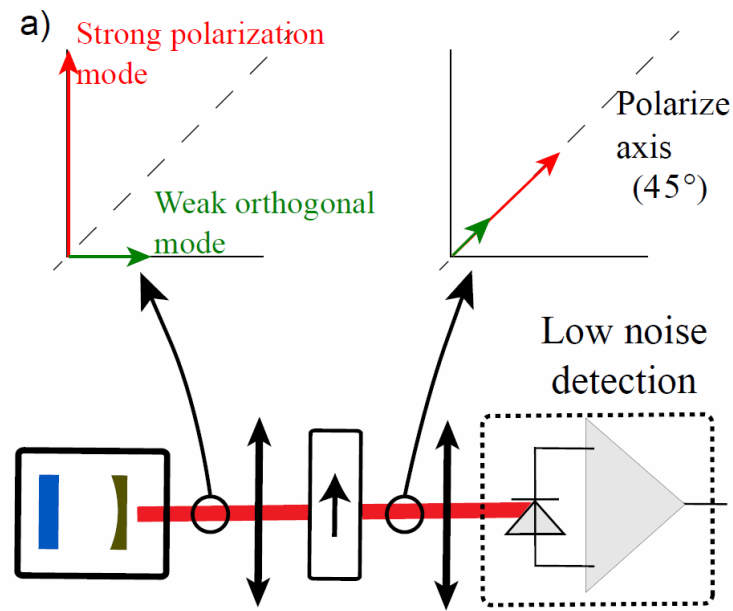


Figure 2.10: Experimental setup of the birefringence measurement. Figure extracted from Ref. 70.

the optical pumping have been pointed out. Multilayer spin-V(E)CSEL devices have been briefly described together with the possible local anisotropies in the quantum wells, interfaces, and at surface. Such local anisotropies have the crucial impact on the polarization state of the light emitted from the laser structures as well as on the frequency detuning between laser modes. Such detuning is expected in the range of a few MHz. Therefore, transferring the optical detuning into the electrical domain is an effective method to study the birefringences in multilayer laser structures such as the 1/2-VCSELs.

Chapter 3

Polarization state of light: Focus on ellipsometry of multilayer semiconductor lasers

This chapter offers a brief review of the electromagnetic theory, which describes the properties of the electromagnetic wave propagation in anisotropic multilayer structures. This theoretical background is required for the fundamental understanding and characterization of passive VECSEL structures with local linear birefringence and dichroism. After derivation of wave equation for generally anisotropic medium, we demonstrate the 4×4 matrix formalism for modeling of the electromagnetic response of the anisotropic multilayer structures. The change of a polarization state of light due to the local linear anisotropy is theoretically described using the Jones and Mueller matrices. Finally to characterize VECSEL structure we introduce the Mueller matrix ellipsometry as an effective measurement technique used in this work. We compare the Mueller matrix ellipsometry to other widely used techniques such as reflectance difference spectroscopy and spectroscopic ellipsometry, and we point out the advantage of this method.

3.1 Electromagnetic response of anisotropic structure

3.1.1 Electromagnetic field equations in anisotropic media

The presence of the electromagnetic field in a linear anisotropic medium is governed by the partial differential equations known as the Maxwell equations. These equations describe the classical properties of the electromagnetic field inside the media

and can be written in the following differential form:

$$\nabla \cdot \mathbf{D}(\mathbf{r}, t) = \rho, \quad (3.1a)$$

$$\nabla \cdot \mathbf{B}(\mathbf{r}, t) = 0, \quad (3.1b)$$

$$\nabla \times \mathbf{E}(\mathbf{r}, t) = -\frac{\partial \mathbf{B}(\mathbf{r}, t)}{\partial t}, \quad (3.1c)$$

$$\nabla \times \mathbf{H}(\mathbf{r}, t) = \mathbf{j}(\mathbf{r}, t) + \frac{\partial \mathbf{D}(\mathbf{r}, t)}{\partial t}, \quad (3.1d)$$

where $\mathbf{E}(\mathbf{r}, t)$, $\mathbf{H}(\mathbf{r}, t)$, $\mathbf{D}(\mathbf{r}, t)$, $\mathbf{B}(\mathbf{r}, t)$, ρ , and $\mathbf{j}(\mathbf{r}, t)$ denote the electric field intensity, the magnetic field intensity, the electric displacement, the magnetic flux density, the volume density of free charges, and the current density, respectively. The medium properties, i.e. the medium polarization $\mathbf{P}(\mathbf{r}, t)$ and the magnetization $\mathbf{M}(\mathbf{r}, t)$, are connected to the field quantities by additional constitutive relations:

$$\mathbf{D}(\mathbf{r}, t) = \varepsilon_0 \mathbf{E}(\mathbf{r}, t) + \mathbf{P}(\mathbf{r}, t) = \hat{\varepsilon} \mathbf{E}(\mathbf{r}, t), \quad (3.2a)$$

$$\mathbf{B}(\mathbf{r}, t) = \mu_0 \mathbf{H}(\mathbf{r}, t) + \mathbf{M}(\mathbf{r}, t) = \hat{\mu} \mathbf{H}(\mathbf{r}, t), \quad (3.2b)$$

where $\hat{\varepsilon}$ and $\hat{\mu}$ are respectively the (generally tensorial) electric permittivity and the magnetic permeability functions of a medium. The permittivity and the permeability of free space are denoted as ε_0 and μ_0 , respectively. The medium conductivity tensor $\hat{\sigma}$ connects the electric field intensity with the current density by the following way:

$$\mathbf{j}(\mathbf{r}, t) = \hat{\sigma} \mathbf{E}(\mathbf{r}, t). \quad (3.3)$$

In the optical spectral region, the magnetic susceptibility $\chi_M = \mu/\mu_0 - 1$ assumes very small values monotonously dependent on the radiation frequency due to the weak feedback of the magnetic dipoles in a medium. It is therefore reasonable to set its value to a real scalar constant equal to a very small number or zero [71]. Therefore, the magnetic permeability for optical frequencies is taken as:

$$\mu = \mu_0. \quad (3.4)$$

Considering no free charges in the medium ($\rho = 0$) allows to rewrite the Maxwell equations (3.1) in the differential form:

$$\nabla \cdot [\hat{\varepsilon} \mathbf{E}(\mathbf{r}, t)] = 0, \quad (3.5a)$$

$$\nabla \cdot \mathbf{H}(\mathbf{r}, t) = 0, \quad (3.5b)$$

$$\nabla \times \mathbf{E}(\mathbf{r}, t) = -\mu_0 \frac{\partial \mathbf{H}(\mathbf{r}, t)}{\partial t}, \quad (3.5c)$$

$$\nabla \times \mathbf{H}(\mathbf{r}, t) = \hat{\sigma} \mathbf{E}(\mathbf{r}, t) + \hat{\varepsilon} \frac{\partial \mathbf{E}(\mathbf{r}, t)}{\partial t}. \quad (3.5d)$$

3.1.2 Wave equation

One of the most important prediction of the Maxwell equations is the existence of electromagnetic waves which can transport energy and which are described by one of the most fundamental equations to all of electromagnetic theory - the wave equation. Let us derive the wave equation for the electric field \mathbf{E} directly from the Maxwell equations (3.5) for isotropic absorbing medium (tensorial $\hat{\varepsilon}$ and $\hat{\sigma}$ are reduced to scalars ε and σ) and discuss its solution.

Eliminating $\mathbf{H}(\mathbf{r}, t)$ by application of the operators $\nabla \times$ and $\partial/\partial t$ on the equations (3.5c) and (3.5d), respectively, and by application of the identity:

$$\nabla \times (\nabla \times \mathbf{E}) = \nabla (\nabla \cdot \mathbf{E}) - \nabla^2 \mathbf{E}, \quad (3.6)$$

we arrive to the wave equation:

$$\nabla^2 \mathbf{E}(\mathbf{r}, t) - \varepsilon \mu_0 \frac{\partial^2 \mathbf{E}(\mathbf{r}, t)}{\partial t^2} - \sigma \mu_0 \frac{\partial \mathbf{E}(\mathbf{r}, t)}{\partial t} = 0. \quad (3.7)$$

The solution can be found for a monochromatic wave with the angular frequency ω and the complex amplitude $\mathbf{E}_\omega(\mathbf{r})$:

$$\mathbf{E}(\mathbf{r}, t) = \mathbf{E}_\omega(\mathbf{r}) e^{i\omega t}. \quad (3.8)$$

Hence, all time derivatives can be simply replaced by the $i\omega$ factor and the wave equation (3.7) can be rewritten as:

$$\nabla^2 \mathbf{E}_\omega(\mathbf{r}) + \omega^2 \mu_0 \tilde{\varepsilon} \mathbf{E}_\omega(\mathbf{r}) = 0, \quad (3.9)$$

known as the Helmholtz equation, where $\tilde{\varepsilon} = \varepsilon_0 \varepsilon_r = \varepsilon - \frac{i}{\omega} \sigma$ is the complex permittivity with ε_r denoting the relative permittivity. Considering the velocity of light c and the wavenumber k_0 in vacuum:

$$c = \frac{1}{\sqrt{\mu_0 \varepsilon_0}} \quad (3.10)$$

$$k_0 = \frac{\omega}{c}, \quad (3.11)$$

yields to the Helmholtz equation in the form:

$$[\nabla^2 + k_0^2 \varepsilon_r] \mathbf{E}_\omega(\mathbf{r}) = 0, \quad (3.12)$$

where we consider the relationship between the wave vector k and the refractive index:

$$k^2 = k_0^2 \varepsilon_r = k_0^2 n^2. \quad (3.13)$$

3.1.3 Plane electromagnetic wave in isotropic medium

Let us examine one of the elementary solution of the Helmholtz equation (3.12) in an isotropic medium: a monochromatic electromagnetic wave with the wavevector \mathbf{k} whose complex amplitude vectors are plane waves so that:

$$\mathbf{E}_\omega(\mathbf{r}) = \mathbf{E}_0 e^{-i\mathbf{k}\mathbf{r}}, \quad (3.14)$$

$$\mathbf{H}_\omega(\mathbf{r}) = \mathbf{H}_0 e^{-i\mathbf{k}\mathbf{r}}, \quad (3.15)$$

where \mathbf{E}_0 and \mathbf{H}_0 are the complex envelopes in an isotropic medium (free of charges). Substitutions of (3.15) into the Maxwell equations with the isotropic relative permittivity ε_r leads to:

$$\mathbf{k} \cdot \mathbf{E}_0 = 0, \quad (3.16a)$$

$$\mathbf{k} \cdot \mathbf{H}_0 = 0, \quad (3.16b)$$

$$\mathbf{E}_0 = -\frac{1}{\omega \varepsilon_0 \varepsilon_r} \mathbf{k} \times \mathbf{H}_0, \quad (3.16c)$$

$$\mathbf{H}_0 = -\frac{1}{\omega \mu_0} \mathbf{k} \times \mathbf{E}_0. \quad (3.16d)$$

From the above equations it follows, that \mathbf{E}_0 , \mathbf{H}_0 , and \mathbf{k} are mutually orthogonal, as illustrated in Fig. 3.1. Moreover, the complex Poynting vector $\mathbf{S}_p = \frac{1}{2} \mathbf{E} \times \mathbf{H}^*$ is parallel to the wavevector \mathbf{k} . This means that the power transferred by wave flows along a normal direction to the wavefronts with magnitude:

$$I = \frac{1}{2} |E_0 H_0^*| = \frac{|E_0|^2}{\eta}, \quad (3.17)$$

where $\eta = \sqrt{\mu_0/\varepsilon}$ denotes the impedance of the medium.

To demonstrate the attenuation of light due to the absorption in the isotropic material with the complex refractive index $n = \Re(n) - i\Im(n) = \sqrt{\varepsilon_r}$, where $\Re(n)$ and $\Im(n)$ denote, respectively, the real and imaginary part of n , one can consider for the wave traveling in the z direction:

$$\mathbf{E}_\omega(z) = \mathbf{E}_0 e^{-ik_0 n z} = \mathbf{E}_0 e^{-ik_0 \Re(n)z} e^{-k_0 \Im(n)z}, \quad (3.18)$$

giving the **Beer-Lambert law**:

$$I(z) = I_0 e^{-2k_0 \Im(n)z} = I_0 e^{-\tilde{\alpha}z}, \quad (3.19)$$

where α is the absorption coefficient of the absorbing medium. Certain media, such as used in lasers, can amplify rather than attenuate the light and thus exhibit $\tilde{\alpha} < 0$ in which case $\tilde{\gamma} = -\tilde{\alpha}$ is called the medium gain [72]. Note that Eq. (3.19) does not include any interface or interference effects, which will be explained later.

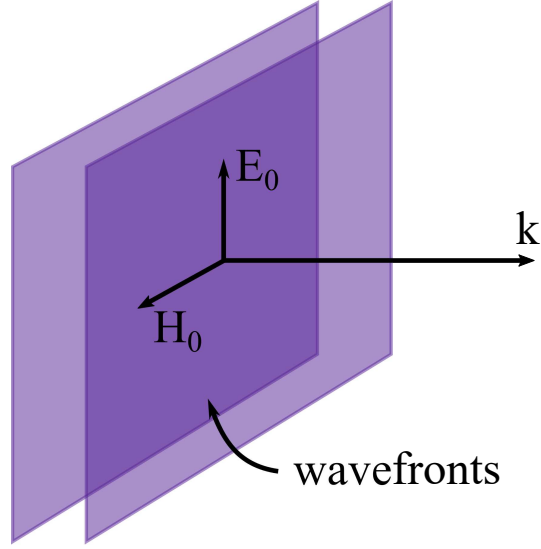


Figure 3.1: Orthogonal orientation of \mathbf{E} , \mathbf{H} , and \mathbf{k} vectors of the plane wave in an isotropic medium.

3.1.4 Plane electromagnetic wave in anisotropic medium

The Maxwell equations (3.16c) and (3.16d) can be for an anisotropic medium with the tensorial relative permittivity $\hat{\epsilon}_r$ generalized to the form:

$$\mathbf{k} \times \mathbf{H}_0 + \omega \epsilon_0 \hat{\epsilon}_r \mathbf{E}_0 = 0, \quad (3.20a)$$

$$\mathbf{k} \times \mathbf{E}_0 - \omega \mu_0 \mathbf{H}_0 = 0. \quad (3.20b)$$

Elimination of \mathbf{H}_0 from Eqs. (3.20) and application of the identity:

$$\mathbf{k} \times (\mathbf{k} \times \mathbf{E}_0) = (\mathbf{k} \cdot \mathbf{E}_0) \mathbf{k} - (\mathbf{k} \cdot \mathbf{k}) \mathbf{E}_0, \quad (3.21)$$

lead to the wave equation for anisotropic medium:

$$k_0^2 \hat{\epsilon} \mathbf{E}_0 - \mathbf{k}^2 \mathbf{E}_0 + \mathbf{k} (\mathbf{k} \cdot \mathbf{E}_0) = 0. \quad (3.22)$$

Particular solutions of this equation are discussed in next section.

3.1.5 Materials characteristics

Anisotropic materials can be represented by the 9-element permittivity tensor such that the electric field \mathbf{E} and displacement field \mathbf{D} are related by Eq. (3.2a). As has been discussed, the general form of the complex permittivity tensor $\hat{\epsilon}$ includes losses in material given by the conductivity tensor $\hat{\sigma}$ so that:

$$\hat{\epsilon} = \epsilon_0 \hat{\epsilon}_r = \hat{\epsilon} - \frac{i}{\omega} \hat{\sigma}, \quad (3.23)$$

where the relative permittivity tensor $\hat{\epsilon}_r$ can be generally written as follows:

$$\hat{\epsilon}_r = \begin{pmatrix} \epsilon_{xx} & \epsilon_{xy} & \epsilon_{xz} \\ \epsilon_{yx} & \epsilon_{yy} & \epsilon_{yz} \\ \epsilon_{zx} & \epsilon_{zy} & \epsilon_{zz} \end{pmatrix}. \quad (3.24)$$

Crystals, in general, are described by a symmetric permittivity tensor. By making the appropriate choice of axes, called principal axes, the dielectric tensor for orthorombic crystal can be diagonalized as given by:

$$\hat{\epsilon}_r = \begin{pmatrix} \epsilon_x & 0 & 0 \\ 0 & \epsilon_y & 0 \\ 0 & 0 & \epsilon_z \end{pmatrix}, \quad (3.25)$$

where ϵ_x , ϵ_y , and ϵ_z are called the principal dielectric constants.

For an uniaxial crystal with optical axis parallel to z axis, such as with trigonal, tetragonal, and hexagonal symmetry, two of three components are equal $\epsilon_x = \epsilon_y$ but the third one ϵ_z is different. Thus one can write:

$$\hat{\epsilon}_r = \begin{pmatrix} \epsilon_x & 0 & 0 \\ 0 & \epsilon_x & 0 \\ 0 & 0 & \epsilon_z \end{pmatrix}. \quad (3.26)$$

The simplest form of dielectric tensor reveals for cubic crystal:

$$\hat{\epsilon}_r = \begin{pmatrix} \epsilon_x & 0 & 0 \\ 0 & \epsilon_x & 0 \\ 0 & 0 & \epsilon_x \end{pmatrix} = \begin{pmatrix} \epsilon_r & 0 & 0 \\ 0 & \epsilon_r & 0 \\ 0 & 0 & \epsilon_r \end{pmatrix}. \quad (3.27)$$

Magneto-optical tensor

An optical response in magnetic media, such as Co, Fe, or Ni, depends on their magnetic state, and this dependence manifests itself in magneto-optic (MO) effects [71, 73]. In a magnetized but otherwise optically isotropic medium, one can observe the linear and the circular birefringence and dichroism, depending on the orientation of the magnetization in the medium. We mention the case (called the polar configuration) with the magnetization oriented normal to the interface (along z coordinate axis). In general, the alignment of spins upon injection into a semiconductor implies the presences of a magnetic layer somewhere in the vicinity of the contact of the spin-optoelectronic device. For this reason, using of ferromagnetic layer as a part of spin-injector in polar magnetization is necessary. The permittivity tensor of such cubic crystal ferromagnet with polar magnetization has the form:

$$\hat{\epsilon}_{r,polar} = \begin{pmatrix} \epsilon_{xx} & -i\epsilon_{xy}(M_z) & 0 \\ i\epsilon_{xy}(M_z) & \epsilon_{xx} & 0 \\ 0 & 0 & \epsilon_{xx} \end{pmatrix}, \quad (3.28)$$

where the off-diagonal components $\varepsilon_{xy}(M_z) = -\varepsilon_{yz}(M_z)$ are proportional to the (polar) magnetization component M_z . We note that the quadratic and higher-order terms in magnetization are neglected here. Then the solution of the wave equation admits circularly polarized proper polarizations propagating along z - direction with different velocities and absorptions leading to the circular birefringence and dichroism, respectively.

3.1.6 Polarization states of light: Jones and Stokes vectors

The time course of the direction of $\mathbf{E}(r, t)$ determines a polarization state of the light, which plays an important role in the interaction of light in absorbing medium such as in bulk media but also in gain laser structures. For example: i) the amount of light reflected or transmitted through a certain material is polarization dependent and ii) the absorption and the amplification of light during its traveling in a laser cavity depends on the helicity of the circular polarization. The polarization state of light is described by **the 2×2 Jones matrix calculus**. Let us define the complex envelope of the wave traveling in the z - direction in the following way:

$$\mathbf{E}_0 = E_{0x}\hat{\mathbf{x}} + E_{0y}\hat{\mathbf{y}}, \quad (3.29)$$

where $\hat{\mathbf{x}}$ and $\hat{\mathbf{y}}$ are the unit Cartesian vectors. The polarization state is commonly described using a column matrix known as Jones vector [74]:

$$\mathbf{J} = \begin{bmatrix} E_{0x} \\ E_{0y} \end{bmatrix} = \begin{bmatrix} |E_{0x}| e^{i\varphi_x} \\ |E_{0y}| e^{i\varphi_y} \end{bmatrix}, \quad (3.30)$$

where $\varphi_{x,y}$ are the initial phases and the total intensity is $I = (|E_{x0}|^2 + |E_{y0}|^2) / 2\eta$ [72]. Using two parameters, the ratio $\mathcal{R} = |E_{y0}| / |E_{x0}|$ and the phase difference $\varphi = \varphi_y - \varphi_x$, is sufficient to determine the orientation and the shape of generally elliptically polarized light:

$$\tan 2\theta = \frac{2\mathcal{R}}{1 - \mathcal{R}^2} \cos \varphi \quad (3.31a)$$

$$\sin 2\epsilon = \frac{2\mathcal{R}}{1 + \mathcal{R}^2} \sin \varphi, \quad (3.31b)$$

$$(3.31c)$$

where θ and ϵ are the azimuth and the ellipticity of the polarization ellipse, respectively [72]. The normalized Jones vectors for some special polarizations are shown in Table 3.1.

The Jones vector defined by (3.30) only spans the space of fully polarized light and cannot be used for description of partially polarized or unpolarized light. Mathematically convenient and a more general description of the polarization state of light was defined by G.G. Stokes as a set of four real numbers S_0 , S_1 , S_2 , and S_3

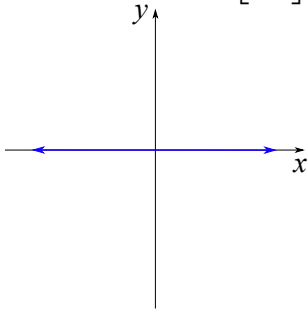
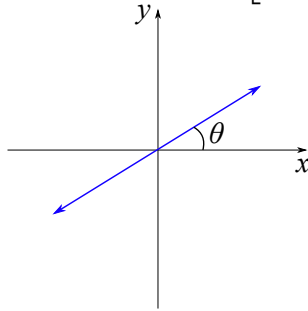
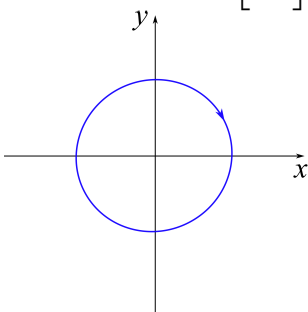
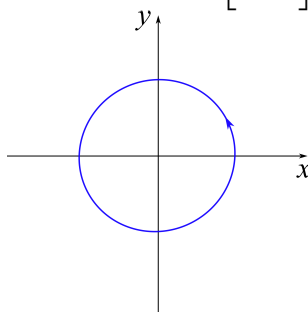
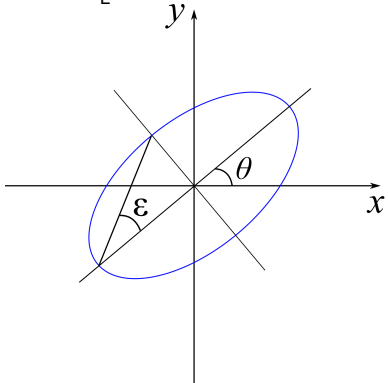
<p>LP in x $\mathbf{J} = \begin{bmatrix} 1 \\ 0 \end{bmatrix}$</p> 	<p>LP at angle θ $\mathbf{J} = \begin{bmatrix} \cos \theta \\ \sin \theta \end{bmatrix}$</p> 
<p>RCP $\mathbf{J} = \frac{1}{\sqrt{2}} \begin{bmatrix} 1 \\ i \end{bmatrix}$</p> 	<p>LCP $\mathbf{J} = \frac{1}{\sqrt{2}} \begin{bmatrix} 1 \\ -i \end{bmatrix}$</p> 
<p>EP $\mathbf{J} = \begin{bmatrix} \cos \theta \cos \epsilon - i \sin \theta \sin \epsilon \\ \sin \theta \cos \epsilon + i \cos \theta \sin \epsilon \end{bmatrix}$</p> 	

Table 3.1: The normalized Jones vectors of linearly (LP), right- and left circularly (RCP, LCP), and elliptically (EP) polarized light.

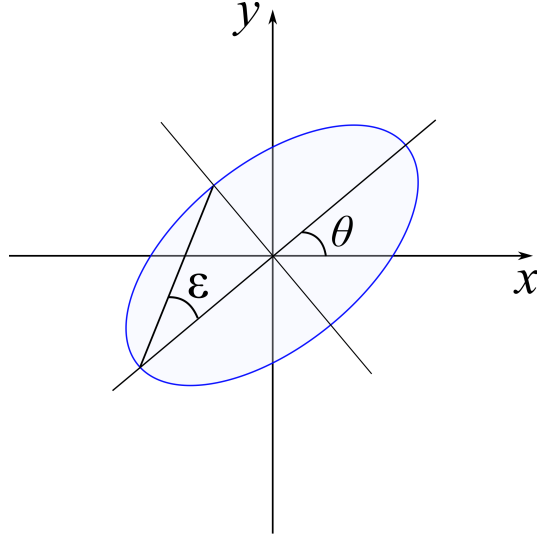


Figure 3.2: The polarization state of light described by the azimuth θ and the ellipticity ϵ of the polarization ellipse.

which define **the Stokes vector**:

$$\mathbf{S} = \begin{pmatrix} S_0 \\ S_1 \\ S_2 \\ S_3 \end{pmatrix} = \begin{pmatrix} I_x + I_y \\ I_x - I_y \\ I_{45} - I_{-45} \\ I_{RP} - I_{LP} \end{pmatrix}, \quad (3.32)$$

which shows the light intensities of different polarization states and could describe unpolarized, partially polarized, and fully polarized light. The Stokes parameters are for fully polarized light defined as:

- $S_0 = I_x + I_y = E_x E_x^* + E_y E_y^* \dots$ the total light intensity,
- $S_1 = I_0 = I_x - I_y = E_x E_x^* - E_y E_y^* \dots$ the intensity difference between light linearly polarized in x and y directions,
- $S_2 = I_{45} - I_{-45} = E_x E_y^* + E_x^* E_y \dots$ the intensity difference between light linearly polarized along the plane with angle $\pm 45^\circ$ about the x -plane,
- $S_3 = I_R - I_L = i(E_x^* E_y - E_x E_y^*) \dots$ the intensity difference between right and left circularly polarized light.

The three Stokes vector components (S_1, S_2, S_3) are the Cartesian coordinates of the point on the Poincaré sphere $(w_1, w_2, w_3) = (\cos 2\epsilon \cos 2\theta, \cos 2\epsilon \sin 2\theta, \sin 2\epsilon)$ multiplied by S_0 [72] as depicted in Fig. 3.3. For example, the points on the equator with $2\theta = 0^\circ$ and $2\theta = 90^\circ$ represent states of the linear polarization along the x axis and the linear polarization at angle 45° from x axis, respectively. The north and south poles $2\epsilon = \pm 90^\circ$ represents, respectively, right and left circularly polarized

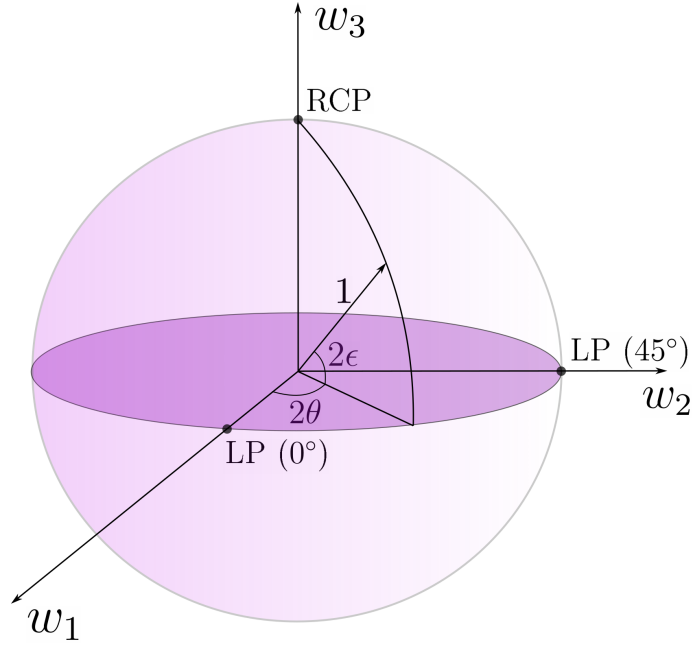


Figure 3.3: The three Stokes vector components (S_1, S_2, S_3) are the Cartesian coordinates of the point on the Poincaré sphere (of unit radius) $(w_1, w_2, w_3) = (\cos 2\epsilon \cos 2\theta, \cos 2\epsilon \sin 2\theta, \sin 2\epsilon)$. Points on the Poincaré sphere representing linearly (LP) and right circularly (RCP) polarized light are marked with black points.

states. Moreover, the portion of an electromagnetic wave, which is polarized, can be described by the degree of polarization defined by:

$$\mathcal{P} = \frac{\sqrt{S_1^2 + S_2^2 + S_3^2}}{S_0}, \quad (3.33)$$

which for totally polarized, unpolarized, and partially polarized light is equal to $\mathcal{P} = 1$, $\mathcal{P} = 0$, and $0 < \mathcal{P} < 1$, respectively.

3.1.7 Jones and Stokes-Mueller formalism

In the absence of depolarization effects, the interaction of the fully polarized incident light transforms the input Jones vector (3.30) into output Jones vector through the linear transformation:

$$\begin{bmatrix} E_x \\ E_y \end{bmatrix}_{out} = \begin{bmatrix} J_{xx} & J_{xy} \\ J_{yx} & J_{yy} \end{bmatrix} \begin{bmatrix} E_x \\ E_y \end{bmatrix}_{in}, \quad (3.34)$$

where J_{ij} are the elements of the 2×2 Jones matrix. Another basis widely used is related to the plane of incidence, which is the plane made by the incoming propagation direction and the vector perpendicular to the plane of an interface as depicted

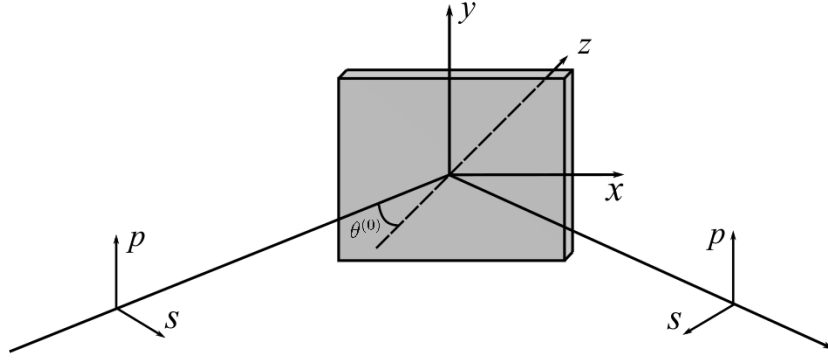


Figure 3.4: The electric field of s -polarization is oriented perpendicularly to the plane of incidence, while p -polarization lies in the plane of incidence.

in Fig. 3.4. The linearly polarized light with its electric field normal to the plane of incidence is called s -polarized (senkrecht, German term for perpendicular) while the light with its polarization along the plane of incidence is denoted as p -polarized (parallel).

For isotropic samples, the independence of s - and p - polarizations implies that the Jones matrix is diagonal and can be written in the form:

$$\mathbf{J} = \begin{bmatrix} r_{ss} & 0 \\ 0 & r_{pp} \end{bmatrix}, \quad (3.35)$$

where r_{ss} and r_{pp} are the complex Fresnel coefficients for reflection.

Although the 2×2 Jones formalism provides an efficient method to describe fully polarized light, it is not sufficient for description of depolarizing devices. As mentioned above, any partially polarized state can be described by the Stokes vector which is given by Eq. (3.32). Upon interaction of incident light \mathbf{S}_{in} with a sample, transformation of such partially polarized light into \mathbf{S}_{out} can be described by the linear transformation:

$$\mathbf{S}_{out} = \mathbf{M}\mathbf{S}_{in}, \quad (3.36)$$

where \mathbf{M} is the 4×4 Mueller matrix. Although the Stokes vector is directly related to the light intensities and thus the Mueller matrix does not (in contrast to the Jones matrix) contain any information about the overall phase shift, it can fully characterize the polarization response of any depolarizing or non-depolarizing sample. In the case of the absence of the depolarization, both formalism are equivalent and simple Jones-Mueller matrix conversion is possible via the following relationship [74]:

$$\mathbf{M} = \mathcal{A}(\mathbf{J} \otimes \mathbf{J}^*)\mathcal{A}^{-1}, \quad (3.37)$$

where \otimes denotes the Kronecker product and \mathcal{A} is defined as:

$$\mathcal{A} = \begin{bmatrix} 1 & 0 & 0 & 1 \\ 1 & 0 & 0 & -1 \\ 0 & 1 & 1 & 0 \\ 0 & i & -i & 0 \end{bmatrix}. \quad (3.38)$$

Considering the anisotropic non-depolarizing sample described by the Jones matrix (3.34), the full Jones-Mueller matrix is in the form:

$$\mathbf{M} = \begin{bmatrix} \frac{1}{2}(|J_{ss}|^2 + |J_{sp}|^2 + |J_{ps}|^2 + |J_{pp}|^2) & \frac{1}{2}(|J_{ss}|^2 - |J_{sp}|^2 + |J_{ps}|^2 - |J_{pp}|^2) & \Re(J_{sp}J_{ss}^* + J_{pp}J_{ps}^*) & -\Im(J_{sp}J_{ss}^* + J_{pp}J_{ps}^*) \\ \frac{1}{2}(|J_{ss}|^2 + |J_{sp}|^2 - |J_{ps}|^2 - |J_{pp}|^2) & \frac{1}{2}(|J_{ss}|^2 - |J_{sp}|^2 - |J_{ps}|^2 + |J_{pp}|^2) & \Re(J_{sp}J_{ss}^* - J_{pp}J_{ps}^*) & \Im(-J_{sp}J_{ss}^* + J_{pp}J_{ps}^*) \\ \Re(J_{ps}J_{ss}^* + J_{pp}J_{sp}^*) & \Re(J_{ps}J_{ss}^* - J_{pp}J_{sp}^*) & \Re(J_{pp}J_{ss}^* + J_{ps}J_{sp}^*) & \Im(-J_{pp}J_{ss}^* + J_{ps}J_{sp}^*) \\ \Im(J_{ps}J_{ss}^* + J_{pp}J_{sp}^*) & \Im(J_{ps}J_{ss}^* - J_{pp}J_{sp}^*) & \Im(J_{pp}J_{ss}^* + J_{ps}J_{sp}^*) & \Re(J_{pp}J_{ss}^* - J_{ps}J_{sp}^*) \end{bmatrix}. \quad (3.39)$$

Linear birefringence

Let us consider linearly birefringent medium with thickness l through which the wave with the wavelength λ is propagating. The principal axes are along x and y directions and the anisotropic medium is described by real refraction indices n_x and n_y . Description of the change of the polarization state during propagation can be done using the Jones matrix:

$$\mathbf{J}_{\text{LB}} = \begin{bmatrix} e^{-i\frac{2\pi}{\lambda}n_x l} & 0 \\ 0 & e^{-i\frac{2\pi}{\lambda}n_y l} \end{bmatrix} = e^{-i\frac{2\pi}{\lambda}\bar{n}l} \begin{bmatrix} e^{-iLB/2} & 0 \\ 0 & e^{iLB/2} \end{bmatrix}, \quad (3.40)$$

where $LB = \frac{2\pi}{\lambda}(n_x - n_y)l$ describes the linear birefringence and $\bar{n} = (n_x + n_y)/2$ is the average real part of optical index, while the matrix prefactor represents an overall phase delay. The Jones-Mueller matrix is then according to (3.39) in the form:

$$\mathbf{M}_{\text{LB}} = \begin{bmatrix} 1 & 0 & 0 & 0 \\ 0 & 1 & 0 & 0 \\ 0 & 0 & \cos(LB) & -\sin(LB) \\ 0 & 0 & \sin(LB) & \cos(LB) \end{bmatrix} \stackrel{LB \ll 1}{\approx} \begin{bmatrix} 1 & 0 & 0 & 0 \\ 0 & 1 & 0 & 0 \\ 0 & 0 & 1 & -LB \\ 0 & 0 & LB & 1 \end{bmatrix}, \quad (3.41)$$

which shows that $M_{34} = -M_{43}$ are the most important elements revealing the optical linear birefringence.

Linear dichroism

Linearly dichroic medium is a medium in which linearly polarized waves along x and y directions are attenuated differently. Such effect can be described by the Jones matrix in the form:

$$\mathbf{J}_{\text{LD}} = \begin{bmatrix} e^{-i\frac{2\pi}{\lambda}(n-ik_x)l} & 0 \\ 0 & e^{-i\frac{2\pi}{\lambda}(n-ik_y)l} \end{bmatrix} = e^{-i\frac{2\pi}{\lambda}nl} e^{-\frac{2\pi}{\lambda}\bar{k}l} \begin{bmatrix} e^{-LD/2} & 0 \\ 0 & e^{LD/2} \end{bmatrix} \quad (3.42)$$

where $LD = \frac{2\pi}{\lambda}(k_x - k_y)l$ describes the linear dichroism and $\bar{k} = (k_x + k_y)/2$ is the average imaginary part of optical index, while the matrix prefactors represents an overall phase delay and absorption. The Jones-Mueller matrix is then according to (3.39) in the form:

$$\mathbf{M}_{\text{LD}} = e^{-\frac{4\pi}{\lambda}\bar{k}l} \begin{bmatrix} \cosh(LD) & -\sinh(LD) & 0 & 0 \\ -\sinh(LD) & \cosh(LD) & 0 & 0 \\ 0 & 0 & 1 & 0 \\ 0 & 0 & 0 & 1 \end{bmatrix} \stackrel{LD \ll 1}{\approx} e^{-\frac{4\pi}{\lambda}\bar{k}l} \begin{bmatrix} 1 & -LD & 0 & 0 \\ -LD & 1 & 0 & 0 \\ 0 & 0 & 1 & 0 \\ 0 & 0 & 0 & 1 \end{bmatrix} \quad (3.43)$$

which shows the $M_{12} = M_{21}$ the most important elements revealing the optical linear dichroism.

3.2 Electromagnetic field in anisotropic multilayer structure

The electromagnetic response of generally anisotropic multilayer structure can be calculated in the following steps: I) solving of the wave equation (3.22) derived in Sec. 3.1 for each generally anisotropic layer, II) including the boundary conditions at interfaces, and III) calculation of the Jones matrix, the Mueller matrix or ellipsometric angles upon reflection or transmission from the structure.

3.2.1 Solution of the Maxwell equation in anisotropic medium

Let us consider an anisotropic multilayer structure consisting of N -anisotropic layers characterized by permittivity tensors $\hat{\varepsilon}^{(n)}$ and the thicknesses $d^{(n)}$, with $n = 1, \dots, N$. The surrounding media are denoted by (0) for superstrate and $(N + 1)$ for substrate as depicted in Fig. 3.5. The interface planes are normal to a common axis parallel to the z axis of the Cartesian coordinate system. The wave equation (3.22) for each layer can be written in the following form [75, 76]:

$$k_0^2 \hat{\varepsilon}^{(n)} \mathbf{E}_0^{(n)} - \mathbf{k}^{2(n)} \mathbf{E}_0^{(n)} + \mathbf{k}^{(n)} [\mathbf{k}^{(n)} \mathbf{E}_0^{(n)}] = 0, \quad (3.44)$$

where $\mathbf{E}_0^{(n)}$ is the amplitude of the electric field in each layer $\mathbf{E}^{(n)} = \mathbf{E}_0^{(n)} e^{i(\omega t - \mathbf{k}^{(n)} \cdot \mathbf{r})}$. Because of the Snell law, the wave propagates in each medium with the same tangential component of the wave vector $\mathbf{k}^{(n)} = k_0(N_x \hat{\mathbf{x}} + N_y \hat{\mathbf{y}} + N_z^{(n)} \hat{\mathbf{z}})$. Let us choose coordinate system, for which $N_x = 0$ and $N_y = n^{(n)} \sin \theta^{(n)} = \text{const.}$, where $\theta^{(n)}$ is the propagation angle in the (n) -th layer, and rewrite the wave equation (3.44) in the matrix form:

$$\underbrace{\begin{pmatrix} \varepsilon_{xx}^{(n)} - N_y^2 - N_z^{(n)2} & \varepsilon_{xy}^{(n)} & \varepsilon_{xz}^{(n)} \\ \varepsilon_{yx}^{(n)} & \varepsilon_{yy}^{(n)} - N_z^{(n)2} & \varepsilon_{yz}^{(n)} + N_y N_z^{(n)} \\ \varepsilon_{zx}^{(n)} & \varepsilon_{zy}^{(n)} + N_y N_z^{(n)} & \varepsilon_{zz}^{(n)} - N_y^2 \end{pmatrix}}_{\spadesuit} \begin{bmatrix} E_{0x}^{(n)} \\ E_{0y}^{(n)} \\ E_{0z}^{(n)} \end{bmatrix} = 0, \quad (3.45)$$

where the condition for existence of nontrivial solution is ensured by fourth-order algebraic equation:

$$\det(\spadesuit) = 0. \quad (3.46)$$

Four solutions with $N_{zj}^{(n)}$, where $(j = 1, 3)$ and $(j = 2, 4)$, correspond to the forward and backward propagating modes called eigen-modes. The eigenmode polarizations $\mathbf{E}_{0j}^{(n)}$ are specific for each media and do not change during the propagation and take the form:

$$\mathbf{E}_{0j}^{(n)} = A_j^{(n)} \mathbf{e}_j^{(n)}, \quad (3.47)$$

where $A_j^{(n)}$ is the amplitude of particular wave and $\mathbf{e}_j^{(n)}$ is the normalized eigen-polarization satisfying:

$$\left[\mathbf{e}_j^{(n)} \right]^+ \mathbf{e}_j^{(n)} = 1, \quad (3.48)$$

where $\left[\mathbf{e}_j^{(n)} \right]^+$ denotes the Hermitian adjoint. In a similar way, the magnetic field vector $\mathbf{H}_{0j}^{(n)}$ can be expressed as

$$\mathbf{H}_{0j}^{(n)} = \sqrt{\frac{\varepsilon_0}{\mu_0}} A_j^{(n)} \mathbf{h}_j^{(n)}, \quad (3.49)$$

where $\mathbf{h}_j^{(n)}$ is the magnetic eigen-polarization. Inside n -th layer at the interface $n/n+1$, we express the field vector $\mathbf{E}^{(n)}$ as a linear combination of these eigen-polarizations:

$${}^{(n/n+1)}\mathbf{E}^{(n)} = \sum_{j=1}^4 A_j^{(n)} \mathbf{e}_j^{(n)}. \quad (3.50)$$

During the propagation in the n -th layer change the field vector according to a factor $\exp \left[ik_0 N_{zj}^{(n)} d^{(n)} \right]$ as depicted in Fig 3.6. Then the field vector at the $(n-1/n)$ interface can be expressed as:

$${}^{(n-1/n)}\mathbf{E}^{(n)} = \sum_{j=1}^4 A_j^{(n)} \mathbf{e}_j^{(n)} \exp \left[ik_0 N_{zj}^{(n)} d^{(n)} \right]. \quad (3.51)$$

3.2.2 Boundary conditions at interfaces

The boundary conditions require continuity of the tangential components of the field vectors \mathbf{E} and \mathbf{H} at the interface:

$$\begin{aligned} {}^{(n-1/n)}\mathbf{E}_x^{(n)} &= {}^{(n-1/n)}\mathbf{E}_x^{(n-1)}, & {}^{(n-1/n)}\mathbf{E}_y^{(n)} &= {}^{(n-1/n)}\mathbf{E}_y^{(n-1)}, \\ {}^{(n-1/n)}\mathbf{H}_x^{(n)} &= {}^{(n-1/n)}\mathbf{H}_x^{(n-1)}, & {}^{(n-1/n)}\mathbf{H}_y^{(n)} &= {}^{(n-1/n)}\mathbf{H}_y^{(n-1)}. \end{aligned}$$

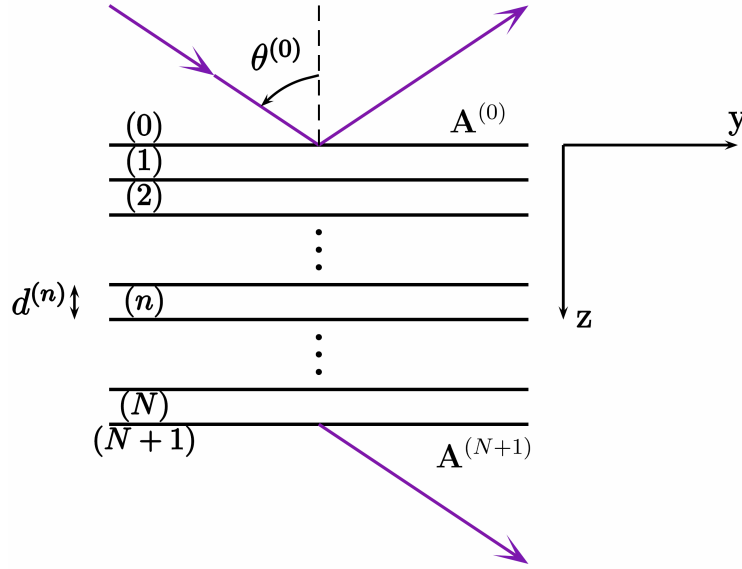


Figure 3.5: Multilayer structure embedded in isotropic halfspaces (0) and $(N + 1)$. Each layer is characterized by the permittivity tensor $\hat{\epsilon}^{(n)}$ and the thickness $d^{(n)}$.

From Eq (3.50) and Eq. (3.51) follows, that these conditions can be expressed as:

$$\sum_{j=1}^4 A_j^{(n-1)} \mathbf{e}_{xj}^{(n-1)} = \sum_{j=1}^4 A_j^{(n)} \mathbf{e}_{xj}^{(n)} \exp \left[ik_0 N_{zj}^{(n)} d^{(n)} \right], \quad (3.52)$$

$$\sum_{j=1}^4 A_j^{(n-1)} \mathbf{h}_{yj}^{(n-1)} = \sum_{j=1}^4 A_j^{(n)} \mathbf{h}_{yj}^{(n)} \exp \left[ik_0 N_{zj}^{(n)} d^{(n)} \right], \quad (3.53)$$

$$\sum_{j=1}^4 A_j^{(n-1)} \mathbf{e}_{yj}^{(n-1)} = \sum_{j=1}^4 A_j^{(n)} \mathbf{e}_{yj}^{(n)} \exp \left[ik_0 N_{zj}^{(n)} d^{(n)} \right], \quad (3.54)$$

$$\sum_{j=1}^4 A_j^{(n-1)} \mathbf{h}_{xj}^{(n-1)} = \sum_{j=1}^4 A_j^{(n)} \mathbf{h}_{xj}^{(n)} \exp \left[ik_0 N_{zj}^{(n)} d^{(n)} \right], \quad (3.55)$$

and in the matrix form:

$$\mathbf{D}^{(n-1)} \mathbf{A}^{(n-1)} = \mathbf{D}^{(n)} \mathbf{P}^{(n)} \mathbf{A}^{(n)},$$

where $\mathbf{D}^{(n)}$ (the dynamic matrix) and $\mathbf{P}^{(n)}$ (the propagation matrix) have the following form

$$\mathbf{D}^{(n)} = \begin{pmatrix} \mathbf{e}_{x1}^{(n)} & \mathbf{e}_{x2}^{(n)} & \mathbf{e}_{x3}^{(n)} & \mathbf{e}_{x4}^{(n)} \\ \mathbf{h}_{y1}^{(n)} & \mathbf{h}_{y2}^{(n)} & \mathbf{h}_{y3}^{(n)} & \mathbf{h}_{y4}^{(n)} \\ \mathbf{e}_{y1}^{(n)} & \mathbf{e}_{y2}^{(n)} & \mathbf{e}_{y3}^{(n)} & \mathbf{e}_{y4}^{(n)} \\ \mathbf{h}_{x1}^{(n)} & \mathbf{h}_{x2}^{(n)} & \mathbf{h}_{x3}^{(n)} & \mathbf{h}_{x4}^{(n)} \end{pmatrix}, \quad \mathbf{A}^{(n)} = \begin{bmatrix} A_1^{(n)} \\ A_2^{(n)} \\ A_3^{(n)} \\ A_4^{(n)} \end{bmatrix} \quad (3.56)$$

$$\mathbf{P}^{(n)} = \begin{pmatrix} ik_0 N_{z1}^{(n)} d^{(n)} & 0 & 0 & 0 \\ 0 & ik_0 N_{z2}^{(n)} d^{(n)} & 0 & 0 \\ 0 & 0 & ik_0 N_{z3}^{(n)} d^{(n)} & 0 \\ 0 & 0 & 0 & ik_0 N_{z4}^{(n)} d^{(n)} \end{pmatrix}. \quad (3.57)$$

Using $\mathbf{P}^{(n)}$ and $\mathbf{D}^{(n)}$, the amplitudes in the halfspaces (0) and $(N+1)$ can be related as follows:

$$\mathbf{A}^{(0)} = \underbrace{[\mathbf{D}^{(0)}]^{-1} \mathbf{D}^{(1)} \mathbf{P}^{(1)} \dots [\mathbf{D}^{(N)}]^{-1} \mathbf{D}^{(N+1)} \mathbf{P}^{(N+1)}}_{\mathbf{M}} \mathbf{A}^{(N+1)}, \quad (3.58)$$

where \mathbf{M} is the total transfer matrix of the system.

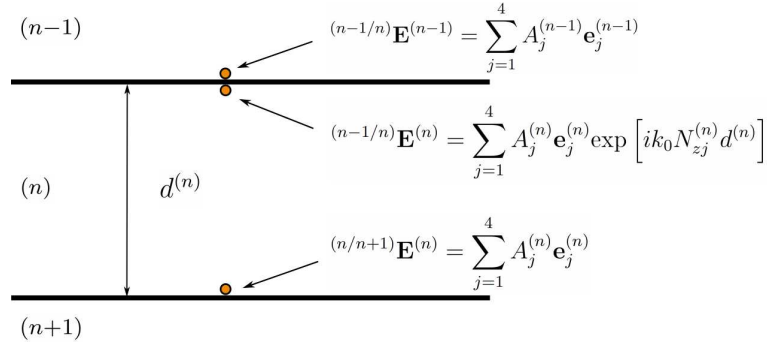


Figure 3.6: Transfer matrix relates the proper polarization fields of amplitudes $A_j^{(n)}$ in the layer (n) and $(n+1)$.

Note, that in the case of isotropic layered media, the electromagnetic field can be divided into two uncoupled modes: s -modes and p -modes with electric field vector perpendicular and parallel to the plane of incidence, respectively. Since they are uncoupled, characteristic equation for $N_{z,j}^{(n)}$ is biquadratic with the solution:

$$N_{z,1,3}^{(n)} = -N_{z,2,4}^{(n)} = n^{(n)} \cos \theta^{(n)}, \quad (3.59)$$

and the dynamic matrix takes the block diagonal form:

$$\mathbf{D} = \begin{pmatrix} 1 & 1 & 0 & 0 \\ n^{(n)} \cos \theta^{(n)} & -n^{(n)} \cos \theta^{(n)} & 0 & 0 \\ 0 & 0 & \cos \theta^{(n)} & \cos \theta^{(n)} \\ 0 & 0 & -n^{(n)} & n^{(n)} \end{pmatrix}. \quad (3.60)$$

3.2.3 Scattering matrix formalism

While the transfer matrix formalism provides an effective tool for the calculation of the electromagnetic response of multilayer anisotropic structures, we explain later, that it can not be used for recursive calculation of the gain tensor in active laser structure with multiple active QWs. For this reason we introduce the scattering matrix formalism, whose approach is depicted in Fig. 3.7. While the transfer matrix \mathbf{M} in Eq. (3.58) relates the upper and lower field amplitudes, the scattering matrix (S-matrix) is defined using the amplitudes of the waves incoming toward ($\mathbf{A}_{\text{down}}^{(0)}$, $\mathbf{A}_{\text{up}}^{(N+1)}$) and outgoing from the structure ($\mathbf{A}_{\text{up}}^{(0)}$, $\mathbf{A}_{\text{down}}^{(N+1)}$). Let us rewrite Eq. (3.58) in more compact form:

$$\begin{bmatrix} \mathbf{A}_{\text{up}}^{(0)} \\ \mathbf{A}_{\text{down}}^{(0)} \end{bmatrix} = \begin{bmatrix} \mathbf{M}_{\text{uu}} & \mathbf{M}_{\text{ud}} \\ \mathbf{M}_{\text{du}} & \mathbf{M}_{\text{dd}} \end{bmatrix} \begin{bmatrix} \mathbf{A}_{\text{up}}^{(N+1)} \\ \mathbf{A}_{\text{down}}^{(N+1)} \end{bmatrix}, \quad (3.61)$$

where the amplitude vectors corresponding to two orthogonal polarizations $\mathbf{A}_{\text{down}}^{(0)} = [A_1^{(0)}; A_3^{(0)}]^T$, $\mathbf{A}_{\text{up}}^{(0)} = [A_2^{(0)}; A_4^{(0)}]^T$ and \mathbf{M}_{kl} denotes the 2×2 sub-matrices.

Then the amplitudes of the waves incoming toward and outgoing from the structure are connected by the scattering matrix \mathbf{S} :

$$\begin{bmatrix} \mathbf{A}_{\text{up}}^{(0)} \\ \mathbf{A}_{\text{down}}^{(N+1)} \end{bmatrix} = \underbrace{\begin{bmatrix} \mathbf{S}_{\text{uu}} & \mathbf{S}_{\text{ud}} \\ \mathbf{S}_{\text{du}} & \mathbf{S}_{\text{dd}} \end{bmatrix}}_{\mathbf{S}} \begin{bmatrix} \mathbf{A}_{\text{up}}^{(N+1)} \\ \mathbf{A}_{\text{down}}^{(0)} \end{bmatrix}, \quad (3.62)$$

where

$$\mathbf{S} = \begin{bmatrix} \mathbf{M}_{\text{uu}} - \mathbf{M}_{\text{ud}}\mathbf{M}_{\text{dd}}^{-1}\mathbf{M}_{\text{du}} & \mathbf{M}_{\text{ud}}\mathbf{M}_{\text{dd}}^{-1} \\ \mathbf{M}_{\text{dd}}^{-1}\mathbf{M}_{\text{du}} & \mathbf{M}_{\text{dd}}^{-1} \end{bmatrix}. \quad (3.63)$$

We will intensively use this relationship in Chapter 5 dealing with the description of the spin-lasers properties.

3.2.4 Reflection coefficients

Eq. (3.58) provides the complete information about the electromagnetic response of the anisotropic multilayer structure. Let us choose the eigenmodes of the incident light in isotropic superstrate (0) perpendicular to the plane of incidence (s -polarized) and parallel to the plane of incidence (p -polarized). The relations between the incident and the reflected electric field amplitudes can be expressed in the form of 2×2 Jones reflection matrix:

$$\mathbf{J} = \begin{bmatrix} r_{ss} & r_{sp} \\ r_{ps} & r_{pp} \end{bmatrix}, \quad (3.64)$$

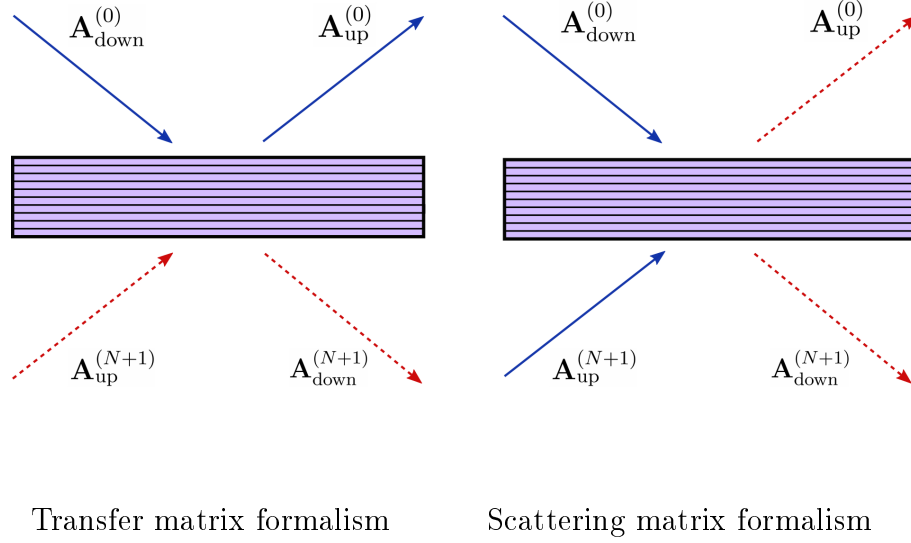


Figure 3.7: Comparison between the transfer matrix and the scattering matrix formalism.

where for s -polarized incident wave ($A_3^{(0)} = 0$):

$$r_{ss} = \frac{A_2^{(0)}}{A_1^{(0)}} = \frac{M_{21}M_{33} - M_{23}M_{31}}{M_{11}M_{33} - M_{13}M_{31}}, \quad (3.65)$$

$$r_{sp} = \frac{A_4^{(0)}}{A_1^{(0)}} = \frac{M_{41}M_{33} - M_{43}M_{31}}{M_{11}M_{33} - M_{13}M_{31}}, \quad (3.66)$$

and for p -polarized incident wave ($A_1^{(0)} = 0$):

$$r_{ps} = -\frac{A_2^{(0)}}{A_3^{(0)}} = \frac{M_{13}M_{21} - M_{11}M_{23}}{M_{11}M_{33} - M_{13}M_{31}}, \quad (3.67)$$

$$r_{pp} = -\frac{A_4^{(0)}}{A_3^{(0)}} = \frac{M_{13}M_{41} - M_{11}M_{43}}{M_{11}M_{33} - M_{13}M_{31}}. \quad (3.68)$$

Note, that the reflection coefficients are generally complex numbers with amplitudes $|r_{pq}|$ and the absolute phases δ_{pq} , where subscripts (p, q) refers to (s, p) polarizations, and can be written in the form:

$$r_{pq} = |r_{pq}| \exp[i\delta_{pq}]. \quad (3.69)$$

3.2.5 Reflection coefficients with local anisotropic layers

In this subsection we propose to connect the change of the reflectivity due to the local anisotropic layers measured by reflectance anisotropy spectroscopy (RAS). Let us consider the light with normal incidence $\theta^{(0)} = 0$ on the multilayer structure,

while each uniaxial anisotropic layer with thickness $d^{(n)}$ can be described by the permittivity components $\varepsilon_{xx}^{(n)}$ and $\varepsilon_{yy}^{(n)}$. The dynamical matrix of each layer is in the simplified form:

$$\mathbf{D}^{(n)} = \begin{bmatrix} \mathbf{D}_{xx}^{(n)} & \mathbf{0} \\ \mathbf{0} & \mathbf{D}_{yy}^{(n)} \end{bmatrix} = \begin{bmatrix} 1 & 1 & 0 & 0 \\ \sqrt{\varepsilon_{xx}^{(n)}} & -\sqrt{\varepsilon_{xx}^{(n)}} & 0 & 0 \\ 0 & 0 & 1 & 1 \\ 0 & 0 & -\sqrt{\varepsilon_{yy}^{(n)}} & \sqrt{\varepsilon_{yy}^{(n)}} \end{bmatrix}, \quad (3.70)$$

while the transfer matrix of each layer is according to (3.58) in the form

$$\mathbf{T}^{(n)} = \frac{1}{2} \begin{bmatrix} 1 & 1 & 0 & 0 \\ \sqrt{\varepsilon_{xx}^{(n)}} & -\sqrt{\varepsilon_{xx}^{(n)}} & 0 & 0 \\ 0 & 0 & 1 & 1 \\ 0 & 0 & -\sqrt{\varepsilon_{yy}^{(n)}} & \sqrt{\varepsilon_{yy}^{(n)}} \end{bmatrix} \begin{bmatrix} e^{ik_0\sqrt{\varepsilon_{xx}^{(n)}}d^{(n)}} & 0 & 0 & 0 \\ 0 & e^{-ik_0\sqrt{\varepsilon_{xx}^{(n)}}d^{(n)}} & 0 & 0 \\ 0 & 0 & e^{ik_0\sqrt{\varepsilon_{yy}^{(n)}}d^{(n)}} & 0 \\ 0 & 0 & 0 & e^{ik_0\sqrt{\varepsilon_{yy}^{(n)}}d^{(n)}} \end{bmatrix} \begin{bmatrix} 1 & \frac{1}{\sqrt{\varepsilon_{xx}^{(n)}}} & 0 & 0 \\ 1 & -\frac{1}{\sqrt{\varepsilon_{xx}^{(n)}}} & 0 & 0 \\ 0 & 0 & 1 & -\frac{1}{\sqrt{\varepsilon_{yy}^{(n)}}} \\ 0 & 0 & 1 & \frac{1}{\sqrt{\varepsilon_{yy}^{(n)}}} \end{bmatrix}.$$

This matrix can be rewritten as

$$\mathbf{T}^{(n)} = \begin{bmatrix} \cos k_0\sqrt{\varepsilon_{xx}^{(n)}}d^{(n)} & \frac{i}{\varepsilon_{xx}^{(n)}}\sin k_0\sqrt{\varepsilon_{xx}^{(n)}}d^{(n)} & 0 & 0 \\ i\varepsilon_{xx}^{(n)}\sin k_0\sqrt{\varepsilon_{xx}^{(n)}}d^{(n)} & \cos k_0\sqrt{\varepsilon_{xx}^{(n)}}d^{(n)} & 0 & 0 \\ 0 & 0 & \cos k_0\sqrt{\varepsilon_{yy}^{(n)}}d^{(n)} & -\frac{i}{\varepsilon_{xx}^{(n)}}\sin k_0\sqrt{\varepsilon_{xx}^{(n)}}d^{(n)} \\ 0 & 0 & -i\varepsilon_{xx}^{(n)}\sin k_0\sqrt{\varepsilon_{xx}^{(n)}}d^{(n)} & \cos k_0\sqrt{\varepsilon_{yy}^{(n)}}d^{(n)} \end{bmatrix} \approx_{k_0\sqrt{\varepsilon_{xx,yy}^{(n)}}d^{(n)} \ll 1} \begin{bmatrix} 1 & ik_0d^{(n)} & 0 & 0 \\ ik_0\varepsilon_{xx}^{(n)}d^{(n)} & 1 & 0 & 0 \\ 0 & 0 & 1 & -ik_0d^{(n)} \\ 0 & 0 & -ik_0\varepsilon_{yy}^{(n)}d^{(n)} & 1 \end{bmatrix}, \quad (3.71)$$

where we consider approximation for ultra-thin layer $k_0\sqrt{\varepsilon_{xx,yy}^{(n)}}d^{(n)} \ll 1$. This approach can be generalized for multiple anisotropic layer according to

$$\prod_{i=1}^N \mathbf{T}^{(i)} = \begin{bmatrix} 1 & ik_0\sum d^{(i)} & 0 & 0 \\ ik_0\sum \varepsilon_{xx}^{(i)}d^{(i)} & 1 & 0 & 0 \\ 0 & 0 & 1 & -ik_0\sum d^{(i)} \\ 0 & 0 & -ik_0\sum \varepsilon_{yy}^{(i)}d^{(i)} & 1 \end{bmatrix}, \quad (3.72)$$

so that the total transfer matrix of the system is given by

$$\mathbf{M} = [\mathbf{D}^{(0)}]^{-1} \prod_{i=1}^N \mathbf{T}^{(i)} \mathbf{D}^{(N+1)}, \quad (3.73)$$

where $\mathbf{D}^{(0)}$ and $\mathbf{D}^{(N+1)}$ are the dynamical matrices of superstrate (air) and substrate, respectively.

Let us now consider one anisotropic ultra-thin layer with the optical constants $\varepsilon_{xx} = \varepsilon$ and $\varepsilon_{yy} = \varepsilon + \Delta\varepsilon$, and thickness $d^{(n)}$, which is embedded between substrate with the optical constant ε and air with $\varepsilon_0 = 1$. Then the reflection coefficients are calculated according to (3.65), (3.68), and (3.73)

$$r_{xx} = r = \frac{M_{21}}{M_{11}} = \frac{1 - \sqrt{\varepsilon}}{1 + \sqrt{\varepsilon}} \quad (3.74)$$

$$r_{yy} = r - \Delta r = -\frac{M_{43}}{M_{33}} = \frac{1 - \sqrt{\varepsilon} - ik_0 \Delta\varepsilon d}{1 + \sqrt{\varepsilon} + ik_0 \Delta\varepsilon d}, \quad (3.75)$$

where the first relation is the well-known Fresnel equation and the second equation describes different reflection due to the anisotropic term $\Delta\varepsilon$. Then the difference in reflectivity $\Delta r = r_{xx} - r_{yy}$ normalized to the mean reflectance $r = (r_{xx} + r_{yy})/2$ is given by

$$\frac{\Delta r}{r} = \frac{-2ikd \Delta\varepsilon}{\varepsilon - 1 \varepsilon}. \quad (3.76)$$

This equation can be also derived by approximate solution of the Helmholtz equation [77] for thin anisotropic film and is widely used for an interpretation of reflectance anisotropy spectroscopy and for the extraction of optical constants of layers with local anisotropies such as with surface strain [78]. One can connect this analysis to the measurement of InGaAs/GaAs quantum well system measured by Yu [38], where $\Delta r/r \approx 10^{-4}$ for 7 nm and $\lambda \approx 1\mu\text{m}$ gives order of the anisotropy magnitude $|\Delta\varepsilon| \approx 0.05$, which is in a good agreement with ellipsometric analysis described in Chapter 4.

3.2.6 Ellipsometric angles

In ellipsometry measurements, the polarization states of incident and reflected light are described by the coordinates of *s*- and *p*-polarizations. Upon light reflection both polarizations exhibit different changes in amplitude and phase which can be in the case of isotropic non-depolarizing sample conveniently described by using two ellipsometric angles Ψ and Δ by the following relation:

$$\frac{r_{pp}}{r_{ss}} = \tan \Psi \exp(i\Delta), \quad (3.77)$$

where $\tan \Psi = |r_{pp}|/|r_{ss}|$ corresponds to the amplitude ratio and $\Delta = \delta_p - \delta_s$ denotes the difference in phase shift upon reflection. On the other hand for anisotropic

sample, the off-diagonal elements of the Jones matrix (3.64) appears:

$$\mathbf{J} \propto \begin{bmatrix} 1 & \frac{r_{sp}}{r_{ss}} \\ \frac{r_{ps}}{r_{ss}} & \frac{r_{pp}}{r_{ss}} \end{bmatrix}, \quad (3.78)$$

where

$$\frac{r_{sp}}{r_{ss}} = \tan \psi_{sp} \exp(i\Delta_{sp}), \quad (3.79)$$

$$\frac{r_{ps}}{r_{ss}} = \tan \psi_{ps} \exp(i\Delta_{ps}), \quad (3.80)$$

and ψ_{sp} , ψ_{ps} , Δ_{sp} , Δ_{ps} are the generalized ellipsometric angles [74, 79]. Accordingly, the Jones matrix of anisotropic sample is characterized by six independent parameters instead of only two parameters for an isotropic structure.

3.3 Mueller matrix ellipsometry

The Mueller matrix ellipsometry has been widely applied for optical characterization of optically anisotropic structures. The important feature of this kind of ellipsometry is its ability to directly measure the Mueller matrix components corresponding to a sample [79, 80]. Moreover, in comparison to generalized spectroscopic ellipsometry, the Mueller matrix ellipsometry can be used to extract the depolarization effects of a sample originating from incoherent superposition of different polarization states upon transmission or reflection from the sample. More details about the measurement procedure are given in next chapter supported by experimental results obtained on real laser structures. In this section we will compare the Mueller matrix ellipsometry with widely used techniques such as reflectance anisotropy spectroscopy and standard spectroscopic ellipsometry and we will point out the benefits of this method.

3.3.1 Comparison of Mueller matrix ellipsometry with reflectance anisotropy spectroscopy (RAS)

Another widely used technique sensitive to anisotropic optical response of surface reconstructions, strain, and interface bonds is reflectance anisotropy spectroscopy (RAS) [81], which measures the difference in reflectance ($\Delta r = r_{xx} - r_{yy}$) of normal incidence linearly-polarized light between two orthogonal directions normalized to the mean reflectance $r = (r_{xx} + r_{yy})/2$:

$$\frac{\Delta r}{r} = 2 \frac{r_{xx} - r_{yy}}{r_{xx} + r_{yy}}, \quad (3.81)$$

while the Jones vector is given by:

$$\mathbf{J} = \begin{bmatrix} r_{xx} & 0 \\ 0 & r_{yy} \end{bmatrix}. \quad (3.82)$$

The simplest RAS spectrometer based on **the intensity modulation** has been designed by Aspnes [82], where linearly polarized light is incident on a sample rotating with angular frequency ω_s . Then the intensity of the light reflected by the sample is:

$$I_{RAS} \propto R - \frac{\Delta R}{2} \cos 2\omega_s t, \quad (3.83)$$

where R and ΔR represents, respectively, the average and the anisotropy of the reflected intensities given by:

$$R = \frac{|r_{xx}|^2 + |r_{yy}|^2}{2}, \quad (3.84)$$

and

$$\Delta R = |r_{xx}|^2 - |r_{yy}|^2. \quad (3.85)$$

The measured ratio the oscillatory $I_{2\omega}$ and time-independent contribution I_0 to the reflected intensity is a direct measure of $\Delta R/R$:

$$\frac{I_{2\omega}}{I_0} = \frac{1}{2\sqrt{2}} \frac{\Delta R}{R}, \quad (3.86)$$

while for small anisotropies:

$$\frac{\Delta R}{R} \approx 2\Re\left(\frac{\Delta r}{r}\right). \quad (3.87)$$

This measured quantity is directly included in Mueller matrix components M_{12} and M_{21} . Considering the Jones vector in the form of (3.82), the Mueller matrix (3.39) can be expressed as:

$$\mathbf{M} = \begin{bmatrix} \frac{1}{2}(|r_{xx}|^2 + |r_{yy}|^2) & \frac{1}{2}(|r_{xx}|^2 - |r_{yy}|^2) & 0 & 0 \\ \frac{1}{2}(|r_{xx}|^2 - |r_{yy}|^2) & \frac{1}{2}(|r_{xx}|^2 + |r_{yy}|^2) & 0 & 0 \\ 0 & 0 & \Re(r_{yy}r_{xx}^*) & \Im(-r_{yy}r_{xx}^*) \\ 0 & 0 & \Im(r_{yy}r_{xx}^*) & \Re(r_{yy}r_{xx}^*) \end{bmatrix}. \quad (3.88)$$

One can clearly see the connection of $M_{12} = M_{21}$ to $\Delta R/R$ given by:

$$m_{21} = \frac{M_{21}}{M_{11}} = \frac{\Delta R}{2R} \quad m_{12} = \frac{M_{12}}{M_{11}} = \frac{\Delta R}{2R}, \quad (3.89)$$

where m_{12} and m_{21} are normalized Mueller matrix components. The main disadvantage of the RAS spectroscopy based on the intensity modulation is unsuitability for the implementation in in-situ real-time measurement because of a need for the sample rotation. Moreover, it only enables the measurements of the real part of the complex quantity $\Delta r/r$.

An improved way for RAS measurements, which has become popular, is based on photoelastic **phase modulation** [81], where one linear polarization, perpendicular to modulation axis is unaffected by modulator, but the polarization along the

modulation axis undergoes an oscillatory retardation Γ_r with the frequency ω_r and the amplitude $\Gamma_{r,0}$:

$$\Gamma_r = \Gamma_{r,0} \sin(\omega_r t). \quad (3.90)$$

Then the measured intensity is in the form of harmonic series $I_{RAS} = I_0 + I_\omega + I_{2\omega} + \dots$, where I_0 is time-independent contribution and remaining terms are oscillatory contribution with angular frequencies indicated by subscripts. Real and imaginary parts of the $\Delta r/r$ are now included in the measured intensities, particularly in the ratios $I_{m\omega}/I_0$:

$$\frac{I_{m\omega}}{I_0} = \frac{2J_m(\Gamma_{r,0}) \Re(\Delta r/r)}{1 + |\Delta r/r|^2/4} \approx 2J_m(\Gamma_{r,0}) \Re\left(\frac{\Delta r}{r}\right), \quad (3.91)$$

where $J_m(\Gamma_{r,0})$ is a Bessel function of order m (even integer), and

$$\frac{I_{m\omega}}{I_0} = \frac{2J_m(\Gamma_{r,0}) \Im(\Delta r/r)}{1 + |\Delta r/r|^2/4} \approx 2J_m(\Gamma_{r,0}) \Im\left(\frac{\Delta r}{r}\right), \quad (3.92)$$

where m is an odd integer. The possibility of a measurement of the imaginary part $\Delta r/r$ brings greater information about structure including phase changes upon a reflection.

The connection between the imaginary part of $\Delta r/r$ and the Mueller matrix is straightforward. One can easily proof that for small anisotropies we obtain:

$$m_{34} = -m_{43} = \frac{M_{34}}{M_{11}} = -\frac{M_{43}}{M_{11}} = \frac{2\Im(-r_{yy}r_{xx}^*)}{|r_x|^2 + |r_y|^2} \approx 2\Im\left(\frac{\Delta r}{r}\right). \quad (3.93)$$

To conclude, the Mueller matrix obtained by using ellipsometry measurement provides complete information about $\Delta r/r$ ratio which is measured by the RAS measurement.

3.3.2 Comparison of Mueller matrix ellipsometry with standard spectroscopic ellipsometry

The spectroscopic ellipsometry allows to determine two independent quantities, the ellipsometric angles Ψ and Δ , defined by Eq. (3.77) as a function of the photon energy. One of the mostly used configuration is based on the phase modulation similarly as used in the RAS measurement. Considering the polarizer-modulator-analyzer configuration with the respective azimuthal angles α_P , α_M , and α_A with respect to the plane of incidence, the measured intensity is [83]:

$$I_{SE}(t) = I_{0,SE} [1 + I_S \sin(\Gamma(t)) + I_C \cos(\Gamma(t))], \quad (3.94)$$

where

$$I_S = \sin[2(\alpha_A - \alpha_M)] \sin 2\alpha_P \sin 2\Psi \sin \Delta, \quad (3.95)$$

$$I_C = \sin[2(\alpha_A - \alpha_M)] [\sin 2\alpha_M (\cos 2\Psi - \cos 2\alpha_P) + \sin 2\alpha_P \cos 2\alpha_M \sin 2\Psi \cos \Delta]. \quad (3.96)$$

One can clearly see that for unambiguous determination of the ellipsometric angles Δ and Ψ , at least two measurements must be done [83]. For example two measurements with configurations: i) $\alpha_M = 0^\circ$, $\alpha_A = 45^\circ$, and $\alpha_P = 45^\circ$ for which $I_S = \sin 2\Psi \sin \Delta$, $I_C = \sin 2\Psi \cos \Delta$, and ii) $\alpha_M = 45^\circ$, $\alpha_A = 90^\circ$, and $\alpha_P = 45^\circ$ for which $I_S = \sin 2\Psi \sin \Delta$, $I_C = I_{C'} = \cos 2\Psi$.

The Mueller matrix polarimetry enables to measure and determine both ellipsometric angles in one fast measurement. For non-depolarizing isotropic sample, the normalized Mueller matrix has the following form:

$$\mathbf{M}_{\text{norm}} = \begin{bmatrix} 1 & -\cos 2\Psi & 0 & 0 \\ -\cos 2\Psi & 1 & 0 & 0 \\ 0 & 0 & \sin 2\Psi \cos \Delta & \sin 2\Psi \sin \Delta \\ 0 & 0 & -\sin 2\Psi \sin \Delta & \sin 2\Psi \cos \Delta \end{bmatrix} = \begin{bmatrix} 1 & -I_{C'} & 0 & 0 \\ -I_{C'} & 1 & 0 & 0 \\ 0 & 0 & I_C & I_S \\ 0 & 0 & -I_S & I_C \end{bmatrix}, \quad (3.97)$$

where I_C , $I_{C'}$, and I_S are the intensities measured by the standard spectroscopic ellipsometry.

3.4 Conclusion of the chapter

This chapter has been dedicated to the theory of the electromagnetic response of multi-layer anisotropic structures. After derivation of the wave equation for generally anisotropic medium, we introduced the transfer and the scattering matrix formalism as effective methods for calculation of the reflection coefficients, ellipsometric angles and the Mueller matrix components. In the end of this chapter we have compared the Mueller matrix ellipsometry used in this thesis with other widely used measurement techniques such as the reflectance anisotropy spectroscopy and standard spectroscopic ellipsometry and we have pointed out the benefits of this method.

Chapter 4

Experimental study of surface and interfacial optical anisotropy

This chapter is devoted to the experimental study of local linear anisotropies in InGaAs/GaAsP semiconductor VECSEL laser structure using the Mueller matrix ellipsometry. Such anisotropic effects originate from i) the reduction from D_{2d} to C_{2v} symmetry group at the III-V semiconductor interface and ii) locally present strain at surface and in the quantum wells. We present ellipsometry results in the spectral range from 0.73 to 6.4 eV in order to disentangle surface and quantum wells (QWs) contributions to the linear optical birefringence of the structures. The measurement of the full 4×4 Mueller matrix for multiple angles of incidence and in-plane azimuthal angles in combination with proper parametrization of optical functions has been used for extraction of optical permittivity tensors of surface strained layers and QWs. Such spectral dependence of optical tensor elements are crucial for modeling of future spin-laser eigenmodes, resonance conditions, and also for understanding of sources of structure anisotropies. The Mueller matrix measurement and analysis have been published in the journal *Applied Physics Letters* [43].

4.0.1 Experimental setup

The Mueller matrix ellipsometer Woollam RC2 was used for the measurement of the complete Mueller matrix of the VECSEL laser structure. Figure 4.1 shows the PCSCA configuration [80] of the experimental measurement (polarizer-compensator-sample-compensator-analyzer) used to collect all 16 elements of the Mueller matrix [84]. The ellipsometer uses a combination of halogen bulb and deuterium lamp as a light source in the UV-NIR spectral region from 0.74 eV to 6.42 eV (193-1700 nm). The beam is collimated by an achromatic lens and then passes through a fixed MgF_2 Rochon polarizer, and finally through an achromatic rotating (10 Hz) prism compensator. The detector consists of two spectrometers: i) Si CCD detector for UV-VIS spectral range and ii) InGaAs photodiode array for NIR region. The sample is mounted to the stage, which enables in-plane rotation of the sample around z axis. In reflection, the angle of incidence $\theta^{(0)}$ can be varied from 19° - 85° .

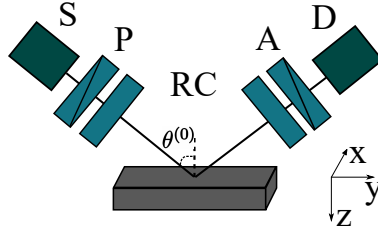


Figure 4.1: Configuration of the experimental measurement: light source (S), polarizer (P), dual-rotating compensator (RC), analyzer (A), and detector (D).

4.1 Sample description

Figure 4.2 shows schematically the VECSEL laser structure consisting an epitaxial high-reflectivity (99.9%) bottom AlAs/GaAs Bragg mirror (26 pairs) of the nominal thicknesses $t_{AlAs} = 85.37$ nm and $t_{GaAs} = 71.8$ nm. The $13\lambda/2$ thick active region is constituted of 6 strain-balanced 8 nm InGaAs/GaAsP QWs with emitting laser frequency at $\lambda \simeq 1 \mu\text{m}$. Each pairs of QWs is separated by a GaAs spacer which size decreases when getting closer to the surface. A 30 nm thick insulating AlAs layer in-between the surface and the active medium used as a carrier confinement layer in optical pumping experiments. The nominal thickness of GaAs capping layer is 10 nm.

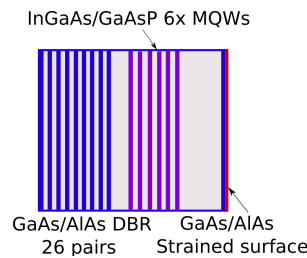


Figure 4.2: Schematic description of studied VECSEL structure.

4.2 Optical function of semiconductor layers

The critical step involved in fitting Mueller matrix ellipsometric data to a given structural model is the proper parametrization of the dispersion of the unknown energy-dependent complex optical functions $\varepsilon_r(E) = \varepsilon_1 - i\varepsilon_2$. We have used a Kramers-Kronig (KK) consistent Tauc-Lorentz (TL) model function, which was developed by Jellison [85] using the Tauc joint density of states and the Lorentz oscillator. This approach is combined by subset of more general Herzinger-Johs parametrized function shape with KK properties [86] to model the shape of an M_0 critical point seen in direct gap semiconductors such as GaAs around the gap energy E_g .

Tauc-Lorentz model

In the approximation of parabolic bands, Tauc's dielectric function describing inter-band mechanism above the band edge is in the form:

$$\varepsilon_2^T(E) = \begin{cases} A_T \left(\frac{E-E_g}{E} \right)^2 & E \geq E_g \\ 0 & E \leq E_g \end{cases}, \quad (4.1)$$

where A_T is the Tauc coefficient, E is the photon energy, and E_g is the energy of the optical bandgap.

On the other hand, the derivation of the Lorentz oscillator is based on the classical theory of interaction between light and matter and is used to describe frequency dependent polarization due to bound charge, which supposed to be analogy to a spring-mass system. Bounded electrons react to an electromagnetic field by vibrating like damped harmonic oscillator leading to the imaginary part of the relative permittivity [85]:

$$\varepsilon_2^L = \frac{A_L \Gamma E_0 E}{(E^2 - E_0^2)^2 + \Gamma^2 E^2}, \quad (4.2)$$

where Γ is the broadening parameter and E_0 is the energy of central peak with amplitude A_L .

Multiplying of Eq. (4.1) and Eq. (4.2) leads to the Tauc-Lorentz dispersion formula:

$$\varepsilon_2(E) = \begin{cases} \frac{1}{E} \frac{A E_0 \Gamma (E-E_g)^2}{(E^2 - E_0^2)^2 + \Gamma^2 E^2} & E \geq E_g \\ 0 & E \leq E_g \end{cases}, \quad (4.3)$$

with the overall amplitude $A = A_T A_L$. The real part of the dielectric function is derived using Kramers-Kronig integration [85]:

$$\varepsilon_1(E) = \varepsilon_{1\infty} + \frac{2}{\pi} \mathcal{P}_C \int_{E_g}^{\infty} \frac{E' \varepsilon_2(E')}{E'^2 - E^2} dE', \quad (4.4)$$

where \mathcal{P}_C is the Cauchy principal value and $\varepsilon_{1\infty}$ is the constant term originating from high-energy absorptions.

Herzinger-Johs model

The model developed by Johs [86], which combines functional shape with Kramers-Kronig consistent properties, is convenient when reproducing complicated dielectric function shape without the need of additional oscillators between critical points. Analytically, a single oscillator is formed by four-order Gaussian-broadened polynomials, which are grouped into four polynomial ensembles connected end-to-end and centred on critical point E_C . Each spline connects smoothly with the adjacent spline, forming a single, continuous function as depicted in Fig 4.3. Generally, each critical point is described by 9 parameters. E_C is the CP energy with amplitude A_C , while E_L and E_U are the end points. Energies E_{LM} and E_{UM} with respective amplitudes A_{LM} and A_{UM} describes two control points for establishing the assymetry of the lineshape. The center (E_C), the bounding energies (E_L and E_U) and

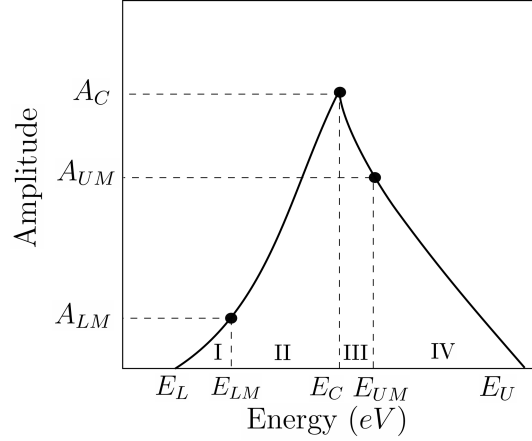


Figure 4.3: Schematic of a single unbroadened CP structure in the Herzinger-Johs model.

center amplitude (A_C) are specified absolutely. The position of the control points, which correspond to the joining points of four polynomials, are defined relative to these absolutes.

The general expression of the dielectric function is then given as a summation of the Herzinger-Johs dielectric function $\varepsilon^{HJ}(\omega) = \varepsilon_1^{HJ} - i\varepsilon_2^{HJ}$ and P_o poles representing contribution from outside region of studied spectra:

$$\varepsilon(\omega) = 1 + \varepsilon^{HJ}(\omega) + \sum_{j=1}^{P_o} \frac{A_j}{(\hbar\omega)^2 - E_j^2}. \quad (4.5)$$

The imaginary part of the Herzinger-Johs dielectric function ε_2^{HJ} is described using m energy-bounded polynomials given by [86]:

$$\varepsilon_2^{HJ}(\omega) = \sum_{j=1}^m \int_{E_{min}}^{E_{max}} W_j(E) \Phi(\hbar\omega, E, \sigma_j) dE, \quad (4.6)$$

where $\Phi(\hbar\omega, E, \sigma_j)$ is the Gaussian broadening factor and $W_j(E)$ is the fourth-order ($N = 4$) polynomial function:

$$W_j(E) = \sum_{k=0}^N P_{j,k} E^k u(E - a_j) u(b_j - E), \quad (4.7)$$

with coefficients $P_{j,k}$ and unit step functions $u(x)$. The corresponding real part of the dielectric function ε_1^{HJ} is obtained by Kramers-Kronig transformation. In this work, we use HJ function to model the shape of M_0 CP of the zinc-blende semiconductor such as GaAs as depicted in Fig. 4.4.

4.3 Fitting procedure and figure of merit

The important part of data analysis process is quantifying how well the quantity calculated by the optical model "agrees" with the raw measured data. Therefore we must define some

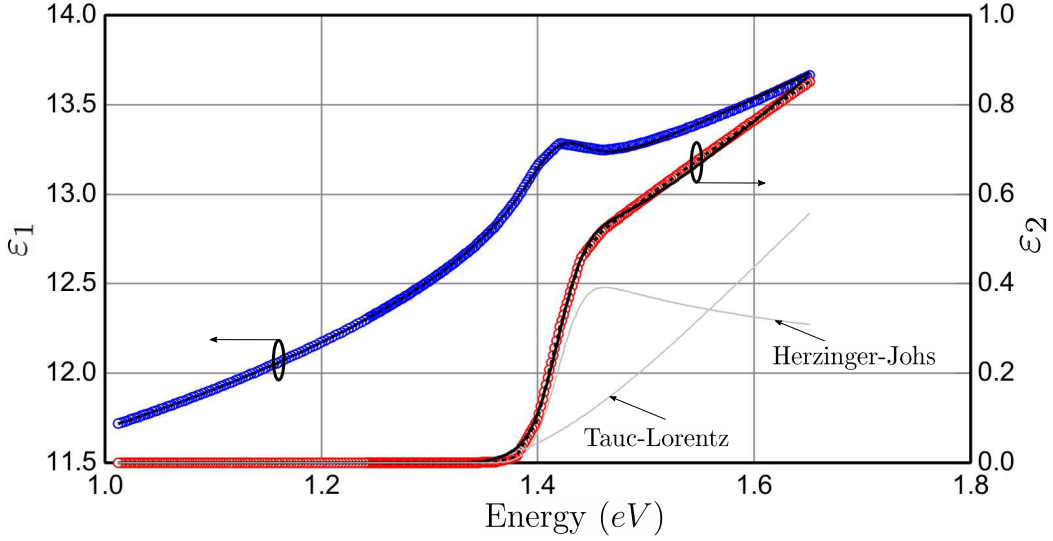


Figure 4.4: Model of the bandgap and M_0 critical point of GaAs by using Herzinger-Johs and Tauc-Lorentz oscillators. Blue and red circles correspond to tabulated data, black solid curves describe model and grey solid curves correspond to model oscillators.

quantity, which represents the quality of the match between the measured and calculated data. The mostly used quantity, χ^2 function, is defined by:

$$\chi^2 = \frac{1}{N_\lambda N_o - N_p} \sum_{w=1}^{N_{wvl}} \sum_{(ij) \neq (1,1)} \left(\frac{m_{ij,w}^{th} - m_{ij,w}^{exp}}{\sigma_{ij,\lambda}} \right)^2, \quad (4.8)$$

where N_λ is the number of spectral points, N_o is the number of observables ($N_o = 15$ for normalized Mueller matrix measurement), N_p is the number of variable (fit parameters), and $\sigma_{ij,\lambda}$ is the wavelength-dependent standard deviation. The subscripts *th* and *exp* refer to the calculated and the measured data, respectively.

To obtain the best fit between the experimentally measured and model generated data (to achieve the lowest χ^2), parameters of the optical model called fit parameters such as thicknesses or optical functions must be adjusted. This procedure is done by using a standard non-linear iterative optimization analysis called the Levenberg-Marquardt least square algorithm [87]. When evaluating the fit results, one must follow the following rules: i) The model must be physical. This for example means that optical function determined from a model fit must be Kramers-Kronig consistent. ii) The model should be unique. The general rule is to choose the simplest model that adequately fits the data set. It is always possible to reduce χ^2 function by adding more fit parameters, but unless the χ^2 is significantly reduced, the additional complexity is not justified. On the other hand, for complex structure, one can try alternate models to partially verify model uniqueness.

4.4 Results

Figure 4.5 displays the measured spectra of the Mueller matrix components M_{21} , M_{34} , and M_{44} in the full range from 0.73 to 6.4 eV compared with data fit with using the tabulated optical constants of GaAs, AlAs, InGaAs, GaAsP [88, 89], and including also GaAs oxide layer on the top [90]. These components of the Mueller matrix together with $M_{12} = M_{21}$, $M_{43} = -M_{34}$, and $M_{33} = M_{44}$ are the most important to reveal the linear birefringence and dichroism. Considering the general form of the reflection coefficient r_{ss} and r_{pp} (without s - and p - polarized light conversion), one can recall Eq. (3.88) and show that $M_{21} \propto |r_{ss}|^2 - |r_{pp}|^2$ and $M_{44} \propto \Re\{r_{ss}r_{pp}^*\}$ leading to the sensitivity on linear dichroism, while $M_{34} \propto \Im\{r_{ss}r_{pp}^*\}$ is the most sensitive element to the linear birefringence [91]. From the spectral measurement, one can clearly observe two different regions: i) the transparent region from 0.73 to 1.7 eV (730-1700 nm) with visible interference effect, where the light is propagating in the whole structure due to the negligible absorption in semiconductor multilayers with presence of photonic Bragg bandgap in the the range from 1.2 to 1.3 eV (953-1033 nm), and ii) the range from 1.7 to 6.4 eV (193-730 nm) without any interferences, where the AlAs/GaAs surface layers absorb incident light.

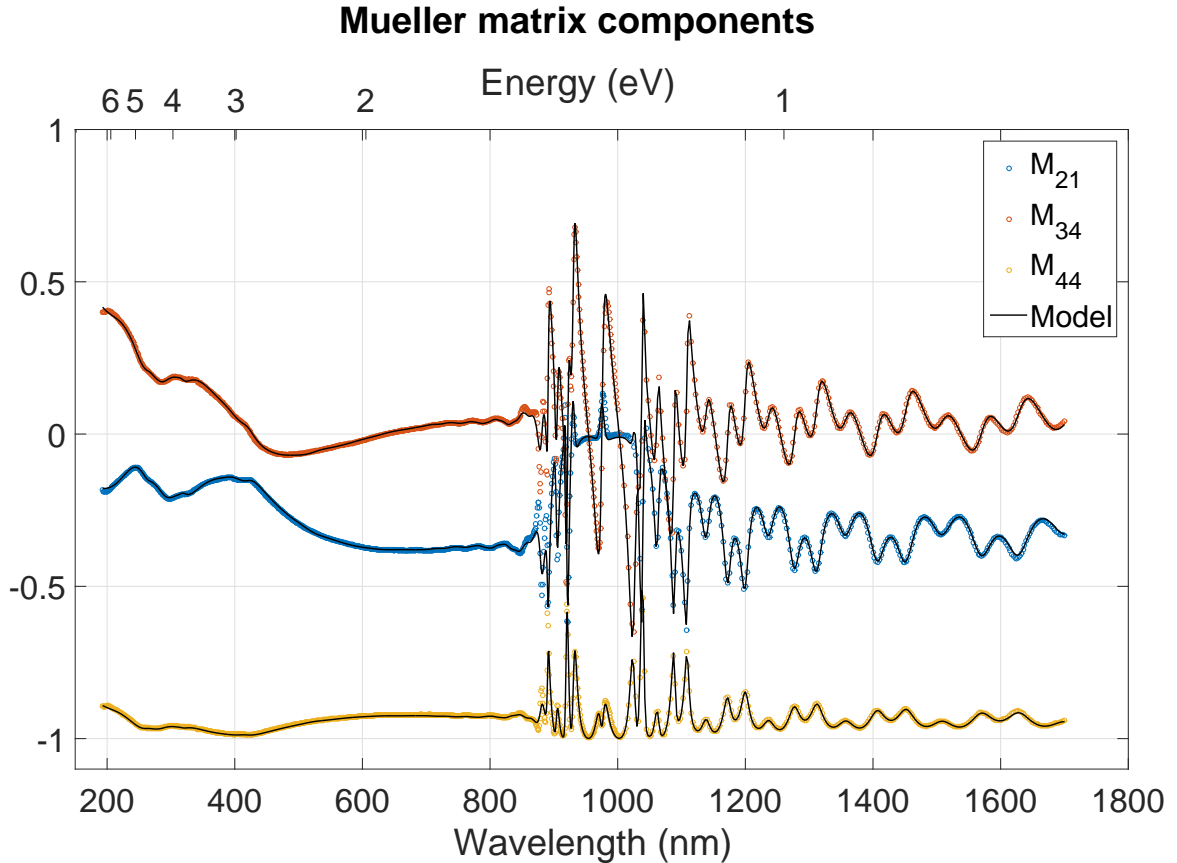


Figure 4.5: Measured and modeled Mueller matrix element spectra. The angle of incidence of $\theta^{(0)} = 40^\circ$ has been chosen.

The analysis procedure of VECSEL structure consists of the following steps: I) The

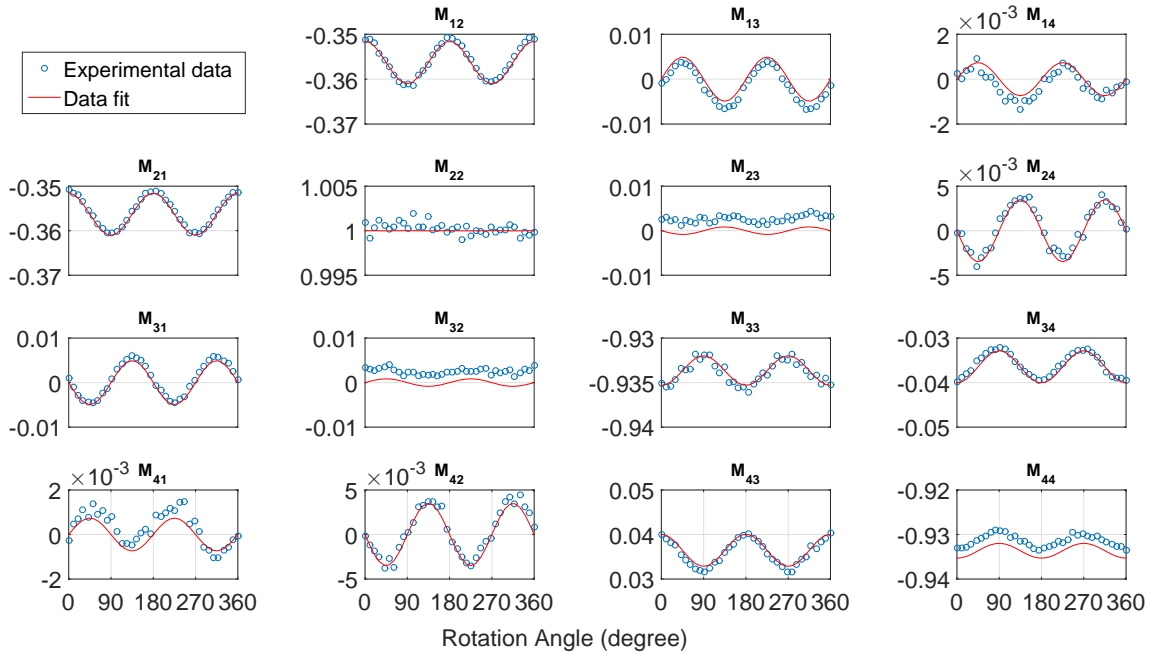


Figure 4.6: The measured Mueller matrix elements as a function of the in-plane azimuth rotation angle ranging from 0 to 360 degrees for $E = 2.2$ eV and for the angle of incidence $\theta^{(0)} = 40^\circ$.

Material	Obtained thickness	Nominal thickness
GaAs	9.3 ± 0.2 nm	10 nm
AlAs	29.8 ± 0.3 nm	30 nm
InGaAs QW	7.8 ± 0.4 nm	8 nm

Table 4.1: The obtained and the nominal thicknesses of GaAs/AlAs layers on the top of surface and InGaAs quantum wells.

analysis of the full measured spectra from 0.73 to 6.4 eV, variable angle of incidence, and using tabulated optical constants in order to extract the precise thicknesses of all semiconductor layers. Example of thickness fit is shown in Fig. 4.5. Comparison of the obtained thicknesses and nominal values of selected layers are shown in Table 4.1. II) Including data with 360 degree range of azimuthal sample-rotation angles, replacing the tabulated constant by the proper parametric functions of the AlAs/GaAs top layers, and fitting the parameters of the oscillators in the absorption region $E > 1.8$ eV, where the sensitivity to surface is maximal due to an absorption of the top layers. III) Fitting of all azimuthal angles in whole spectral range including mainly transparent region $E < 1.8$ eV, replacing the tabulated constant by parametric function of the InGaAs quantum wells and fitting of a few parameters of the optical oscillators while the surface optical constants obtained in the previous step are fixed.

As mentioned above, the critical step involved in fitting Mueller matrix ellipsometric data to a given structural model is the proper parametrization of the energy-dependent

complex material optical functions described by the complex permittivity $\varepsilon(E) = \varepsilon_1 - i\varepsilon_2$. We have used the Kramers-Kronig (KK) consistent Tauc-Lorentz (TL) model function [85] described in Section 4.2. This approach is combined by subset of more general Herzinger-Johs parametrized function shape with KK properties [86] to model the shape of an M_0 critical point seen in direct gap semiconductors such as GaAs around the gap energy E_g . In combination with 4×4 matrix formalism describing the light propagation in anisotropic stratified media, the Levenberg-Marquardt least square algorithm [87] is used to obtain Mueller matrix data fit.

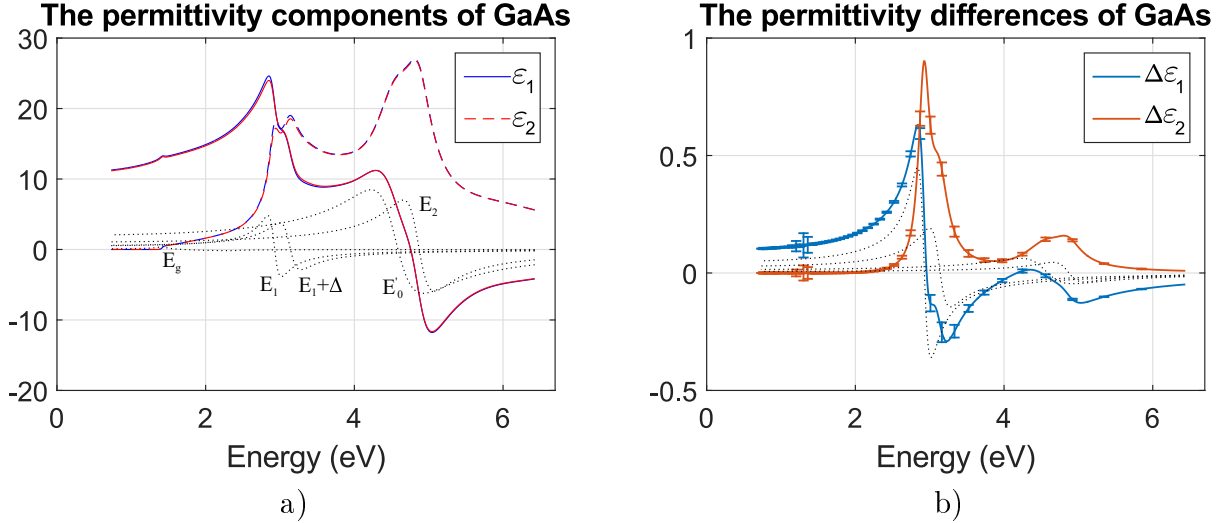


Figure 4.7: a) The ordinary (blue curve) and extraordinary (red curve) optical constants and b) the permittivity differences of real $\Delta\varepsilon_1$ and imaginary $\Delta\varepsilon_2$ parts of GaAs

Figure 4.6 displays the measured Mueller matrix elements as a function of the in-plane azimuth rotation angle ranging from 0 to 360 degree for the photon energy of $E = 2.2$ eV. Clear evidence of the broken in-plane symmetry in the surface GaAs/AlAs layers is observed due to the 180 degree (π) symmetry of the measured MM dependence on the rotation angle. Note that effects of the sample tilt and misalignment would exhibit 360 degree (2π) symmetry. Presented model is based on the optical functions parametrization of the GaAs/AlAs top layers by TL model with the amplitudes as a fitting parameters in the absorbing range from 1.7 to 6.4 eV, while all other structure parameters (thicknesses, optical constants of quantum wells and barriers, etc.) are fixed. The resulting optical constants are shown in Fig 4.7a) and Fig. 4.8a). For the lasing energy of $E = 1.24$ eV, the difference between ordinary and extraordinary optical constants $\Delta\varepsilon_1 = \varepsilon_{1,o} - \varepsilon_{1,eo}$ gives $\Delta\varepsilon_1 = 0.115 \pm 0.005$ for 10 nm thick GaAs and $\Delta\varepsilon_1 = 0.021 \pm 0.005$ for 30 nm thick AlAs, giving the average value about $\Delta\varepsilon_1 = 0.04$ for a 40 nm thick layer composed of GaAs/AlAs at surface in agreement with our recent analysis using active lasing configuration described in Chapter 6 and published in our paper [37].

We will now discuss the connection between particular interband transitions of zinc-blende-type semiconductor depicted in Fig. 4.10 with the obtained permittivity functions. The fundamental absorption edge of zinc-blende-type GaAs and AlAs corresponds to direct transitions from the highest valence band to the lowest conduction band at the Γ point

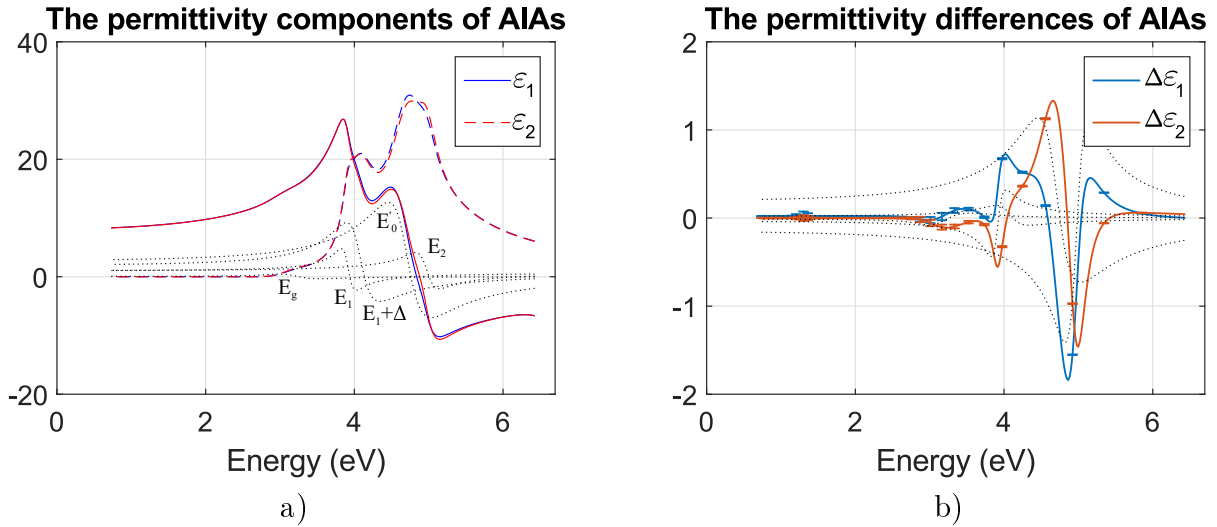


Figure 4.8: a) The ordinary (blue curve) and extraordinary (red curve) optical constants and b) the permittivity differences of real $\Delta\varepsilon_1$ and imaginary $\Delta\varepsilon_2$ parts of AlAs.

	$\varepsilon_1 = \varepsilon_{1,o}$	$\varepsilon_2 = \varepsilon_{2,o}$	$\Delta\varepsilon_1 = \varepsilon_{1,o} - \varepsilon_{1,eo}$	$\Delta\varepsilon_2 = \varepsilon_{2,o} - \varepsilon_{2,eo}$
GaAs	12.30	0	0.115	0
AlAs	8.69	0	0.021	0
InGaAs	13.10	0.76	0.047	0.026

Table 4.2: Table of the optical constants and their extracted difference.

(Brillouin zone center) with the energy $E_g = 1.42$ eV for GaAs and $E_g = 2.89$ eV for AlAs as depicted in Figs. 4.7a) and 4.8a). Above the E_g critical point, we observe E_1 and $E_1 + \Delta$ (spin-orbit split) transitions, which occur at the L point of the Brillouin zone or along the Λ lines [92]. The E_0' describes the transitions between the valence bands and higher conduction band at the Γ point. The imaginary part of the permittivity ε_2 reaches a strong absolute maximum known as the E_2 peak, which contains contribution over a large region close to the edges in the [100] (X point) and [110] (K point) directions of the Brillouin zone [93].

In Figure 4.7b and Fig. 4.8b one can observe each of the resonant peak absorption corresponding to each critical points of the Brillouin zone. The main contribution of the anisotropy of the GaAs originates from the E_1 and $E_1 + \Delta$ transitions giving up a positive anisotropy between ordinary and extraordinary axis $\Delta\varepsilon_1 > 0$ and $\Delta\varepsilon_2 > 0$ up to the energy of $E = 2.9$ eV and opposite $\Delta\varepsilon_1 < 0$ for higher energy. The contribution of AlAs to the surface anisotropy for energy below band gap E_g is much smaller due to the compensation between E_1 and E_0' oscillators. On the other hand, in higher energy range, these oscillators play crucial role and contribute most to the surface strain.

In the following step, the extracted optical constants of the surface layers have been considered fixed, while the optical constants of the InGaAs QW are parametrized and

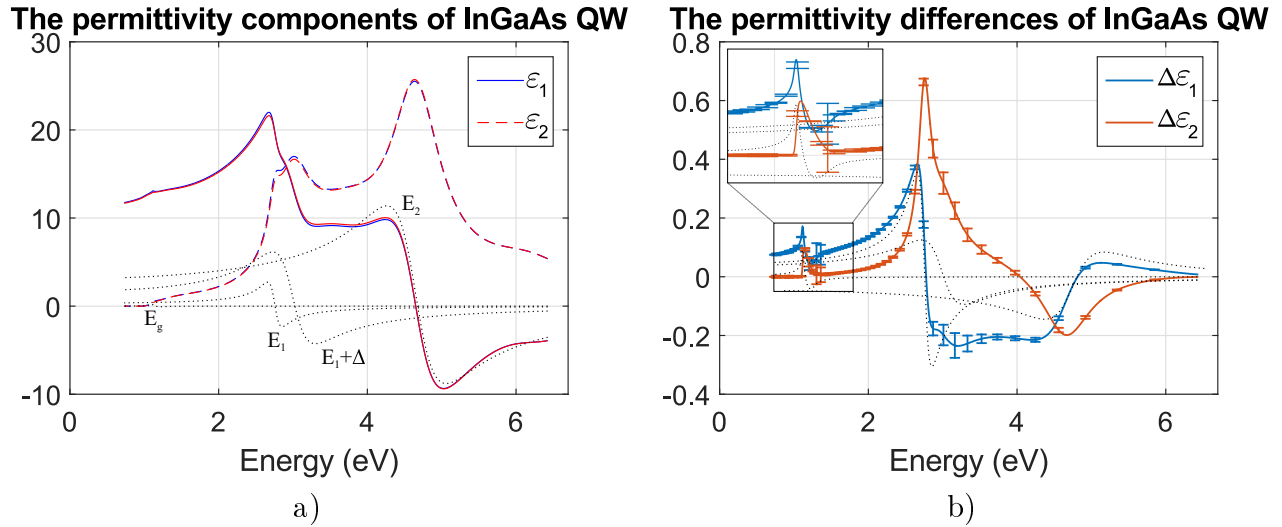


Figure 4.9: a) The ordinary (blue curve) and extraordinary (red curve) optical constants and b) the permittivity differences of real $\Delta\epsilon_1$ and imaginary $\Delta\epsilon_2$ parts of InGaAs quantum wells.

fitted to the experimental data in the full range from 0.73 to 6.4 eV. The optical constants in all QWs are considered the identical (coupled) in order to reduce a number of fitting parameters. Results are depicted in Fig. 4.9a and Fig. 4.9b. We note that the highest accuracy is obtained for region below 1.8 eV, while the features above are determined only quantitatively. The contribution of the QW to the overall birefringence admits two main parts: i) one positive originating from the region of E_1 and E'_1 spin-orbit split transitions and ii) the negative from the region of higher energies around E_2 transition. For the lasing energy $E = 1.24$ eV, this gives $\Delta\epsilon_1 = 0.047 \pm 0.005$ for 8 nm thick InGaAs QW (48 nm total). We first note a positive sign of $\Delta\epsilon_1 > 0$, identical to the surface birefringence, which should be correlated to a corresponding negative sign in the regime of laser operation due to the population inversion. The larger value of $\Delta\epsilon_1$, although not yet understood, may originate in the non-saturated inversion of population in laser operation, where the average birefringence has been extracted close to $6 \cdot 10^{-3}$ [37]. The order of magnitude of $\Delta\epsilon_1$ is in agreement with the RAS measurement of the similar single quantum well system InGaAs/GaAs in Ref. 38.

4.5 Conclusion of the chapter

The Mueller matrix ellipsometry presented in this chapter is useful method for study of local anisotropies in multilayer semiconductor structures such as VECSEL lasers. In a future work, this experimental method can be combined with S-matrix recursive formalism for lasing structures developed in our previous work in Ref. 37 and in the next chapter of this thesis to find the best material conditions (semiconductor host, active zone, quantum well alloying) to eliminate or compensate overall birefringence in compact spin-VCSEL devices, which will lead to circularly-polarized laser emission.

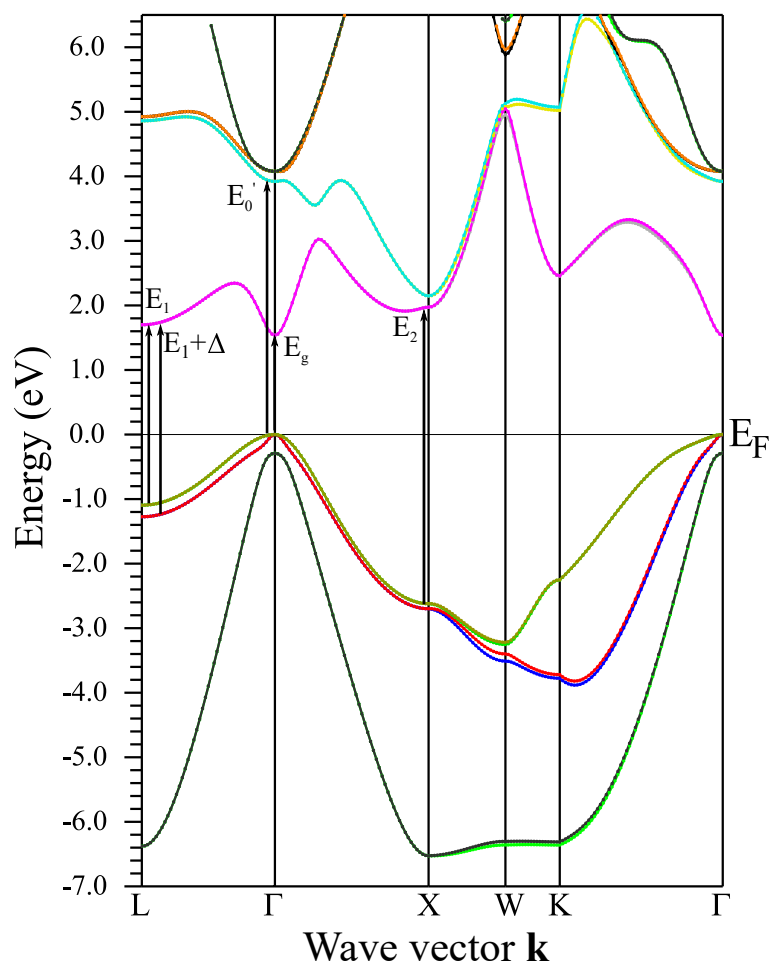


Figure 4.10: Electronic energy-band structure of GaAs calculated by density function theory (DFT) using Wien2K. The main interband transitions are indicated by the vertical arrows.

Chapter 5

Theoretical and numerical techniques for the analysis of eigenmodes of spin-VECSELs with local linear birefringence and gain dichroism

This chapter is dedicated to the detailed analysis of a general method for the modeling of semiconductor lasers such as spin-polarized vertical-cavity surface-emitting lasers and vertical-external-cavity surface-emitting lasers. In the beginning of this chapter we will describe the recent 2×2 Jones matrix analysis of spin-VECSEL developed by Alouini and described in Ref. 44. This simple model can describe evolution of the polarization eigen states in the cavity as a function of the effective linear birefringence and circular gain dichroism induced by the spin of injected carriers. However, it is not suitable for description of more complex laser structures with multiple quantum wells (dipolar active sources) inside a cavity and with local anisotropies.

On the other hand, the modeling method developed in this work contains description of the amplification processes in multiple quantum wells, multiple reflections, propagation between them, and involving anisotropies that may reveal *i*) a local linear birefringence due to the strain field at the surface or *ii*) a birefringence in quantum wells (QWs) due to phase amplitude coupling originating from the reduction of the biaxial D_{2d} to the C_{2v} symmetry group at the III-V ternary semiconductor interfaces. From a numerical point of view, a novel scattering S-matrix recursive method is implemented using a gain or amplification tensor derived analytically from the Maxwell-Bloch equations. It enables to model the properties of the emission (threshold, polarization, mode splitting) from the laser with multiple quantum well (MQW) active zones by searching for the resonant eigenmodes of the cavity. The results presented in this chapter have been published in the journal *Physical Review A* [37] and in Ref. 45.

5.1 Recent mathematical description: The 2×2 Jones matrix analysis of spin-VECSEL

Let us consider a cavity depicted in Fig. 5.1 which exhibits a residual phase anisotropy (linear birefringence) and circular gain dichroism induced by a spin-population unbalance. The Jones matrix of the is given by Eq. (3.40). We recall:

$$\mathbf{J}_{\text{LB}} = \begin{bmatrix} e^{-i\frac{2\pi}{\lambda}n_x l} & 0 \\ 0 & e^{-i\frac{2\pi}{\lambda}n_y l} \end{bmatrix} = e^{-i\frac{2\pi}{\lambda}\bar{n}l} \begin{bmatrix} e^{-iLB/2} & 0 \\ 0 & e^{iLB/2} \end{bmatrix}, \quad (5.1)$$

where $LB = \frac{2\pi}{\lambda_0}(n_x - n_y)l$ describes the linear birefringence and $\bar{n} = (n_x + n_y)/2$ is the average real part of optical index, while the matrix prefactor represents an overall phase delay. It is usual to rewrite the Jones vector in the term of the phase anisotropy γ so that:

$$\mathbf{J}_{\text{LB}} = e^{-i\frac{2\pi}{\lambda}\bar{n}l} \begin{bmatrix} e^{-i\gamma} & 0 \\ 0 & e^{i\gamma} \end{bmatrix}, \quad (5.2)$$

where

$$\gamma = \frac{\pi}{\lambda_0} (n_x - n_y) l. \quad (5.3)$$

In the case of spin-polarized pumping, a cavity exhibits the gain circular dichroism $\Delta G = G_+ - G_-$, where G_+ and G_- are the gains for right and left circularly-polarized light, respectively. If we introduce the average gain as $\bar{G} = (G_+ + G_-)/2$, then the associated Jones matrix is:

$$\mathbf{J}_{\text{GD}} = \begin{bmatrix} \bar{G} & -\frac{i}{2}\Delta G \\ +\frac{i}{2}\Delta G & \bar{G} \end{bmatrix}. \quad (5.4)$$

The complete cavity is closed with the input and the output mirrors. The Jones vectors of the mirror with reflectivity R_m can be written in the form

$$\mathbf{J}_{\text{M}} = \sqrt{R_m} \begin{bmatrix} 1 & 0 \\ 0 & 1 \end{bmatrix}. \quad (5.5)$$

Considering the input mirror with perfect reflectivity and output mirror with reflectivity R_m , we can express the complete Jones vector of the cavity as:

$$\mathbf{J}_{\text{C}} = e^{i\phi} \mathbf{J}_{\text{LB}} \mathbf{J}_{\text{GD}} \mathbf{J}_{\text{LB}} \mathbf{J}_{\text{M}}, \quad (5.6)$$

where the $e^{i\phi}$ term describes the accumulated phase during propagation in the laser cavity. By including the particular Jones matrices from Eqs.(5.2)-(5.5) we express the final Jones matrix of the cavity as:

$$\mathbf{J}_{\text{C}} = \bar{G} \sqrt{R_M} e^{-2ik_0 l_{\text{eff}}} \begin{bmatrix} e^{-2i\gamma} & -\frac{i}{2}\Delta\tilde{G} \\ +\frac{i}{2}\Delta\tilde{G} & e^{2i\gamma} \end{bmatrix}, \quad (5.7)$$

where $l_{\text{eff}} = n_a l_a + \bar{n}l + l_{\text{ext}}$ represents the effective length of the cavity while n_a , l_a , and l_{ext} are optical index of the active medium, its length, and the length of the air cavity, respectively. The normalized circular gain dichroism is $\Delta\tilde{G} = \Delta G/\bar{G}$. The resonance

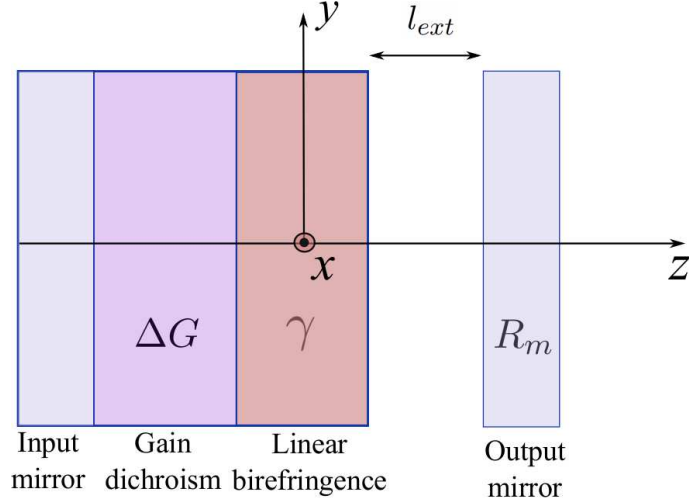


Figure 5.1: Schematic representation of the simplified laser cavity.

condition of the electric field \mathbf{E} is then solved using the eigenvalue equation with eigenvalue λ_E :

$$\mathbf{J}_C \mathbf{E} = \lambda_E \mathbf{E}. \quad (5.8)$$

The eigenvalue equation is then:

$$(\lambda_E - \cos 2\gamma)^2 = \frac{1}{4} \Delta \tilde{G}^2 - \sin^2 2\gamma. \quad (5.9)$$

We will now discuss general non-trivial case for which both linear birefringence and circular gain dichroism induced by spin unbalance are present: γ and $\Delta \tilde{G} \neq 0$.

Case i) the linear birefringence is dominant: $\frac{1}{4} \Delta \tilde{G}^2 < \sin^2 2\gamma$

Solving of Eq. (5.9) leads to two *complex solutions*:

$$\lambda_E^\pm = \cos 2\gamma \pm i \sqrt{\sin^2 2\gamma - \frac{1}{4} \Delta \tilde{G}^2}. \quad (5.10)$$

It is straightforward that the imaginary part causes frequency degeneracy breaking so that each polarization state has its own lasing frequency. The detuning between these eigenpolarization is then:

$$\Delta f = \frac{c}{2\pi l_{eff}} \arctan \frac{\sqrt{\sin^2 2\gamma - \frac{1}{4} \Delta \tilde{G}^2}}{\cos 2\gamma}. \quad (5.11)$$

By developing (5.8) we express the ratio between the electric-field components as:

$$\frac{E_y}{E_x} = 2 \frac{\sin 2\gamma}{\Delta \tilde{G}} \left(1 \pm \sqrt{1 - \frac{\Delta \tilde{G}^2}{4 \sin^2 2\gamma}} \right). \quad (5.12)$$

Because of the requirement $\frac{1}{4} \Delta \tilde{G}^2 < \sin^2 2\gamma$, the ratio E_y/E_x is real so that the laser admits two linearly polarized eigenmodes whose orientation depends on the ratio between the circular dichroism term $\frac{1}{4} \Delta \tilde{G}^2$ and the linear birefringence term $\sin^2 2\gamma$.

Case ii) the linear birefringence and the gain dichroism have equal magnitudes: $\frac{1}{4}\Delta\tilde{G}^2 = \sin^2 2\gamma$

This case represents a transition point between the linearly and circularly (elliptically) polarized eigenmodes. The solution of Eq. (5.9) gives *real value*:

$$\lambda_E^\pm = \cos 2\gamma \quad (5.13)$$

so that the electric field components verify:

$$\frac{E_y}{E_x} = -1, \quad (5.14)$$

which describes linearly polarized mode oriented at -45° from the birefringence axis x . Both eigenstates are therefore degenerate in frequency and with the same polarization state so that they are indistinguishable.

Case iii) the circular gain dichroism is dominant: $\frac{1}{4}\Delta\tilde{G}^2 > \sin^2 2\gamma$

In comparison to the previous case i), now the solving Eq. (5.9) leads to two *real solutions*:

$$\lambda_E^\pm = \cos 2\gamma \pm \sqrt{\frac{1}{4}\Delta\tilde{G}^2 - \sin^2 2\gamma}. \quad (5.15)$$

It is now straightforward that pure real solutions of λ_E^\pm lead to no change in phases of two eigenmodes and therefore both eigenmodes oscillate with same frequency. The output polarization is then given by their superposition. The ratio between the electric field components are given by:

$$\frac{E_y}{E_x} = \frac{e^{-2i\gamma} - \lambda_E^\pm}{\frac{1}{2}i\tilde{G}} \quad (5.16)$$

with the module:

$$\left| \frac{E_y}{E_x} \right| = 1 \quad (5.17)$$

and the phase:

$$\arg\left(\frac{E_y}{E_x}\right) = \mp \arctan\left(\frac{\tilde{G}^2}{4\sin^2 2\gamma} - 1\right), \quad (5.18)$$

which straightly describe elliptically polarized eigenmodes. The resolution of the eigenvalue equation (5.9) gives access to the respective gain for each eigen state:

$$G_\pm = \frac{1}{\sqrt{R_M}\lambda_E^\pm} = \left[\sqrt{R_M}\cos 2\gamma \pm \sqrt{\frac{1}{4}\Delta\tilde{G}^2 - \sin^2 2\gamma} \right]^{-1}. \quad (5.19)$$

The conclusion of the presented analysis is shown in Fig. 5.2. If the linear birefringence is dominant ($\frac{1}{4}\Delta\tilde{G}^2 < \sin^2 2\gamma$) both eigen polarizations are linearly polarized oscillating with different frequencies while their respective orientation depends on the ratio between the terms describing the circular gain dichroism $\Delta\tilde{G}$ and the linear birefringence $\sin 2\gamma$. When the circular gain dichroism increases, the linearly polarized and fully degenerated eigenmodes lose their orthogonality and converge in one direction oriented at -45° from the birefringence axis for $\frac{1}{4}\Delta\tilde{G}^2 = \sin^2 2\gamma$. With increasing circular gain dichroism, the linear polarizations change to an elliptical one with the long axis oriented at 45° from the birefringence axis up to the state which can be considered as circularly polarized. Second orthogonal elliptical (circular) polarization with lower gain appears for higher $\frac{1}{4}\Delta\tilde{G}^2$.

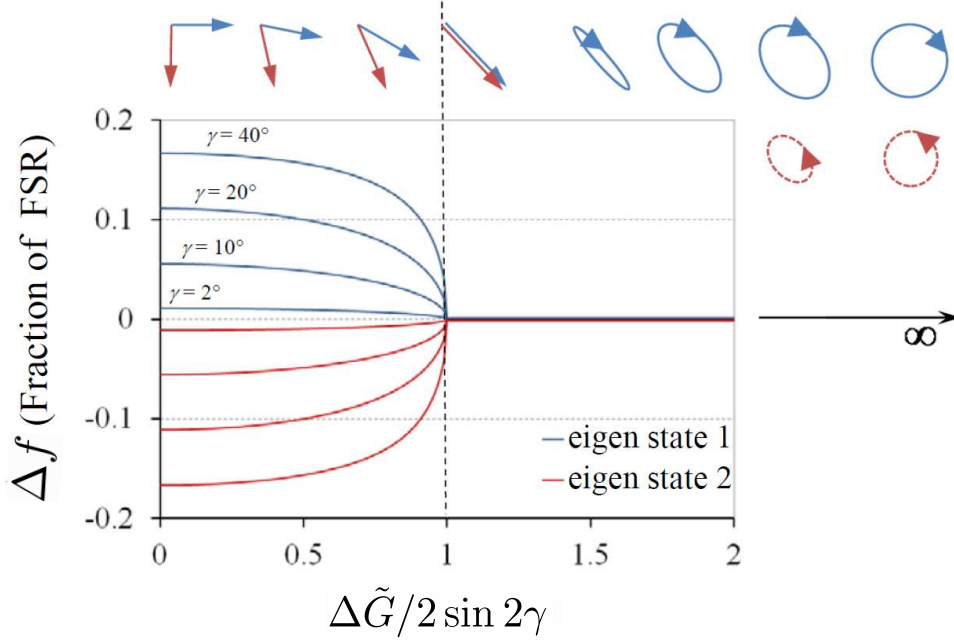


Figure 5.2: Evolution of the polarization state and the frequency detuning [33, 44].

5.2 Physics of spin-pumped gain medium with linear birefringence

5.2.1 Maxwell-Bloch Equations

The carrier-photon dynamics of spin-lasers can be modeled, from the basis of the Maxwell-Bloch equations [94–103], using a spin-dependent rate equation analysis. The rate equations can provide a direct relation between material properties and device parameters [104–106]. Recalling the general form for the electric field \mathbf{E} and the polarization $\tilde{\mathbf{P}}$:

$$\mathbf{E} = \frac{1}{2}\mathbf{E}_0 e^{i(\omega t - \mathbf{k}\mathbf{r})} + \text{c.c.} = \frac{1}{2}A\boldsymbol{\eta}_0 e^{i(\omega t - \mathbf{k}\mathbf{r})} + \text{c.c.} \quad (5.20)$$

$$\tilde{\mathbf{P}} = \frac{1}{2}\tilde{\mathbf{P}}_0 e^{i(\omega t - \mathbf{k}\mathbf{r})} + \text{c.c.} = \frac{1}{2}\tilde{\mathcal{P}}\boldsymbol{\eta}_0 e^{i(\omega t - \mathbf{k}\mathbf{r})} + \text{c.c.}, \quad (5.21)$$

we will now discuss three rate equations governing the behaviour of a single-frequency laser for i) the polarization of the active medium, ii) the inversion of a spin-polarized population, and iii) the electric field in a cavity.

Interaction Hamiltonian

The Maxwell-Bloch equations derive from the evolution of the density matrix [94–97, 102, 103] under the action of the electrical dipolar Hamiltonian:

$$\hat{\mathbf{H}}_d = -\hat{\mathbf{d}} \cdot \mathbf{E} = -\sum_i \hat{\mathbf{d}}_i E_i, \quad (5.22)$$

where $\hat{\mathbf{d}}$ is the electric dipole operator with the off-diagonal matrix elements between two levels $|1\rangle$ and $|2\rangle$, with $\mu \equiv d_{21,i} = \langle 1|\hat{\mathbf{d}}_i|2\rangle$ as the dipolar coupling coefficient.

All atomic eigenstates have well defined parity (even or odd) due to the central character of the atomic potential, so that $\mathbf{d}_{11} = \mathbf{d}_{22} = 0$ and $\mathbf{d}_{12} = \mathbf{d}_{21}^*$. Then in order to have interaction, we have to consider states $|1\rangle$ and $|2\rangle$ with opposite parity. Hence the interaction Hamiltonian is in the form:

$$\hat{\mathbf{H}}_d = \begin{bmatrix} 0 & V \\ V^* & 0 \end{bmatrix}, \quad (5.23)$$

where we introduce the notation:

$$V = -\mathbf{d}_{21} \cdot \mathbf{E}, \quad (5.24)$$

which with the form for electric field (5.20) becomes [107]:

$$V = -\hbar\alpha e^{i(\omega t - \mathbf{k}\mathbf{r})} - \hbar\beta e^{-i(\omega t - \mathbf{k}\mathbf{r})}, \quad (5.25)$$

where

$$\alpha = \frac{\mathbf{d}_{21} \cdot \boldsymbol{\eta}_0}{2\hbar} A, \quad (5.26)$$

$$\beta = \frac{\mathbf{d}_{21} \cdot \boldsymbol{\eta}_0^*}{2\hbar} A^*. \quad (5.27)$$

Note that $2\alpha = \omega_R$ is usually called the Rabi angular frequency of the light. Then the total Hamiltonian for two-level atom with the transition angular frequency ω_{21} reads:

$$\hat{\mathbf{H}} = \begin{bmatrix} \frac{1}{2}\hbar\omega_{21} & V \\ V^* & -\frac{1}{2}\hbar\omega_{21} \end{bmatrix}. \quad (5.28)$$

Density matrix and population matrix

In the case of two-level atom with states $|1\rangle$ and $|2\rangle$, the density matrix $\tilde{\rho}$ is used for describing the probability that an atom occupies a particular state. For example the matrix element $\tilde{\rho}_{22}$ denotes the probability, that the atom occupies state $|2\rangle$. The evolution of $\tilde{\rho}_{22}$ is governed by the Von Neumann equation [108]:

$$i\hbar \frac{\partial \tilde{\rho}}{\partial t} = [\hat{\mathbf{H}}, \tilde{\rho}]. \quad (5.29)$$

An introducing of the new variables:

$$\sigma_{21} = \sigma_{12}^* = \tilde{\rho}_{21} e^{-i(\omega t - \mathbf{k}\mathbf{r})}, \quad (5.30)$$

allows us to write the Bloch equations for two-level system as:

$$\frac{\partial \tilde{\rho}_{22}}{\partial t} = -\frac{\partial \tilde{\rho}_{11}}{\partial t} = -i \left(\alpha e^{2i(\omega t - \mathbf{k}\mathbf{r})} + \beta \right) \sigma_{21} + \text{c.c.}, \quad (5.31)$$

$$\frac{\partial}{\partial t} \sigma_{21} = -i\delta' \sigma_{21} - i \left(\alpha^* e^{-2i(\omega t - \mathbf{k}\mathbf{r})} + \beta^* \right) (\tilde{\rho}_{22} - \tilde{\rho}_{11}) + \text{c.c.}, \quad (5.32)$$

where $\delta' = \omega - \omega_{21}$ is the detuning factor. From the above equations we can clearly see, that if the interaction with the electric field is present ($\alpha \neq 0$ and $\beta \neq 0$), two terms appear: one slowly varying proportional to β and one high frequency varying term proportional

to α . Clearly, atoms cannot well respond to the latter and one can neglect them in the so-called Rotating Wave Approximation [109]. This approximation widely used in quantum optics allows us to write the equations (5.31) and (5.32) in the following form [107]:

$$\frac{\partial}{\partial t} (\tilde{\rho}_{22} - \tilde{\rho}_{11}) = -2i(\beta\sigma_{21} - \beta^*\sigma_{21}^*) \quad (5.33)$$

$$\frac{\partial}{\partial t} \sigma_{21} = -i\delta'\sigma_{21} - i\beta^*(\tilde{\rho}_{22} - \tilde{\rho}_{11}). \quad (5.34)$$

In real lasers, we consider not only two-level atom interacting with the electric field, but many atoms bounded together and creating lattices in bulk or quantum well semiconductors. In the case of a large number of atoms, the density matrix $\tilde{\rho}$ is replaced by the population matrix ρ , which is the averaged density matrix over a large number of atoms \mathcal{N} with the density matrices $\tilde{\rho}_i$:

$$\rho = \frac{1}{\mathcal{N}} \sum_i \tilde{\rho}_i. \quad (5.35)$$

Moreover, since a laser is a dissipative system, including relaxations is important as depicted in Fig. 5.3. We introduce them phenomenologically into the optical Bloch equations (5.33) and (5.34). Since the levels $|1\rangle$ and $|2\rangle$ exhibit finite lifetimes τ_1 and τ_2 , we can define the relaxation rates for the populations ρ_{11} and ρ_{22} :

$$\gamma_1 = \frac{1}{\tau_1} \quad (5.36)$$

$$\gamma_2 = \frac{1}{\tau_2}. \quad (5.37)$$

Now we consider that some of the population decaying from level $|2\rangle$ feeds level $|1\rangle$, for example, by spontaneous emission with the rate γ_{21} . By introducing Γ as a off-diagonal damping factor for the coherences ρ_{12} , and the pumping rates Λ_1 and Λ_2 of levels $|1\rangle$ and $|2\rangle$, allows us to rewrite the optical Bloch equations (5.33) and (5.34) as follows:

$$\frac{\partial}{\partial t} \rho_{22} = \Lambda_2 - \gamma_2 \rho_{22} - i(\beta\sigma_{21} - \beta^*\sigma_{21}^*), \quad (5.38)$$

$$\frac{\partial}{\partial t} \rho_{11} = \Lambda_1 - \gamma_1 \rho_{11} + \gamma_{21} \rho_{22} + i(\alpha^*\sigma_{21} - \alpha\sigma_{21}^*), \quad (5.39)$$

$$\frac{\partial}{\partial t} \sigma_{21} = -(\Gamma + i\delta')\sigma_{21} - i\beta^*(\rho_{22} - \rho_{11}). \quad (5.40)$$

Equation of evolution for the polarization

Under the action of the light field each atom develops an electric dipole. As the number of atoms contained in a small volume (small as compared with the light wavelength) is always large, one can assume that at each spatial position \mathbf{r} there exists a polarization given by the quantum-mechanical expectation value of the electric dipole moment operator $\hat{\mathbf{d}}$. When using the density (population) matrix formalism, this expectation value is computed as the trace:

$$\tilde{\mathbf{P}} = \mathcal{N} \text{Tr}(\rho \hat{\mathbf{d}}) \quad (5.41)$$

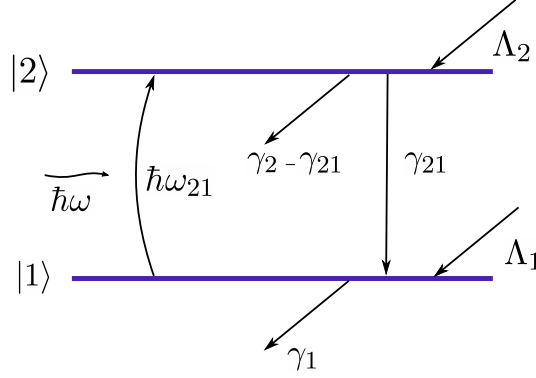


Figure 5.3: The relaxation and pumping of a two-level system.

where \mathcal{N} and ρ are, respectively, the atomic density and the density matrix, so that:

$$\tilde{\mathbf{P}} = \mathcal{N} (\rho_{21} \mathbf{d}_{12} + \text{c.c.}). \quad (5.42)$$

By considering:

$$\sigma_{21} = \sigma_{12}^* = \rho_{21} e^{-i(\omega t - \mathbf{k} \cdot \mathbf{r})}, \quad (5.43)$$

Eq. (5.42) yields:

$$\tilde{\mathbf{P}} = \mathcal{N} \left[\sigma_{21} \mathbf{d}_{12} e^{-i(\omega t - \mathbf{k} \cdot \mathbf{r})} + \text{c.c.} \right]. \quad (5.44)$$

By comparing with the general form of the polarization (5.21) and inserting into Eq. (5.40) using Eq. (5.27) we obtain the rate equation for the evolution of polarization:

$$\frac{\partial \tilde{\mathbf{P}}_0}{\partial t} = -(\Gamma + i\delta') \tilde{\mathbf{P}}_0 - i \frac{\mu^2}{\hbar} \mathbf{E}_0 \Delta n. \quad (5.45)$$

Equation of evolution for the population inversion

We now simplify the calculation for four-level system for which the lower level |1> decays very fast ($\tau_1 \ll \tau_2$) and is not pumped ($\Lambda_1 = 0$) so that it is considered empty ($\rho_{11} = 0$). Then the population inversion is given by:

$$\Delta N = \mathcal{N} \rho_{22}. \quad (5.46)$$

The rate equation for the population inversion (5.38) takes the form:

$$\frac{\partial \Delta N}{\partial t} = -\gamma (\Delta N - \Delta N_0) - \frac{i}{\hbar} \left(\mathbf{E}_0^* \tilde{\mathbf{P}}_0 - \mathbf{E}_0 \tilde{\mathbf{P}}_0^* \right), \quad (5.47)$$

where $\gamma = 1/\tau_2 = 1/\tau$ is the damping rate of the carrier densities and $\Delta N_0 = \mathcal{N} \Lambda_2 \tau$ is the population pumping term. The Maxwell-Bloch dynamical equations link the electric field \mathbf{E} and the medium polarization \mathbf{P} in a vectorial form vs. the carrier density, which may be different, using electrical or optical elliptically polarized pumps. In the slowly-varying-amplitude approximation limit, rate equations for dynamics of the electric field \mathbf{E} and carrier density can be determined once one admits that the medium polarization \mathbf{P} adiabatically follows the electric field dynamics.

Equation of field evolution in laser cavity

The evolution of the electric field in the cavity is governed by wave equation (3.7) which can be rewritten with help of the additional relation for the polarization \mathbf{P} (3.2a):

$$\frac{\partial^2 \mathbf{E}}{\partial z^2} - \varepsilon_0 \mu_0 \frac{\partial^2 \mathbf{E}}{\partial t^2} - \tilde{\sigma} \mu_0 \frac{\partial \mathbf{E}}{\partial t} = \mu_0 \frac{\partial^2 \mathbf{P}}{\partial t^2}, \quad (5.48)$$

where losses in the cavity (absorption and output losses) are introduced by a generalized conductivity $\tilde{\sigma}$, which depends on the photon lifetime in the cavity τ_{ph} so that: $\tilde{\sigma} \sim 1/\tau_{ph}$. The polarization term in Eq. (5.48) contains two terms: the material polarization:

$$\mathbf{P}_{mat} = \varepsilon_0 \chi \mathbf{E} = \varepsilon_0 (\varepsilon_r - 1) \mathbf{E} \quad (5.49)$$

and the nonlinear polarization of the active atoms $\tilde{\mathbf{P}}$ which acts as a source term, so that

$$\mathbf{P} = \mathbf{P}_{mat} + \tilde{\mathbf{P}}. \quad (5.50)$$

Taking into account that

$$c = \frac{1}{\sqrt{\mu_0 \varepsilon_0}}, \quad (5.51)$$

we finally write:

$$\frac{\partial^2 \mathbf{E}}{\partial z^2} - \frac{\varepsilon_r}{c^2} \frac{\partial^2 \mathbf{E}}{\partial t^2} - \tilde{\sigma} \mu_0 \frac{\partial \mathbf{E}}{\partial t} = \mu_0 \frac{\partial^2 \tilde{\mathbf{P}}}{\partial t^2}. \quad (5.52)$$

By inserting Eqs. (5.20) and (5.21) into the field wave equation (5.52) one can expect long equation for the amplitude and polarization amplitudes \mathbf{E}_0 and $\tilde{\mathbf{P}}_0$. Therefore we use the slowly-varying-amplitude approximation which is valid when losses and gain in the cavity are weak enough. Then we can neglect all the second time and space derivatives, for example if:

$$\left| \frac{\partial^2 \mathbf{E}_0}{\partial z^2} \right| \ll k \left| \frac{\partial \mathbf{E}_0}{\partial z} \right|. \quad (5.53)$$

Moreover we can also neglect the term $\partial \mathbf{E}_0 / \partial z$ with respect to $\partial \mathbf{E}_0 / \partial t$. With these assumptions we reach the wave equation in the form:

$$\frac{\partial \mathbf{E}_0}{\partial t} = -\frac{1}{2\tau_{ph}} \mathbf{E}_0 + i \frac{\omega}{2\varepsilon_r} \tilde{\mathbf{P}}_0, \quad (5.54)$$

where we introduced the lifetime of the photons in the cavity τ_{ph} :

$$\tau_{ph} = \frac{\varepsilon_r}{\tilde{\sigma}} \quad (5.55)$$

5.2.2 Generalized Maxwell-Bloch Equations

Generally, a common dynamic spin-flip model (SFM) originally developed by San Miguel and coworkers two decades ago is used to describe the left- or right-handed polarization switching and bistability [36, 97, 110]. The polarization properties of the light generated by VCSELs depend on the quantum numbers of the angular momentum in the electronic

states between which the optical transitions take place generally under local strain fields. One possibility of considering anisotropy is a generalization of the equations with the considerable simplification of neglecting the longitudinal variations within the system, by taking the z average (where z is the direction of propagation of light) of the optical constant in order to develop the equivalent of the mean-field model in the Jones vector analysis [111]. Such an approach, although first satisfactory, prevents a full multiscale description treating the exact effect of the local strain field on the optical birefringence and of the gain. The full scattering matrix method [40, 45] developed in this work fulfills all these requirements.

One admits here that the transverse relaxation time of the optical polarizability is very short corresponding to the main class-A and class-B lasers [112]. In the semiconductor host constituting the optical cavity, the vectors \mathbf{E} and \mathbf{P} are linked by the dielectric constant (or the optical refractive index) that we will consider locally via a layer-by-layer approach.

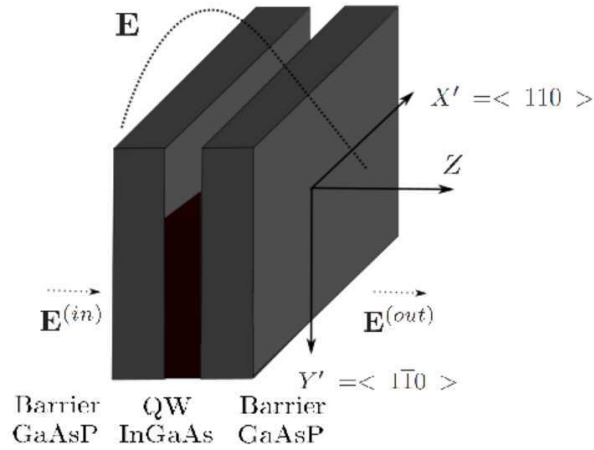


Figure 5.4: Scheme of the quantum well and barrier system with crystal axes.

However, crystallographic and electro-optical anisotropies can cause the directions of the vectors \mathbf{E} and \mathbf{P} to slightly differ in the active regions where carrier recombination takes place. Even if the resulting optical gain only represents a small fraction of the electromagnetic wave intensity in the cavity, the non collinearity property between \mathbf{E} and \mathbf{P} in QWs is of major importance to understand polarizations and mode coupling. The non-collinearity between \mathbf{E} and \mathbf{P} also impacts on the competition between circular pumps and native linear gain anisotropy as observed in recent experiments [32, 34].

We propose to tackle the problem of non-collinearity between \mathbf{E} and \mathbf{P} by deriving a certain optical amplification matrix describing the electric field entering the active zone and its emission from the laser. We refer now to the sketch and notations given in Fig. 5.4. Let us define the electromagnetic field of the two-mode laser $\mathbf{E}_{(1,2)}$ as a sum of two orthogonal

coupled lasing eigenmodes $A_{(1,2)}\boldsymbol{\eta}_{(1,2)}$ in the following way:

$$\begin{aligned}\mathbf{E} &= \sum_{i=1,2} \frac{1}{2} \mathbf{E}_{(i)} \exp [i (\omega_{(i)} t - \mathbf{k}_{(i)} \mathbf{r})] + c. c. \\ &= \sum_{i=1,2} \frac{1}{2} A_{(i)} \boldsymbol{\eta}_{(i)} \exp [i (\omega_{(i)} t - \mathbf{k}_{(i)} \mathbf{r})] + c. c.,\end{aligned}\quad (5.56)$$

$$\tilde{\mathbf{P}} = \sum_{i=1,2} \frac{1}{2} \tilde{\mathbf{P}}_{(i)} \exp [i (\omega_{(i)} t - \mathbf{k}_{(i)} \mathbf{r})] + c. c.,\quad (5.57)$$

where the $\boldsymbol{\eta}_{(1,2)}$ are the two polarized eigenmodes we are searching for, either (1) or (2); $A_{(i)}(\mathbf{r}, t)$ and $\tilde{\mathbf{P}}_{(i)}$ are, respectively, the slowly time-varying envelope amplitudes and the polarizations of the modes i ($i = 1, 2$). $\mathbf{k}_{(i)}$ are the wave vectors. In the following, we consider wave propagation parallel to the z direction. The derivation is made by projecting the ongoing electric-field vector of the propagating wave crossing the active region over the two optically active circular reference basis [(+) for spin \uparrow and (-) for spin \downarrow defined along the direction normal to the layers].

For that purpose, the dipolar amplitude responsible for the optical gain and corresponding to each of the two spin populations has to be derived. We define \mathbf{A}_{\pm}^d as those amplitudes in the Jones vector form like largely emphasized in the remaining part of this chapter. For a two-level model, N_{\pm} denotes the respective spin-up (+) and spin-down (-) carrier densities in QWs above transparency (tr) where $N_{\pm} = N_{\uparrow\downarrow} - N_{\text{tr}}$ follows the respective pumping rates $N_{0\pm}$. Recent theoretical investigations based on the steady-state ab initio laser theory (SALT) allow an extension from a two-level model to more complex media involving multilevel transitions [102, 103]. The dynamical behavior of each of physical constituents, \mathbf{E} and $\tilde{\mathbf{P}}$ follows [94, 96]:

$$\begin{aligned}\frac{\partial \tilde{\mathbf{P}}_{(1,2)}}{\partial t} &= -(\Gamma + i\delta') \tilde{\mathbf{P}}_{(1,2)} \\ &\quad - i \frac{\mu^2}{\hbar} \left[\left(\mathbf{E}_{(1,2)} \mathbf{A}_{+}^{d*} \right) \mathbf{A}_{+}^d N_{+} + \left(\mathbf{E}_{(1,2)} \mathbf{A}_{-}^{d*} \right) \mathbf{A}_{-}^d N_{-} \right]\end{aligned}\quad (5.58)$$

$$\begin{aligned}\frac{\partial N_{\pm}}{\partial t} &= -\gamma (N_{\pm} - N_{0\pm}) \mp \gamma_s (N_{+} - N_{-}) \\ &\quad - \frac{i}{\hbar} \sum_{i=1,2} \left\{ \left(\mathbf{E}_{(i)}^* \mathbf{A}_{\pm}^d \right) \left(\tilde{\mathbf{P}}_{(i)} \mathbf{A}_{\pm}^{d*} \right) + c.c. \right\}\end{aligned}\quad (5.59)$$

where Γ is the off-diagonal damping factor for the off-diagonal density-matrix elements (media polarization), γ is the damping rate of the carrier densities, γ_s is the corresponding spin-flip rate, and δ' is the spectral detuning.

Those two equations together with the wave equation (5.52) represent a generalization of the Maxwell-Bloch equations and of the spin-flip model we were searching for to the case of anisotropic active regions. The difference with previous approaches is now that we have projected the \mathbf{E} - and $\tilde{\mathbf{P}}$ - fields within a non-orthogonal basis imposed by the anisotropy. Indeed, from the first equation, one can be convinced that the *vectorial* optical gain is not necessarily collinear to the incoming \mathbf{E} -field for $\langle \boldsymbol{\eta}_{(2)} | \mathbf{A}_{+}^d \rangle \neq 0$ and $\langle \boldsymbol{\eta}_{(1)} | \mathbf{A}_{-}^d \rangle \neq 0$. This feature is reinforced if birefringences within the semiconductor host

are considered. Our modeling method satisfies the whole Eqs. (5.52), (5.58), and (5.59) in each of the layers, active regions, barriers, and semiconductor host by using selected optical constants. In particular, the last equation describes the propagation of the electromagnetic field throughout the structure including a certain optical loss. This can be modeled by a certain imaginary part into the dielectric constant tensor (or the optical refractive index) describing a possible temporal damping parameter $\kappa \sim 1/\tau_{layer}$ where τ_{layer} denotes the photon lifetime. In the following, we will derive the optical gain properties by considering QWs free of losses.

5.2.3 Derivation of the optical gain including linear anisotropies

Derivation of the optical gain tensor

We are now searching for a general numerical scheme for the determination of the resonant eigenmodes in cavities. The assumption of the slowly variable amplitude approximation (see Eq. 5.54) and of a fast polarization damping leads, in a steady-state operation regime, to:

$$\frac{\partial \mathbf{E}_{(i)}}{\partial t} = -\frac{1}{2}\kappa \mathbf{E}_{(i)} + i\frac{\omega}{2\varepsilon_r} \tilde{\mathbf{P}}_{(i)} \quad (5.60)$$

and

$$\langle \tilde{\mathbf{P}}_{(i)} \rangle = -i\frac{\mu^2}{\hbar} \frac{[(\mathbf{E}_{(i)} \mathbf{A}_+^{d*}) \mathbf{A}_+^d N_+ + (\mathbf{E}_{(i)} \mathbf{A}_-^{d*}) \mathbf{A}_-^d N_-]}{\Gamma + i\delta'} \quad (5.61)$$

which yields:

$$\begin{aligned} \frac{\partial \mathbf{E}_{(i)}}{\partial t} &= -\frac{1}{2}\kappa \mathbf{E}_{(i)} \\ &+ \frac{\omega\mu^2}{2\varepsilon_r (\Gamma + i\delta') \hbar} \left[(\mathbf{E}_{(i)} \mathbf{A}_+^{d*}) \mathbf{A}_+^d N_+ + (\mathbf{E}_{(i)} \mathbf{A}_-^{d*}) \mathbf{A}_-^d N_- \right]. \end{aligned} \quad (5.62)$$

This is the general dynamical equation controlling the change of the E -field envelope amplitude in a non-zero polarization-medium. It gives then the expression for the field amplification in an active layer (QWs) once the spin-polarized carriers densities N_{\pm} are given. A slow dynamics of N_{\pm} may come into play when one considers two or several coupled modes [99, 101] or oscillation emission, which we will not consider henceforth. Although we will discuss the impact of anisotropies on a possible two transverse mode coupling, we only address here the issue of a single mode laser and we are searching for such modes.

If one neglects any optical losses in QWs ($\kappa_{QW} \rightarrow 0$), one can implement a fast integration in time of Eq. (5.60) leading thus to the required jump in $\delta \mathbf{E}_{(i)}$ according to $\delta \mathbf{E}_{(i)} = \frac{nW\omega\mu^2}{2c\varepsilon(\Gamma+i\delta')\hbar} [(\mathbf{E}_{(i)} \cdot \mathbf{A}_+^{d*}) \mathbf{A}_+^d N_+ + (\mathbf{E}_{(i)} \cdot \mathbf{A}_-^{d*}) \mathbf{A}_-^d N_-]$ with the result:

$$\delta \mathbf{E}_{(i),m} = g_0 \mathcal{T}_{mn} \mathbf{E}_{(i),n}, \quad (5.63)$$

where

$$\mathcal{T}_{mn} = \left[\mathbf{A}_{+,m}^{d*} \mathbf{A}_{+,n}^d \frac{N_+}{N_+ + N_-} + \mathbf{A}_{-,m}^{d*} \mathbf{A}_{-,n}^d \frac{N_-}{N_+ + N_-} \right]. \quad (5.64)$$

W represents the QW thickness and \mathcal{T} is the *optical gain tensor* for the electromagnetic field $\mathbf{E}_{(i)}$ with the corresponding gain amplitude

$$g_0 = \frac{n\omega\mu^2NW}{2c\varepsilon_r(\Gamma + i\delta')\hbar}, \quad (5.65)$$

where $N = N_+ + N_-$ is the total pumped carrier density above transparency and the NW product represents the carrier sheet density in QWs. We recall that the subscripts (m, n) are the space coordinates. As largely discussed in the following, this particular form of the gain we derived should include the phase-amplitude coupling known as the Henry factor $\alpha = \frac{\text{Real}(\partial\chi/\partial N)}{\text{Imag}(\partial\chi/\partial N)}$ [where $\chi(\omega)$ is the matter susceptibility]. In that sense, g_0 may be written as $g_0 = g_{00}(1 - i\alpha)$. The relevance of the so-called Henry's factor also manifests on the steady-state SALT equations described in Refs. 102 and 103. Equation (5.63) simply reflects an amplification of the m -component ($m = x, y$) of the \mathbf{E} -field for an incoming n -component ($n = x, y$) when N_{\pm} are controlled parameters at present (Fig. 5.4). Off-diagonal components of the \mathcal{T} -matrix reflect the non-collinearity between dipole sources and eigenmodes, originating from the linear gain dichroism.

The particular expression for the prefactor gain g_0 is the one given at low out-of-equilibrium carrier densities. It can be shown that the dependence of the gain on pumped carrier density has generally logarithmic dependence so that Eq. (5.65) can be generalized into:

$$g_0 = \frac{n\omega\mu^2}{2c\varepsilon_r(\Gamma + i\delta')\hbar} (N_{th}W) \ln \left(\frac{N + N_s}{N_{th} + N_s} \right) \quad (5.66)$$

giving $g_0(N) \simeq \frac{\partial g_0}{\partial N} N$ with the differential gain $\frac{\partial g_0}{\partial N}$. Here N_{th} is the carrier density at threshold (or slightly smaller) and N_s is an adjustable parameter controlling the correct gain variation with N [46].

In order to derive the expression of the 2×2 optical gain tensor \mathcal{T}_{ij} , one needs to consider the two different E -field polarization sources, \mathbf{A}_{\pm}^d within the active regions (QWs). These are described in a Jones vector form and correspond separately to the two different spin eigenchannels, $+$ and $-$. Due to the quantization axis of the wave functions, along the z direction normal to the layers, the correct basis is the \pm spin basis along z even in the case of a linearly polarized pump (the particular case with $N_+ = N_-$). \mathbf{A}_{\pm}^d are complex conjugate from each other $\mathbf{A}_{-}^d = (\mathbf{A}_{+}^d)^*$ but not necessarily orthogonal.

Effect of the linear gain anisotropy.

We consider now the possible case of a linear gain anisotropy in the active layers (QWs), imposed by a certain bonding anisotropy at the interface with the barriers due to the symmetry reduction from D_{2d} to C_{2v} . The overall gain anisotropies may be characterized by *i*) a Δ parameter departing from 1 (we will see in the following that $\Delta = 1$ will correspond to a perfect isotropy) and *ii*) by the effective spin-polarization in QWs of carriers pumped:

$$\mathcal{P}_s = \frac{N_+ - N_-}{N_+ + N_-}. \quad (5.67)$$

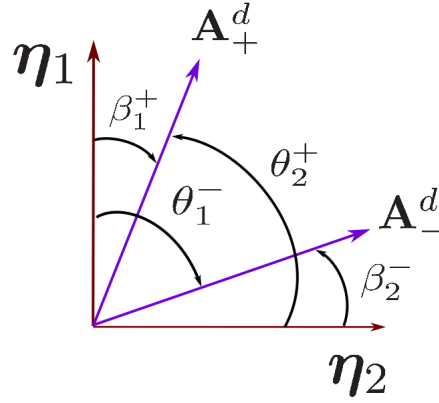


Figure 5.5: Scheme of the two orthogonal laser eigenmodes $\eta_{1,2}$ and dipolar source vectors \mathbf{A}_{\pm}^d . The dipolar source vectors are not necessarily orthogonal to each other depending on the dichroism into play. The non-orthogonality between \mathbf{A}_{\pm}^d is at the origin of a strong mode-coupling as discussed in the text.

The evaluation of \mathbf{A}_{\pm}^d is performed in the $X' = [110], Y' = [1\bar{1}0]$ crystallographic basis for the two reference optical directions. Associated to a possible anisotropy of the optical oscillator strengths along X' and Y' , two different dipolar transition matrix elements can be ascribed for an \mathbf{E} emission along X' or Y' according to $\Pi_{x'} = \langle S|p_{x'}|X' \rangle = -i\hbar \langle S|\nabla_{x'}|X' \rangle$ and $\Pi_{y'} = \langle S|p_{y'}|Y' \rangle = -i\hbar \langle S|\nabla_{y'}|Y' \rangle$ with $\Pi_{y'} = \Delta\Pi_{x'}$; $\Delta \neq 1$ then refers to a certain linear gain anisotropy. \hat{p}_m is the impulsation operator and Π_m is the corresponding optical transition element. We refer, e. g., to the notation of Zutic *et al.* [113] for the description of the respective S (conduction band) and X, Y , and Z , (P-type orbitals of the valence band) quantum states describing the optical interband dipolar terms. We rewrite the basis states $|X\rangle$ and $|Y\rangle$ into the basis $|X'\rangle$ and $|Y'\rangle$ rotated by $\pi/4$ using the following transformation:

$$|X\rangle = \frac{1}{\sqrt{2}} (|X'\rangle + |Y'\rangle) \quad (5.68)$$

$$|Y\rangle = \frac{1}{\sqrt{2}} (|X'\rangle - |Y'\rangle). \quad (5.69)$$

Then the heavy hole valence band for the respective spin \uparrow (+) and spin \downarrow (-) channels can be described as:

$$|X\rangle \mp i|Y\rangle = \frac{1}{\sqrt{2}} [1 \mp i] |X'\rangle + \frac{1}{\sqrt{2}} [1 \pm i] |Y'\rangle. \quad (5.70)$$

By application of the oscillator strength anisotropy Δ on the second term we have:

$$|X\rangle \mp i|Y\rangle = \frac{1}{2} [(1 + \Delta) \mp i(1 - \Delta)] |X\rangle + \frac{1}{2} [(1 - \Delta) \mp i(1 + \Delta)] |Y\rangle. \quad (5.71)$$

Then the normalized dipolar source vector for the spin \uparrow (+) and spin \downarrow (-) channels can be expressed as:

$$\mathbf{A}_{\pm}^d = \frac{1}{\sqrt{1 + \Delta^2}} \begin{bmatrix} (1 + \Delta)/2 \mp i(1 - \Delta)/2 \\ \mp i(1 + \Delta)/2 + (1 - \Delta)/2 \end{bmatrix}, \quad (5.72)$$

from which follows that $\mathbf{A}_-^d = (\mathbf{A}_+^d)^*$ are complex conjugate from each other. Nonetheless, they are generally not orthogonal in the presence of certain linear gain anisotropy. The two measurable optical laser polarization eigenmodes $\boldsymbol{\eta}_\pm$ derived from the diagonalization of the optical \mathcal{T} -matrix are then orthogonal. It may result in a non-orthogonality between \mathbf{A}_\pm^d and $\boldsymbol{\eta}_\pm$ as depicted in Fig. 5.5. This is the source of a strong mode coupling between the two transverse modes.

The resulting dipolar amplification matrix \mathcal{T} from Eq. (5.64) is given by:

$$\mathcal{T} = g_{00}(1 - i\alpha) \begin{bmatrix} \frac{1+\Delta^2}{2} & \frac{1-\Delta^2}{2} - i\mathcal{P}_s\Delta \\ \frac{1-\Delta^2}{2} + i\mathcal{P}_s\Delta & \frac{1+\Delta^2}{2} \end{bmatrix}, \quad (5.73)$$

where $g_{00}(1 - i\alpha)$ is the optical gain parameter. The \mathbf{E} -field in the QW obeys $\mathbf{E}^{(out)} - \mathbf{E}^{(in)} = g_{00}(1 - i\alpha)\mathcal{T}\mathbf{E}^{(in)}$ or $\mathbf{E}^{(out)} = \mathbf{T}\mathbf{E}^{(in)}$ where $\mathbf{T} = I_{2 \times 2} + \mathcal{T}$ admits an Hermitian form. As discussed before, we have also introduced the phase-amplitude Henry's coefficient α [114, 115] describing the local change in the optical constant from free carriers. Via a diagonalization procedure of \mathcal{T} (or \mathbf{T}), one finds the two different polarized eigenmodes we are searching for, $\boldsymbol{\eta}_{(1,2)}$, together with the optical gain $g_{(1,2)}$ as the corresponding eigenvalues. Those are given as a function of the spin-polarization of carriers \mathcal{P}_s and the oscillator strength anisotropy Δ :

$$\boldsymbol{\eta}_{(1,2)} = \frac{1}{\sqrt{2}} \begin{bmatrix} 1 \\ \pm \frac{\frac{1-\Delta^2}{2} - i\mathcal{P}_s\Delta}{\sqrt{\left(\frac{1-\Delta^2}{2}\right)^2 + (\mathcal{P}_s\Delta)^2}} \end{bmatrix}_{<100>}, \quad (5.74)$$

where the $<100>$ subscript means that the present expression for the modes is expressed in the cubic $<100>$ reference crystallographic axis. $g_{(1,2)}$ are expressed as:

$$g_{(1,2)} = g_0(N_+ + N_-) \left[\frac{1 + \Delta^2}{2} \pm \sqrt{\left(\frac{1 - \Delta^2}{2}\right)^2 + \mathcal{P}_s^2 \Delta^2} \right] \quad (5.75)$$

or

$$g_{(1,2)} = g_0(N_+ + N_-)\bar{g}_{(1,2)}. \quad (5.76)$$

In the above formula for $g_{(1,2)}$ the (+) sign refers to the mode (1) whereas the (-) sign refers to the mode (2). $\bar{g}_{(1,2)} = \frac{1+\Delta^2}{2} \pm \sqrt{\left(\frac{1-\Delta^2}{2}\right)^2 + \mathcal{P}_s^2 \Delta^2}$ are the reduced gains. One recovers $g_{(1,2)} = g_\pm = 1 \pm \mathcal{P}_s$ for $\Delta = 1$ (no linear anisotropy) whereas $g_{(1)} = 1$ and $g_{(2)} = \Delta^2$ for $\mathcal{P}_s = 0$ for the linear polarized pump, as expected. In the more general case, eigenmodes and corresponding gain display a more complex form. However, one can be convinced that the two sets of vectors $\boldsymbol{\eta}_{1,2}$ and \mathbf{A}_\pm^d are generally not collinear to each other, leading to a strong mode coupling between the two transverse modes $\boldsymbol{\eta}_1$ and $\boldsymbol{\eta}_2$ as discussed below. We note that $\mathcal{P}_s(\tau_s)$ in Eq. 5.67 depends on the spin-relaxation time τ_s and thus such effects can be included in the model.

Coupling between transverse modes.

We discuss here the impact of non-collinearity between $\boldsymbol{\eta}_{1,2}$ and \mathbf{A}_\pm^d on the transverse mode coupling, as sketched in Fig. 5.5, and leading to possible polarization beating. The possible

mode coupling between longitudinal modes [101] of the same polarization is not considered here because of the absence of any polarization beating. One gets the effective optical gain β_1^+ and β_2^- from the squared projection of the *natural* optical eigenmode polarization along the dipole source direction according to:

$$\beta_1^+ = |\langle \boldsymbol{\eta}_{(1)} | \mathbf{A}_+^d \rangle|^2 = \frac{1 + \sin(2\phi_1 + \phi_2)}{2} \quad (5.77)$$

$$\beta_2^- = |\langle \boldsymbol{\eta}_{(2)} | \mathbf{A}_-^d \rangle|^2 = \frac{1 - \sin(2\phi_1 - \phi_2)}{2} \quad (5.78)$$

as depicted in Fig. 5.5. In the same spirit, the coupling between modes or the *cross-coupling* terms θ_1^- and θ_2^+ [116–118], involving linear gain anisotropy, are calculated from the squared projection of the optical eigenmode polarization along the cross-dipole source direction:

$$\theta_1^- = |\langle \boldsymbol{\eta}_{(1)} | \mathbf{A}_-^d \rangle|^2 = \frac{1 + \sin(2\phi_1 - \phi_2)}{2}, \quad (5.79)$$

$$\theta_2^+ = |\langle \boldsymbol{\eta}_{(2)} | \mathbf{A}_+^d \rangle|^2 = \frac{1 - \sin(2\phi_1 + \phi_2)}{2}, \quad (5.80)$$

where ϕ_1 and ϕ_2 are given by

$$\phi_1 = \arctan\left(\frac{1 - \Delta}{1 + \Delta}\right) \quad (5.81)$$

$$\phi_2 = \arctan\left(\frac{2\mathcal{P}_s \Delta}{1 - \Delta^2}\right). \quad (5.82)$$

It results that θ_1^- and θ_2^+ couple the two mode amplitudes and that this coupling is strongly correlated to the linear gain dichroism Δ and the carrier spin polarization \mathcal{P}_S . A zero linear gain dichroism $\Delta = 1$ leads to no coupling $\theta_{1,2}^{\pm} = 0$ whatever the spin-polarization \mathcal{P}_S . The increase of the linear gain dichroism ($\Delta < 1$) increases the coupling between modes ($\theta_{1,2}^{\pm} > 0$) even in the case of a non-zero spin-polarization \mathcal{P}_S . The dynamics of carriers pumped are given by the generalization of Eq. (5.59):

$$\begin{aligned} \frac{\partial N_+}{\partial t} &= -\gamma(N_+ - N_{0+}) - \gamma_s(N_+ - N_-) \\ &\quad - \gamma \left(\bar{g}_{(1)}(N) \beta_1^+ \frac{I_{(1)}}{I_{sat}} + \bar{g}_{(2)}(N) \theta_1^- \frac{I_{(2)}}{I_{sat}} \right), \end{aligned} \quad (5.83)$$

$$\begin{aligned} \frac{\partial N_-}{\partial t} &= -\gamma(N_- - N_{0-}) + \gamma_s(N_+ - N_-) \\ &\quad - \gamma \left(\bar{g}_{(1)}(N) \theta_2^+ \frac{I_{(1)}}{I_{sat}} + \bar{g}_{(2)}(N) \beta_2^- \frac{I_{(2)}}{I_{sat}} \right), \end{aligned} \quad (5.84)$$

with the field intensity at saturation $I_{sat} = \frac{\epsilon_r c \hbar^2 (\Gamma^2 + \delta'^2) \gamma}{n \mu^2 \Gamma}$. We recover the expression for the dynamics of coupling modes vs. the coupling coefficient θ [32, 119] from the Lamb model (described in more details in Appendix A), that we have expressed vs. the linear gain dichroism parameter Δ appearing in $\bar{g}_{(1,2)}$, $\beta_{(1,2)}$ and $\theta_{(1,2)}$. In that picture, the overall

coupling coefficient \mathcal{C} [116–118] between the two transverse intensity modes $I_{(1)}$ and $I_{(2)}$ is written:

$$\begin{aligned} \mathcal{C} &= \frac{\theta_1^- \theta_2^+}{\beta_1^+ \beta_2^-} \\ &= \frac{(1 - \cos(2\phi_1) \sin(\phi_2))^2 - \sin^2(2\phi_1) \cos^2(\phi_2)}{(1 + \cos(2\phi_1) \sin(\phi_2))^2 - \sin^2(2\phi_1) \cos^2(\phi_2)}. \end{aligned} \quad (5.85)$$

The simultaneous oscillation of two orthogonally polarized states is ruled by the strength of the nonlinear coupling between the two eigenstates in the active medium. Whether the coupling constant \mathcal{C} is higher or lower than 1 leads, respectively, to two distinct regimes, namely, bistability and simultaneity [116]. In this case of laser modes with linearly polarized optical gain along the $[110]$ and $[1\bar{1}0]$ directions and no spin-polarized pump ($P_s = 0$), the respective gains are $g_{(1)} = 1$ and $g_{(2)} = \Delta^2$ as expected. These experimental conditions are often fulfilled in real situations with no spin-polarized carrier pump, corresponding to two possible linear modes along $[110]$ and $[1\bar{1}0]$ directions.

5.2.4 Source of linear birefringence in the optical cavity

Vector dipolar sources in active regions of VECSELs do not necessarily force the polarization to be emitted in the same direction because of the residual linear birefringences within the semiconductor multilayers. These anisotropic properties of the dielectric function strongly impacts the performance and properties of laser operation leading to the complex polarization dynamics and polarization switching [46]. Previous theoretical and experimental investigations allowed separation between two different contributions. The first anisotropy to consider is the unavoidable linear phase anisotropy induced by a possible local strain-field in the host material via electro-optical effects [68, 120] and originating, e.g., from the lattice mismatch [121] or from the crystal relaxation at the surface [38, 39, 42, 122]. As a result, the directional degeneracy between the two in-plane $[110]$ and $[1\bar{1}0]$ directions will be removed and the frequencies for the corresponding two linear polarizations will be split. The second source of anisotropy is the linear birefringence originating from the interface between ternary quantum wells and barriers (GaAsP/InGaAs/GaAsP). An in-plane optical anisotropy in III-V QWs was found due to the breakdown of the rotoinversion symmetry at interfaces when the host materials do not share any common atoms (symmetry breaking from D_{2d} to C_{2v}) [39] or due to an In chemical segregation [38]. This optical anisotropy has been evaluated by the pseudo-potential microscopic model as well as by k-p models including relevant electronic boundary conditions [39, 41, 123, 124]. Such an effect of linear birefringence in the QWs is generally measured by optical reflectance [78], by optical transmission [125] or by optical absorption [126]. In the next section, we will introduce the necessary 4×4 matrix formalism enabling us to describe the wave propagation inside the anisotropic multilayer laser cavity as described by Eq. (5.52) of the Maxwell-Bloch equations.

5.3 Generalization for emission from multilayer spin-laser and spin-LED

5.3.1 Description of the optical gain in multilayers

In this section, we describe the main properties of the optical gain tensor derived above and the propagation of the electromagnetic field inside the multilayer laser. One defines the amplitude of the source Jones vector in a Cartesian s - p basis according to $\mathbf{A}_{\text{down}}^d = [A_1^d; A_3^d]^T$ and $\mathbf{A}_{\text{up}}^d = [A_2^d; A_4^d]^T$ (with T transpose vectors) as illustrated in Fig. 5.6. Those describe the \mathbf{E} waves, respectively, propagating downward and upward. We call, respectively, $\mathbf{A}'_{\text{up,down}}$ and $\mathbf{A}''_{\text{up,down}}$ the amplitudes of the \mathbf{E} field traveling towards the respective *up* and *down* directions in the region of space below (') and above (') a given active QW region, as depicted in Fig. 5.6. Amplification effects by the dipole sources in the active layers can be expressed in the following matrix form:

$$\begin{bmatrix} \mathbf{A}'_{\text{up}} \\ \mathbf{A}''_{\text{down}} \end{bmatrix} = \begin{bmatrix} \mathbf{T}_{\text{uu}} & \mathbf{0} \\ \mathbf{0} & \mathbf{T}_{\text{dd}} \end{bmatrix} \begin{bmatrix} \mathbf{A}''_{\text{up}} \\ \mathbf{A}'_{\text{down}} \end{bmatrix} + \gamma_{sp} \begin{bmatrix} \mathbf{A}_{\text{up}}^d \\ \mathbf{A}_{\text{down}}^d \end{bmatrix}, \quad (5.86)$$

where the first term describes the stimulated emission involving the amplification tensor \mathbf{T}_{uu} and \mathbf{T}_{dd} (uu for up-ingoing and up-outgoing and dd for down-ingoing and down-outgoing), the precise form will be given later. The second term in the right-hand side of the equation describes the spontaneous emission (stochastic process) weighted by the coefficient γ_{sp} .

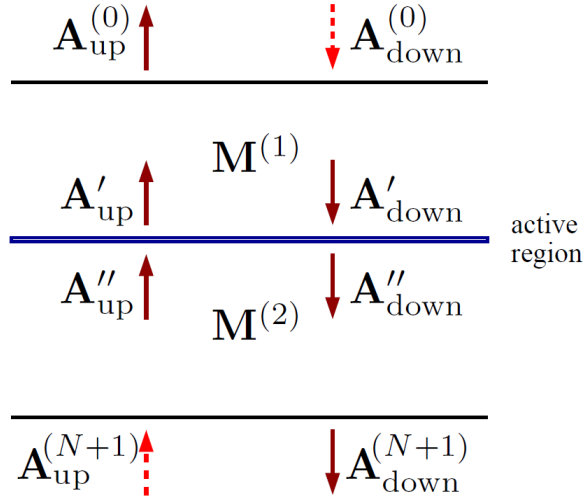


Figure 5.6: Schematic description of the structure with a single active layer showing wave propagation inside the cavity.

After reflections on mirrors and back and forth traveling, the wave polarization $\mathbf{A}'_{\text{down}}$ may be different from the source $\mathbf{A}_{\text{down}}^d$ because of residual birefringences (linear or circular) in the host. Note also that, for elliptical modes, polarization and Jones vectors are changed after reflections on Bragg mirrors leading to the definition of two different optical-gain tensors for up- and down- propagation. The result [45] is that one has to consider

the gain tensor, $\mathcal{T}_{mn}^{\alpha\beta}$, in a supermatrix form with double index, one $m, n = x, y, z$ for the coordinates and the other $\alpha, \beta = uu, dd$ for the propagation direction (*up, down*). In that sense, (*up, up*) means amplification from an *up-incoming* wave into an *up-outgoing* wave, and similarly for (*down, down*) combination.

Considering normalized vector sources, $(\mathbf{A}_{\text{down}}^d)^+ \mathbf{A}_{\text{down}}^d = 1$, \mathbf{T}_{uu} and \mathbf{T}_{dd} admit the form:

$$\mathbf{T}_{uu} = \mathbf{I} + g_{00} [1 - i\alpha\mathcal{T}_{uu}] \mathcal{T}_{uu} \quad (5.87)$$

with

$$\mathcal{T}_{uu} = \begin{bmatrix} A_2^d A_2^{d*} & A_2^d A_4^{d*} \\ A_4^d A_2^{d*} & A_4^d A_4^{d*} \end{bmatrix} \quad (5.88)$$

and

$$\mathbf{T}_{dd} = \mathbf{I} + g_{00} [1 - i\alpha\mathcal{T}_{dd}] \mathcal{T}_{dd} \quad (5.89)$$

with

$$\mathcal{T}_{dd} = \begin{bmatrix} A_1^d A_1^{d*} & A_1^d A_3^{d*} \\ A_3^d A_1^{d*} & A_3^d A_3^{d*} \end{bmatrix}, \quad (5.90)$$

returning to previous form for the amplification matrix \mathbf{T} . Here, \mathbf{I} is the 2×2 identity matrix. We recall that g_{00} is the scalar gain to find at threshold and $\alpha = \frac{\partial n_r / \partial N}{\partial n_i / \partial N}$ is the Henry's coefficient accounting for the relative change of the real part of the optical index (n_r) [114].

In the previous form given by Eq. (5.73), the expression for α dealing with a satellite mode does not take into account the gain saturation by the central mode. The previous expression of α in (5.87) and (5.89) is therefore changed into $\alpha\mathcal{T}_{uu}$ and $\alpha\mathcal{T}_{dd}$ in order to consider gain self-saturation without much computational effort. For example, if one considers for the case of $\mathcal{P}_s = 0$:

$$\mathcal{T}_{uu} = \begin{bmatrix} \frac{1+\Delta^2}{2} & \frac{1-\Delta^2}{2} \\ \frac{1-\Delta^2}{2} & \frac{1+\Delta^2}{2} \end{bmatrix}, \quad (5.91)$$

then by diagonalization procedure of the second term in (5.87) one finds

$$\begin{bmatrix} 1 - i\alpha & \\ & 1 - i\alpha\Delta^2 \end{bmatrix} \begin{bmatrix} 1 & \\ & \Delta^2 \end{bmatrix} \quad (5.92)$$

for the two different eigenmodes $\boldsymbol{\eta}_{(1,2)} = [1; \pm 1]$. Then the corresponding gains are $g_{(1)} = 1$ multiplied by the factor $1 - i\alpha$ and $g_{(2)} = \Delta^2$ multiplied by the factor $1 - i\alpha\Delta^2$. This difference causes a particular frequency splitting between two modes as expected and demonstrated in the next chapter.

5.3.2 Transfer and scattering matrix formalism for anisotropic cavity

We are now going to tackle the issue of propagation end eigenmodes in optical cavities including active regions (QWs), barriers, and Bragg mirrors. One considers first a single QW as an optical source. Fig. 5.6 displays a simple laser structure consisting of a *single active dipole layer* embedded in multilayer systems. The multilayers above and below the

active layer are described by transfer matrices $\mathbf{M}^{(1)}$ and $\mathbf{M}^{(2)}$. Those transfer matrices connect the amplitudes of the *outgoing* and *ingoing* waves from the external parts of the active layer to the *top* (1) and *bottom* (2), respectively. In that sense, the \mathbf{M} matrix contains all the optical properties of the host (birefringence, strain, and optical anisotropies) from the permittivity tensor. Moreover, the \mathbf{T} matrix includes information on the optical gain. More details are given in Appendix B. From (B.1), (B.2), and (5.86) we obtain a compact form of the basic equation for the calculation of the field amplitudes emitted from the structure $\mathbf{A}_{\text{up}}^{(0)}$ and $\mathbf{A}_{\text{down}}^{(N+1)}$:

$$\tilde{\mathbf{A}}_{\mathbf{M}} \begin{bmatrix} \mathbf{A}_{\text{up}}^{(0)} \\ \mathbf{A}_{\text{down}}^{(N+1)} \end{bmatrix} = -\gamma_{sp} \begin{bmatrix} \mathbf{A}_{\text{up}}^d \\ \mathbf{A}_{\text{down}}^d \end{bmatrix}, \quad (5.93)$$

where

$$\tilde{\mathbf{A}}_{\mathbf{M}} = \begin{bmatrix} -\tilde{\mathbf{M}}_{\text{uu}}^{(1)} & \mathbf{T}_{\text{uu}}\mathbf{M}_{\text{ud}}^{(2)} \\ \mathbf{T}_{\text{dd}}\tilde{\mathbf{M}}_{\text{du}}^{(1)} & -\mathbf{M}_{\text{dd}}^{(2)} \end{bmatrix}. \quad (5.94)$$

The condition for a resonant eigenmode (no spontaneous emission $\gamma_{sp} = 0$) is the zero determinant of the constituent matrix $\tilde{\mathbf{A}}_{\mathbf{M}}$. In the simplest case of a laser cavity of thickness d , wave vector $k_0 = 2\pi/\lambda$, and complex refractive index $n = n_r - in_i$, one obtains in this way the well-known condition for the resonance wavelength $k_0dn_r = m\pi$ by finding the zero of the imaginary part of the determinant. From the zero of its real part, one obtains $g = e^{k_0dn_i/2} - 1$, giving the condition for the optical gain g at the laser threshold. From (5.93), the conditions for resonance and eigenmodes for a single active layer are then generally given by:

$$\det \left[\tilde{\mathbf{A}}_{\mathbf{M}} \right] = 0 \quad (5.95)$$

or equivalently

$$\left[\mathbf{T}_{\text{dd}}\tilde{\mathbf{M}}_{\text{du}}^{(1)} \left(\tilde{\mathbf{M}}_{\text{uu}}^{(1)} \right)^{-1} \right]^{-1} = \mathbf{T}_{\text{uu}}\mathbf{M}_{\text{ud}}^{(2)} \left(\mathbf{M}_{\text{dd}}^{(2)} \right)^{-1}. \quad (5.96)$$

However, the transfer matrices $\mathbf{M}^{(1)}$ and $\mathbf{M}^{(2)}$ described by (B.1) and (B.2), respectively, connecting the upper and lower field amplitudes is only suitable to describe the *single active region*. One can easily be convinced that it cannot be extended to the case of *multiple QWs*. The scattering matrix (S-matrix) formalism is much more appropriate to treat this general case. It describes the amplification and optical propagation/diffusion of the *ingoing* wave amplitudes into *outgoing* wave-amplitudes. For more details see Appendix C. From (C.1), (C.2), and (5.86), one derives:

$$\tilde{\mathbf{A}}_{\mathbf{S}} = \begin{bmatrix} \mathbf{S}_{\text{uu}}^{(1)} & \mathbf{0} \\ \mathbf{0} & \mathbf{S}_{\text{dd}}^{(2)} \end{bmatrix}^{-1} \begin{bmatrix} \mathbf{T}_{\text{ud}}\mathbf{S}_{\text{du}}^{(1)} - \mathbf{I} & \mathbf{T}_{\text{uu}}\mathbf{S}_{\text{ud}}^{(2)} \\ \mathbf{T}_{\text{dd}}\mathbf{S}_{\text{du}}^{(1)} & \mathbf{T}_{\text{du}}\mathbf{S}_{\text{ud}}^{(2)} - \mathbf{I} \end{bmatrix}, \quad (5.97)$$

where \mathbf{I} is the 2×2 unit matrix. The $\tilde{\mathbf{A}}_{\mathbf{S}}$ matrix in Eq. (5.97) is in a more general expression suitable for recursive calculations. \mathbf{T} defined in (5.86) is generalized into a more general form including possible off-diagonal submatrices \mathbf{T}_{ud} and \mathbf{T}_{du} required to describe coherent multiple reflections and interference effects between two active regions (discussed in details in the next subsection). These cannot be included in the \mathbf{M} -matrix formulation and they

are derived from a general recursive formula detailed hereafter. In the case where $\mathbf{T}_{ud} = \mathbf{T}_{du} = \mathbf{0}$ (a single active region is considered), finding the zero-determinant of the $\tilde{\mathbf{A}}_M$ and $\tilde{\mathbf{A}}_S$ matrices in Eqs. (5.94) and (5.97) gives naturally equivalent results for optical modes (polarization, wavelength) and gain (threshold). The conditions for resonance and eigenmodes for multiple-QWs structures are:

$$\det \left[\tilde{\mathbf{A}}_S \right] = 0 \quad (5.98)$$

or equivalently

$$\det \begin{bmatrix} \mathbf{T}_{ud}\mathbf{S}_{du}^{(1)} - \mathbf{I} & \mathbf{T}_{uu}\mathbf{S}_{ud}^{(2)} \\ \mathbf{T}_{dd}\mathbf{S}_{du}^{(1)} & \mathbf{T}_{du}\mathbf{S}_{ud}^{(2)} - \mathbf{I} \end{bmatrix} = 0 \quad (5.99)$$

that we will consider now by implementing a general recursion method for deriving \mathbf{S} and \mathbf{T} tensors in the most general cases. The resonant condition can be written as:

$$\left[\mathbf{T}_{dd}\mathbf{S}_{du}^{(1)} \left(\mathbf{T}_{ud}\mathbf{S}_{du}^{(1)} - \mathbf{I} \right)^{-1} \right]^{-1} = \mathbf{T}_{uu}\mathbf{S}_{ud}^{(2)} \left(\mathbf{T}_{du}\mathbf{S}_{ud}^{(2)} - \mathbf{I} \right)^{-1} \quad (5.100)$$

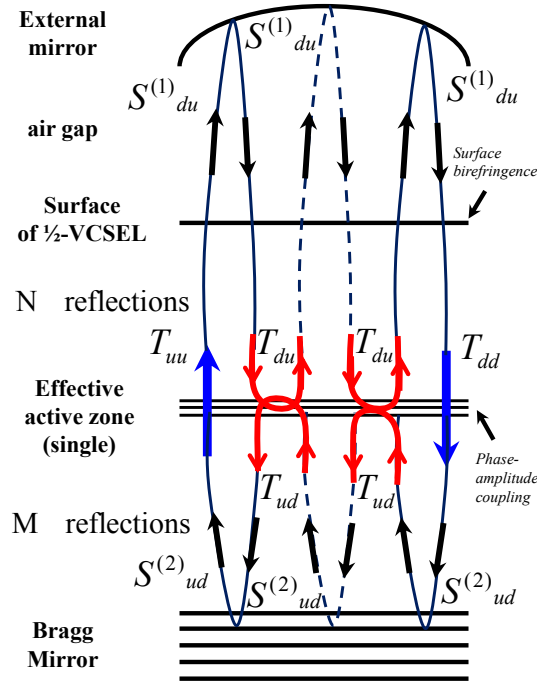


Figure 5.7: Sketch of the phase matching in a 1/2 VCSEL structure involving multiple reflection, propagation, and amplification processes in the optical semiconductor cavity containing one effective active layer, the properties of which are derived by recursive method. \mathbf{S}_{du} and \mathbf{S}_{ud} correspond to propagation and reflection effects with respective N (top) and M (bottom) reflections processes. \mathbf{T}_{ud} and \mathbf{T}_{du} represent reflection after amplification in the effective active zone whereas \mathbf{T}_{uu} and \mathbf{T}_{dd} correspond to forward amplification.

or equivalently:

$$\begin{aligned} \mathbf{T}_{dd}\mathbf{S}_{du}^{(1)} \left(\mathbf{T}_{ud}\mathbf{S}_{du}^{(1)} - \mathbf{I} \right)^{-1} \mathbf{T}_{uu}\mathbf{S}_{ud}^{(2)} \left(\mathbf{T}_{du}\mathbf{S}_{ud}^{(2)} - \mathbf{I} \right)^{-1} &= \mathbf{I} \\ \mathbf{T}_{dd}\mathbf{S}_{du}^{(1)} \sum_N \left(\mathbf{T}_{ud}\mathbf{S}_{du}^{(1)} \right)^N \mathbf{T}_{uu}\mathbf{S}_{ud}^{(2)} \sum_M \left(\mathbf{T}_{du}\mathbf{S}_{ud}^{(2)} \right)^M &= \mathbf{I} \end{aligned} \quad (5.101)$$

giving the general phase-matching conditions for the optical waves after all possible optical pathways (S -matrix) and amplifications (T -matrix) in the optical cavity. In that sense, N and M are the number of the partial back-and-forth travelings in the respective upper and down part of the cavity (see Fig. 5.7).

5.3.3 Generalization to emission from multiple QW: Recursive formulas for multiple active QW regions

The S -matrix scheme adopted here is suitable to describe multiple optical active zones, their optical amplification, and the propagation of the electromagnetic inside the cavity. In particular, the S -matrix scheme enables us to provide a recursive formula for the optical gain involving multiple dipole sources that could be implemented in numerical procedures for the derivation of optical eigenmodes of VCSELs and spin-VCSELs. The result is the following. Let us consider that the dipole active layers are described by the dipole source vectors $\mathbf{A}^{(n)d}$ and $\mathbf{A}^{(n+1)d}$ and the optical gain tensor $\mathbf{T}^{(n)}$ and $\mathbf{T}^{(n+1)}$. The definition of vectors and optical gain are similar to (5.86). The effective dipole layer is found by using the following generalized relationship:

$$\begin{bmatrix} \mathbf{A}_{\text{up}}^{(n)'} \\ \mathbf{A}_{\text{down}}^{(n+1)''} \end{bmatrix} = \mathbf{T}^{(n,n+1)} \begin{bmatrix} \mathbf{A}_{\text{up}}^{(n+1)''} \\ \mathbf{A}_{\text{down}}^{(n)'} \end{bmatrix} + \mathbf{A}^{(n,n+1)d}, \quad (5.102)$$

where $\mathbf{T}^{(n,n+1)}$ is in the form

$$\mathbf{T}^{(n,n+1)} = \begin{bmatrix} \mathbf{T}_{uu}^{(n,n+1)} & \mathbf{T}_{ud}^{(n,n+1)} \\ \mathbf{T}_{du}^{(n,n+1)} & \mathbf{T}_{dd}^{(n,n+1)} \end{bmatrix}. \quad (5.103)$$

The equivalent dipole source vector, $\mathbf{A}^{(n,n+1)d}$, and optical gain tensor $\mathbf{T}^{(n,n+1)}$ of the total system are written:

$$\mathbf{T}^{(n,n+1)} = \begin{bmatrix} \mathbf{0} & \mathbf{T}_{ud}^{(n)} \\ \mathbf{T}_{du}^{(n+1)} & \mathbf{0} \end{bmatrix} + \mathbf{B} \begin{bmatrix} \mathbf{T}_{uu}^{(n+1)} & \mathbf{0} \\ \mathbf{0} & \mathbf{T}_{dd}^{(n)} \end{bmatrix}, \quad (5.104)$$

$$\mathbf{A}^{(n,n+1)d} = \mathbf{A}^{(n)d} + \mathbf{B} \mathbf{A}^{(n+1)d}, \quad (5.105)$$

where

$$\mathbf{B} = \begin{bmatrix} \mathbf{T}_{uu}^{(n)} \mathbf{S}_{uu}^{(n)} & \mathbf{T}_{uu}^{(n)} \mathbf{S}_{ud}^{(n)} \\ \mathbf{T}_{dd}^{(n+1)} \mathbf{S}_{du}^{(n)} & \mathbf{T}_{dd}^{(n+1)} \mathbf{S}_{dd}^{(n)} \end{bmatrix} \begin{bmatrix} \mathbf{I} - \mathbf{T}_{ud}^{(n+1)} \mathbf{S}_{du}^{(n)} & -\mathbf{T}_{ud}^{(n+1)} \mathbf{S}_{dd}^{(n)} \\ -\mathbf{T}_{du}^{(n)} \mathbf{S}_{uu}^{(n)} & \mathbf{I} - \mathbf{T}_{du}^{(n)} \mathbf{S}_{ud}^{(n)} \end{bmatrix}^{-1}. \quad (5.106)$$

Note that the effective \mathbf{T} matrix consists of non-zero off-diagonal sub-matrices \mathbf{T}_{ud} and \mathbf{T}_{du} , describing coherent reflection processes between consecutive active regions. In Sec. 6.2, we will show that \mathbf{T}_{ud} and \mathbf{T}_{du} may largely impact the resonance conditions on the wavelength and the frequency splitting in anisotropic VCSELs. More details of the numerical recursive procedure are shown in Appendix C.

5.4 Conclusion of the chapter

The mathematical approach presented in this chapter and published in our paper [37] offers a powerful method for modeling of the laser eigenmodes of VCSELs and spin-VCSELs lasers with the local linear birefringence and the linear gain dichroism caused by symmetry reduction on the III-V semiconductor interfaces, surface reconstruction and strain effects. Recursive formulas used for calculation of the effective active region enable to include the interference and reflection effects between both active regions together with amplification of multiple reflected light inside the MQWs region. In the next chapter we reveal the important role of the different local birefringences in the eigenmodes and frequency splitting together with the need to correctly describe optical amplification.

Chapter 6

Application of formalism to the real 1/2 (spin-) VECSELs and spin-LEDs

Chapter 6 is focused on a numerical and experimental investigation of the local anisotropies in LED and VCSEL cavities. We start with a simplified model of multilayer spin-LED structure, which includes magneto-optical spin-injector and we show the effect of magneto-optical effects on the emitted polarization state. Then we will use derived S-matrix recursive formalism for modeling of a frequency splitting and we will compare it with experimentally measured values in order to extract anisotropic permittivity tensors of surface layers and quantum wells of real VCSEL structures. The chapter is completed by numerical simulation of the polarization states of emitted eigenmodes including local anisotropies such as linear gain dichroism and surface strain.

6.1 Model of realistic single-source spin-LED

In this section we will demonstrate our approach on half spin-VCSEL structure in LED regime (with spontaneous emission), which is constituted of only one DBR. Such structures can benefit from the external cavity degree of freedom ensured by an external mirror, which is placed outside to stimulate Fabry-Perot resonance.

For the following model, the particular form of the Jones source vector (5.72) will be used. From the previous section, it becomes now clear that if 100% spin-polarized carriers are injected in the active medium with a $m_j = 1/2$ state, the emitted light will consist of photons with both negative (σ^-) and positive (σ^+) helicity at the 3:1 ratio (in the $+z$ direction \downarrow). Recalling N_{\pm} the densities of electrons in the $\pm 1/2$ electron states and $\theta^{(n)}$ the propagation angle in n-th layer, we can use the following combination of the dipole sources in a simplified scheme according to:

$$\begin{aligned} \mathbf{A}_{\downarrow\uparrow}^d &= \frac{N_+}{N_+ + N_-} \left[\sqrt{\xi_{HH}} \begin{pmatrix} 1 \\ -i\cos\theta^{(n)} \end{pmatrix} + e^{i\tilde{\varphi}} \sqrt{\xi_{LH}} \begin{pmatrix} 1 \\ i\cos\theta^{(n)} \end{pmatrix} \right] + \\ &+ \frac{N_-}{N_+ + N_-} \left[\sqrt{\xi_{LH}} \begin{pmatrix} 1 \\ -i\cos\theta^{(n)} \end{pmatrix} + e^{i\tilde{\varphi}} \sqrt{\xi_{HH}} \begin{pmatrix} 1 \\ i\cos\theta^{(n)} \end{pmatrix} \right], \end{aligned} \quad (6.1)$$

where ξ_{LH} and ξ_{HH} are normalized transition probabilities defined by

$$\xi_{HH} = 3/4 \quad \xi_{LH} = 1/4 \quad \xi_{HH} + \xi_{LH} = 1. \quad (6.2)$$

We consider the outside angle of emission $\theta^{(0)} \in \langle 0, \pi/2 \rangle$ for $\mathbf{A}_{\downarrow\uparrow}^d$. By averaging the final Stokes intensities over the random phase $\tilde{\varphi}$, we describe the independence of stochastic HH and LH transitions. If we consider anisotropic non-stochastic emission by specific broken symmetry, particular $\tilde{\varphi}$ can be chosen for describing preferential emitted polarization e.g. in the case of strain-induced broken symmetry of interfaces with GaAs quantum wells [127].

The polarization state of the emitted light is then calculated by solving of Eq. (5.93). In the simple case of an isotropic structure and for purely spontaneous emission (with gain $g = 0$), this approach corresponds to the approach described by Benisty [128]. However, note that the spontaneous emission is not a coherent process and thus the terms $\gamma_{sp}\mathbf{A}_{up}^d$ and $\gamma_{sp}\mathbf{A}_{down}^d$ have to be added incoherently to the incident wave. In the present method we suppress possible interference effects originating from coherence spurious superposition. To that goal, we consider breaking phase factor $e^{i\tilde{\varphi}}$ of the source vector on the right side of Eq. (5.93) so that $\mathbf{A}_{down}^d = [A_1^d; A_3^d]^T$ and $\mathbf{A}_{up}^d = e^{i\tilde{\varphi}}[A_2^d; A_4^d]^T$ (with T transpose vectors). Then by averaging outside Stokes vector components over $\tilde{\varphi}$:

$$S_{out} = \left\langle S_{out}^{\uparrow,\downarrow}(\tilde{\varphi}) \right\rangle_{\tilde{\varphi}}, \quad (6.3)$$

we succeed to obtain outside Stokes vector of the structure with polarized source including the inherent incoherence property of spontaneously emitted waves.

Figure 6.1: Modeled spin-structure shown schematically including the gold capping layer (Au), magneto-optical spin-injector (Co), tunnel barrier (MgO), active layer GaAs with an active plane in the center and Bragg structure AlAs/InGaAs.

Figure 6.1 schematically displays the model of the multilayered structure including, from top to bottom, the metallic capping layer (Au), the magnetic and magneto-optically active thin spin-injector (Co) described in a polar geometry $\varepsilon_{xy}^{(Co)} = -\varepsilon_{yx}^{(Co)} = -1.14 + 0.19i$ [129], the oxide tunnel barrier (MgO) dedicated to electrical spin-injection issue [12, 130, 131], the active layer GaAs with the active medium QW (plane) in the center and a Bragg reflector at the bottom. The energy of the emitted light was for demonstration fixed to $E = 1.6$ eV, corresponding to the wavelength of $\lambda = 775$ nm. Optical constants for the materials in the structure are $n_{Au} = 0.17 - 4.86i$ [88], $n_{Co} = 2.44 - 4.71i$ [132], $n_{MgO} = 1.73$ [89], $n_{GaAs} = 3.69 - 0.01i$, $n_{AlAs} = 3.02$, and $n_{InGaAs} = 3.76 - 0.28i$ [89]. Note, that all plots describe emission to the halfspace (0) in direction \uparrow with the chosen parameters for the spontaneous emission $\gamma_{sp} = 1$ and for the stimulated emission $g_0 = 1$.

Figures 6.2 demonstrates the changes of the Stokes vector components when varying the injected carrier spin-polarization defined by (5.67). We observe two effects on outgoing emitted light polarization: (i) an effect of the injected spin polarization described by the

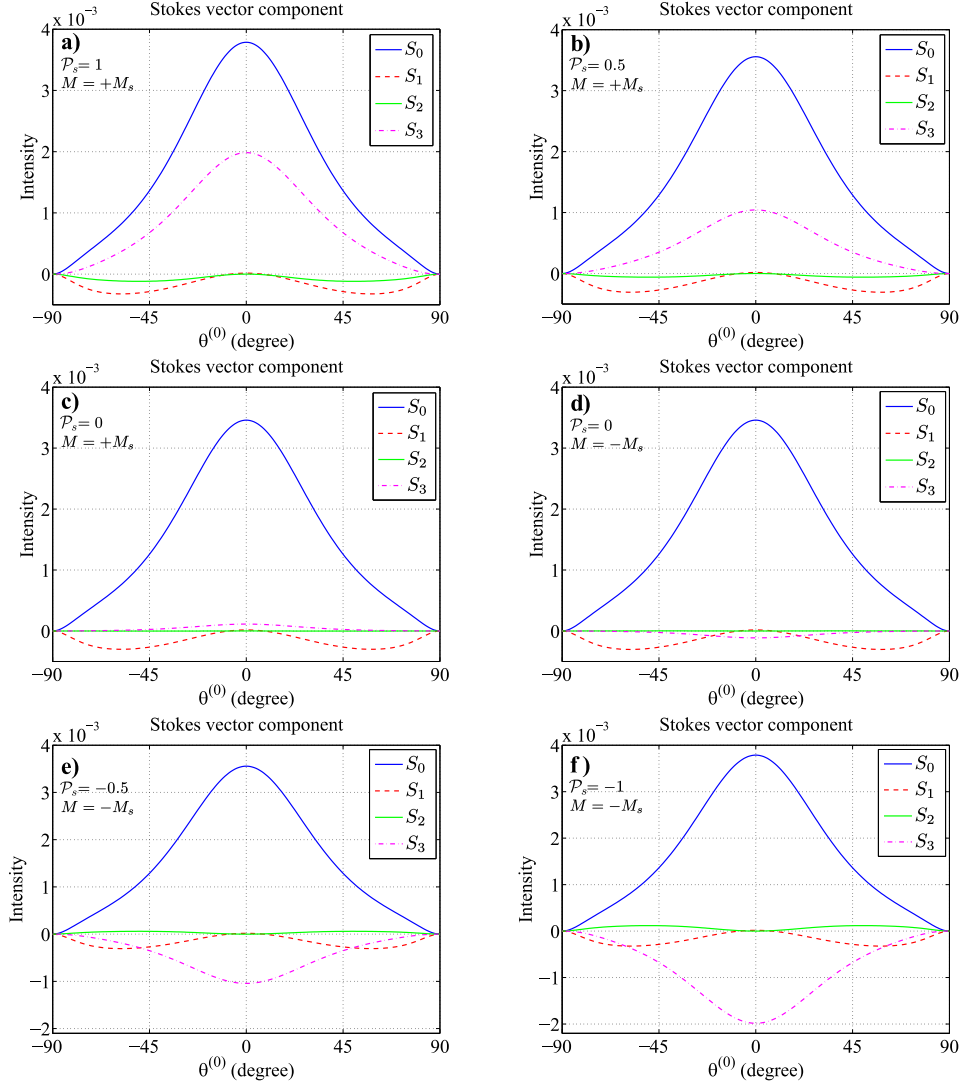


Figure 6.2: The effect of the electron spin polarization. Subplots show emission pattern for varying injected spin polarization $\mathcal{P}_s = 1$ (a), $\mathcal{P}_s = 0.5$ (b), and $\mathcal{P}_s = 0$ (c) with the magnetization of Co layer oriented in the $+z$ direction. Subplots d), e), and f) show emission pattern for varying injected spin polarization $\mathcal{P}_s = 0$, $\mathcal{P}_s = -0.5$ and $\mathcal{P}_s = -1$, respectively, with the magnetization of Co layer oriented in the $-z$ direction.

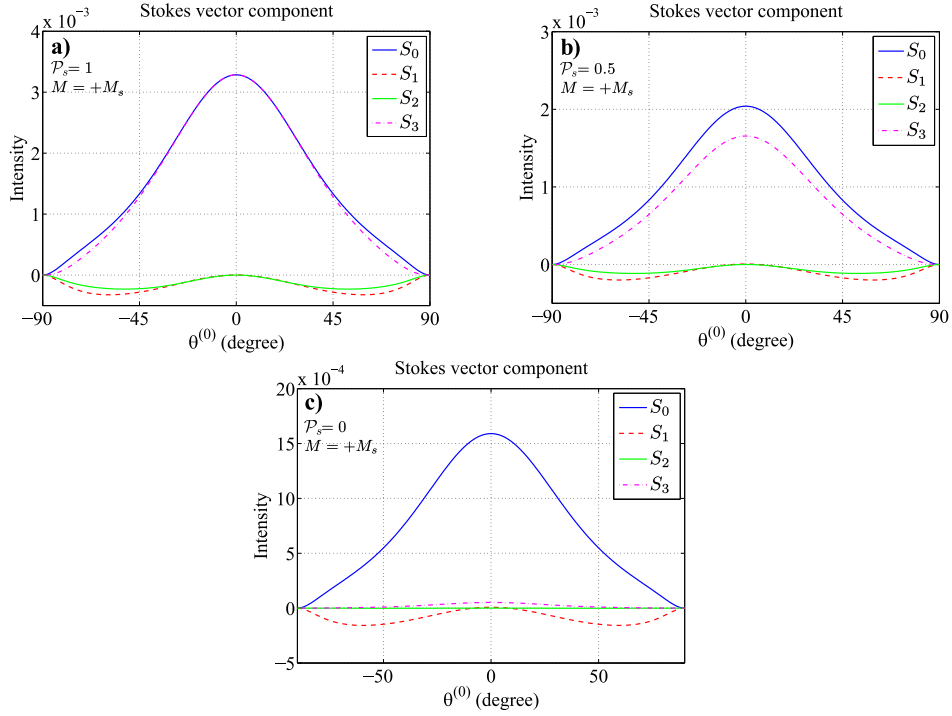


Figure 6.3: The effect of the electron spin polarization in the case of the heavy hole transitions. Subplots show emission pattern for varying injected spin polarization $\mathcal{P}_s = 1$, $\mathcal{P}_s = 0.5$, and $\mathcal{P}_s = 0$ with the magnetization of Co layer oriented in the $+z$ direction.

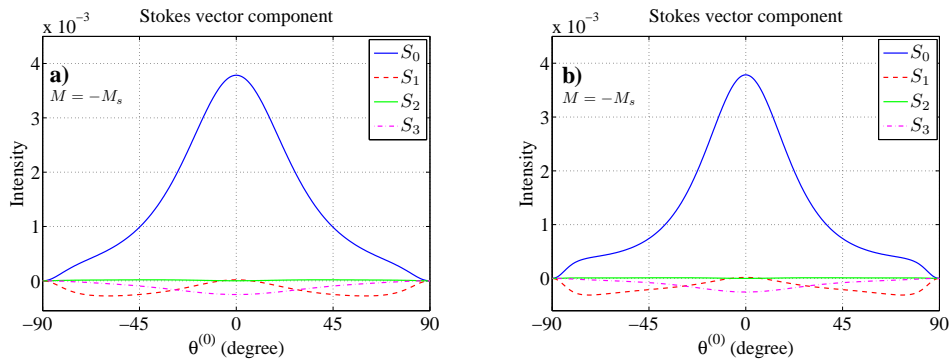


Figure 6.4: Effect of thickness $d^{(n)} = d_{GaAs}$ in the case of the hh transitions. Subplot a) $d_{GaAs} = 4\lambda/n_{GaAs}$ and subplot b) $d_{GaAs} = 8\lambda/n_{GaAs}$.

spin-polarization parameter \mathcal{P}_s and (ii) polarization effects originating by transmission and reflection from the magneto-optical Co layer. The effect of the injected spin polarization is related to the transition probabilities for heavy and light holes (see Figure 2.1). For the spin polarization $\mathcal{P}_s = 1$ (subplot a of Fig. 6.2), both heavy hole transition (resulting in RCP in $-z$ direction) and light hole transition (resulting in LCP) polarization are involved, while HH transitions are three times more probable than LH transitions.

Moreover the total intensity S_0 changes slightly. These changes are caused by the selective polarization transmission through the structure related to Faraday magneto-optical effect in the ferromagnetic Co layer. Circularly polarized eigenmodes in Co layer with perpendicularly oriented magnetic field are absorbed differently and have different velocity due to the magnetic circular dichroism and birefringence, respectively. After crossing the Co layer, the input wave transforms in such a way that its azimuth is rotated and its polarization becomes generally elliptical. Thus even if unpolarized carriers $\mathcal{P}_s = 0$ are injected (subplot c and d of Fig. 6.2) and the source is linearly polarized, we can observe non-zero circular S_3 component, which has different sign for opposite magnetic field orientation. The component S_3 switches sign due to different transition probabilities for different current spin-polarization \mathcal{P}_s (subplot e and f of Fig. 6.2). Experimental measurement of the Stokes vector can thus bring valuable information about injected spin-polarized current.

Figure 6.3 displays the evolution of the Stokes vector components when varying the injected spin polarization in the case of the heavy hole transitions ($\xi_{HH} = 1$). As expected for the injected current $\mathcal{P}_s = 1$, 100% circularly-polarized light is emitted. As can be seen in Figure 6.4, the thickness of the GaAs film has an impact on outside field pattern due to the interference effects.

6.2 Emission from 1/2-VCSELS structures with linear birefringence and gain dichroism: model vs. experiments

We turn now to experiments and connect our calculation method to some real experimental 1/2-VECSELS structures for two different cavity geometries involving linear birefringences. The typical set-up is displayed in Fig. 6.5. This section includes robust numerical predictions for eigenmodes with strong local linear birefringence and linear gain anisotropy effects. The results are compared to experimental measurements with the goal to disentangle both surface and interface anisotropies. We will consider two different sources of linear birefringence at the interface and/or in the QWs.

6.2.1 Main physical issues: From a single source to multiple QWs recursion

It is well-known that the birefringence in the laser optical cavity may induce a degeneracy shift of the optical frequencies of polarized eigenvectors, leading to a frequency splitting in the radio-frequency (RF) domain due to difference of their optical path. A simple model for the derivation of the corresponding phase or frequency splitting between two consecutive

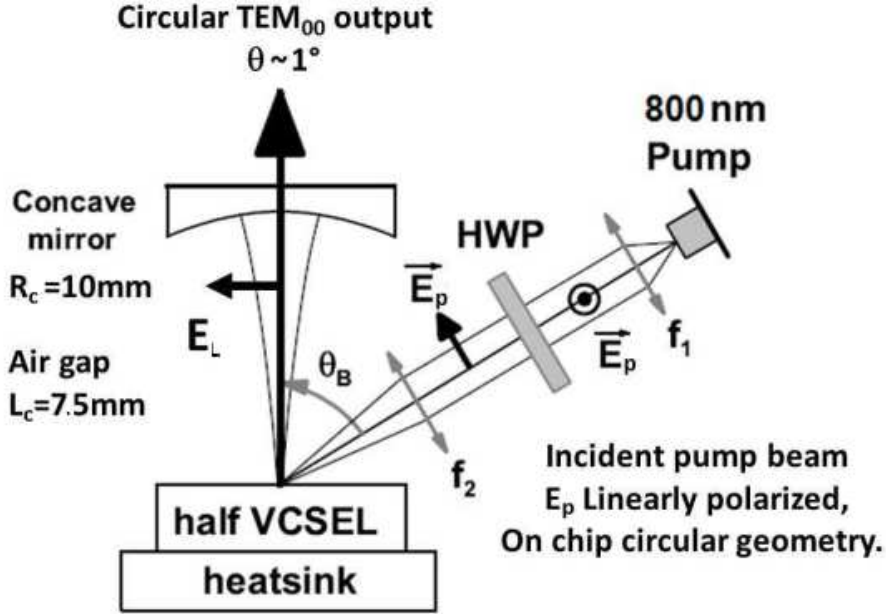


Figure 6.5: Sketch and geometry of the 1/2-VCSEL devices investigated in this study showing 1/2-VCSEL structure as the gain mirror, the optical pumping system, and the stable plano-concave-type optical cavity (air gap $L_c = 7.5$ mm) [70, 133, 134].

modes after one round trip in the optical cavity of length L_c is given by [112]:

$$\Delta\varphi_l = 2k_0L_c\Delta n, \quad (6.4)$$

where $\Delta n = n_y - n_x$ is the modal optical index difference between the eigenvector axis (integrated over the cavity length), and k_0 is the free-space wavevector of light. The frequency splitting is given by $2\pi\Delta f = -\Delta\varphi_l c / 2\bar{n}L_c$ where \bar{n} is the average modal index.

In the non intentionally doped GaAs-based nanostructures considered here, emitting vertically along the [001] crystal axis under optical pumping (no vertical static electric field applied), the typical sources of linear optical anisotropy, and thus birefringence, might find their origin in three characteristic regions [70]:

- At the Bragg interfaces;
- In the QW layers;
- At the top air-semiconductor interface.

We will consider the latter two contributions as the strongest. An important remark is that the effective phase-amplitude birefringence in QWs depends on the optical gain and then on the losses unlike purely electro-optic birefringence arising from the surface.

The power of the proposed method is to correctly include the gain properties in a self-consistent manner. For instance, we will show that restricting ourselves to the use of a simple round-trip model suppressing main interferences and inter-QW amplification

[switching-off \mathbf{T}_{ud} and \mathbf{T}_{du} in Eq. (5.97)] may lead to inaccuracy in the determination of the birefringence from the value of the average refractive index, Δn .

6.2.2 Modeling real VECSELS involving linear anisotropies.

Description of the 1/2-VCSEL structures.

We consider two different structures (S1 and S2 for samples 1 and 2) schematically shown in Fig. 6.6, the anisotropic optical properties of which have been investigated by high-resolution microwave RF-techniques [70]. In details, the non intentionally doped 1/2-VCSEL structure was grown by MOCVD on a [001] GaAs substrate [135]. Structures S1 and S2 are composed of a high reflectivity (99.9%) bottom AlAs/GaAs Bragg mirror (31.5 pairs), and a GaAs active layer of $13\lambda/2$ thickness containing six strain-balanced InGaAs/GaAsP QWs emitting at $\lambda \simeq 1\ \mu\text{m}$ for S1 and $\lambda \simeq 1.06\ \mu\text{m}$ for S2. Each QW is placed at an antinode of the optical standing wave, following a non-uniform longitudinal distribution ensuring uniform QWs carrier excitation. This ensures a low threshold carrier density and homogeneous gain broadening as needed for single longitudinal mode operation [70, 134, 135]. Structure S1 is terminated by a dielectric anti-reflection coating. Structure S2 is ended by a moderately reflective top epitaxial AlGaAs Bragg mirror, that may affect the sensitivity of the surface and QW anisotropy. This leads to an optical confinement of the electromagnetic field which is strongly enhanced on the QWs. The VECSEL devices are depicted in Fig. 6.5. The gain structures were optically pumped in the GaAs barriers close to Brewster incidence angle θ_B , by using a linearly polarized single mode 800-nm laser diode, focused with a pair of aspheric lenses with the focal lengths f_1 and f_2 on a $\simeq 35\text{-}\mu\text{m}$ spot radius with a circular in-plane geometry. The passive optical cavity is a high finesse stable plano-concave resonator of $L_c \simeq 7.5\ \text{mm}$, closed by a concave output coupler ($T = 0.7\%$ for S1 and 13% for S2) of radius of curvature $R_c = 10\ \text{mm}$. The minimum waist of the Gaussian beam occurs at the plan mirror. The typical fundamental TEM₀₀ beam waist is $w_0 \sim 37\ \mu\text{m}$ here, and exhibits a circular geometry. From an experimental point of view, in contrast to the case of monolithic micro-cavity-VCSEL devices [110, 133, 136], for conventional VECSELS both the frequency splitting and the power beating between polarization eigenmodes are too small to be able to be measured using optical spectrometers. Those experiments are thus based on the mixing of the two orthogonal cavity eigenvectors (see Siegman's book for reference [112]), and on the observation of the beat note in the RF domain, by measuring on a photodiode the power spectral density of the laser total power fluctuations [70, 112], as shown in Fig. 6.7.

Optical constants.

The optical constants $\varepsilon = n^2$ used in the calculation are the following: $\varepsilon_{GaAs}(\lambda = 1000\ \text{nm}) = 12.3$, $\varepsilon_{GaAs}(\lambda = 1060\ \text{nm}) = 12.09$, $\varepsilon_{AlAs}(\lambda = 1000\ \text{nm}) = 8.7$, $\varepsilon_{AlAs}(\lambda = 1060\ \text{nm}) = 8.63$ [88], $\varepsilon_{InGaAs}(\lambda = 1000\ \text{nm}) = 13.1$, $\varepsilon_{InGaAs}(\lambda = 1060\ \text{nm}) = 12.9$ [89], $\varepsilon_{GaAsP}(\lambda = 1000\ \text{nm}) = 12.15$, and $\varepsilon_{GaAsP}(\lambda = 1060\ \text{nm}) = 11.9$ [137]. These optical constants are also in agreement with ellipsometry measurements and modeling that we have recently performed [43] and that are shown in Chapter 4. Concerning the InGaAs quantum well, we switched off the imaginary part of the optical constant being replaced by the optical gain as a controlled input parameter.

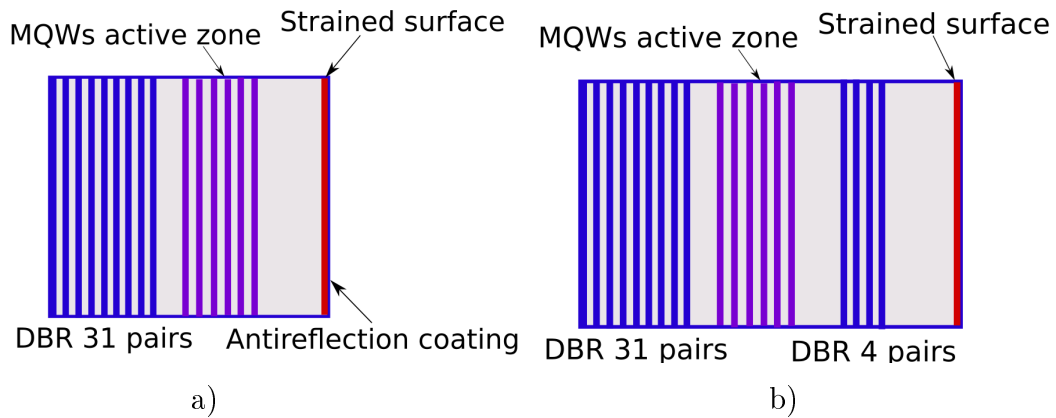


Figure 6.6: Description of the 1/2-VECSEL structures under study a) without (S1, left) and b) with (S2, right) the moderately reflective Bragg mirror. S1 is composed of an antireflection coating at the surface.

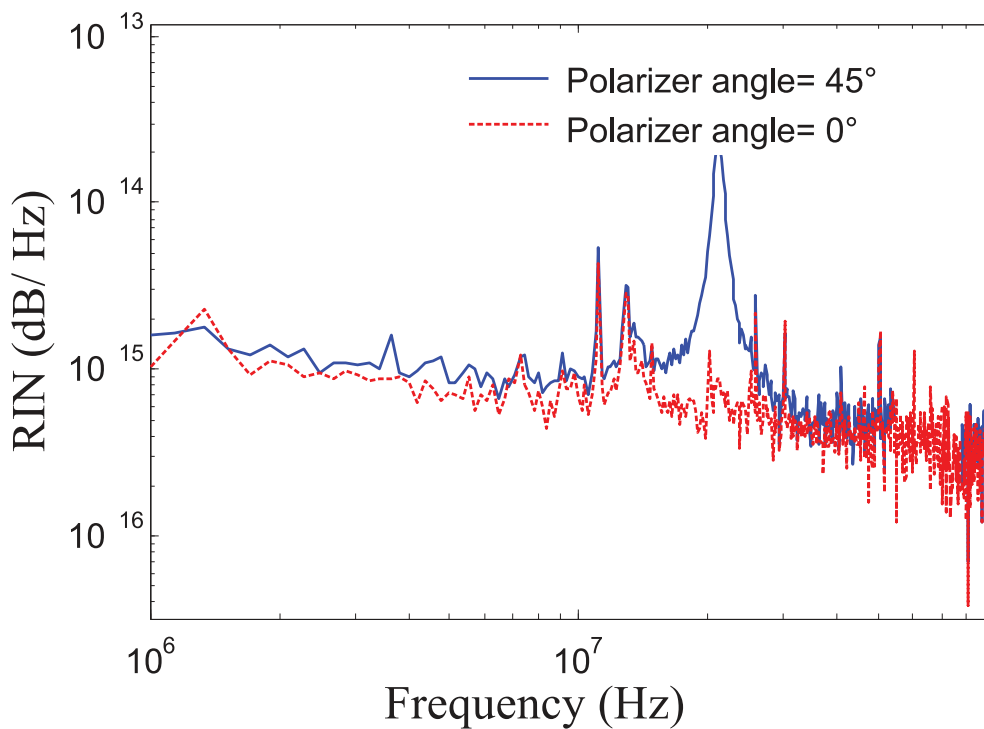


Figure 6.7: Experimental birefringence measurement, via orthogonal E-field polarization mode beating on a low noise photodiode with a laser beam passing through a polarizer rotated at 45° from [110] axis: an example of measured RF-spectrum, obtained with Sample 1 in a 7.5 mm long cavity and a concave output coupler with $T = 0.7\%$. The absence of the peak in the red dashed curve, confirms that the observed beat note is due the orthogonal polarization mode [70].

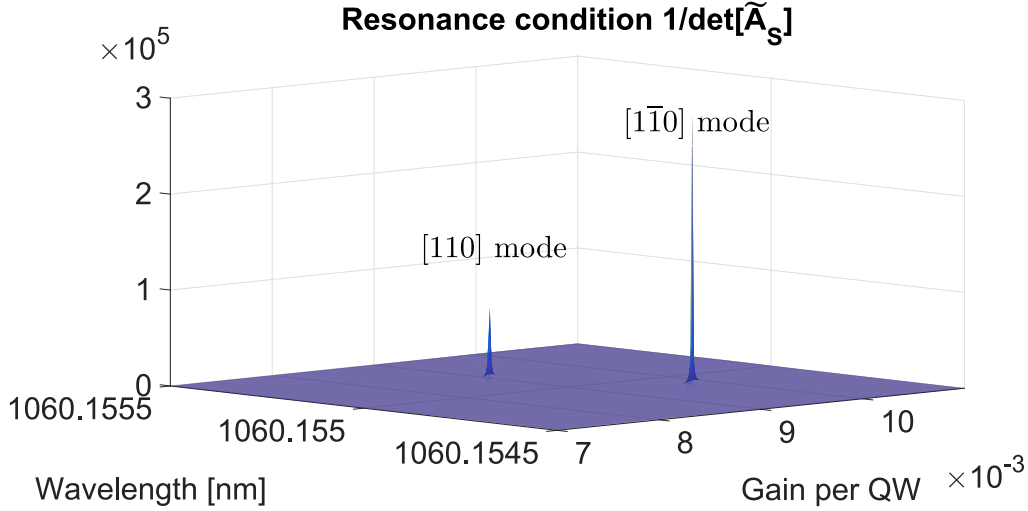


Figure 6.8: Calculation of the resonance conditions of Sample 2 for two linearly polarized eigenmodes oriented along the $[110]$ and $[1\bar{1}0]$ direction and $\Delta\varepsilon_s = 0.02$. Δ was taken equal to 0.95.

Detailed birefringence analysis on 1/2-VCSELS.

We are going now to apply our numerical method to three different physical situations of a) a linear birefringence at the surface only b) an intrinsic linear birefringence in QWs, and c) a linear birefringence at the surface and phase-amplitude coupling in QWs.

Case a) The laser resonance can be found by searching for the maximum of $1/\det[\tilde{\mathbf{A}}_S]$ in Eq. (5.99). To obtain laser parameters, we calculate the $1/\det[\tilde{\mathbf{A}}_S]$ as a function of wavelength λ and gain g_{00} via a step-by-step mesh-calculation procedure. Under these conditions, one finds a comb of resonance doublets, as expected, two representatives of which are plotted in Fig. 6.8 for Sample 2. The linear gain dichroism has been fixed at $\Delta = 0.95$ in the present example and the linear birefringence at the surface $\Delta\varepsilon_s = (\varepsilon_{x'x'} - \varepsilon_{y'y'})/2 = 0.02$, where $\varepsilon_{x'x'}$ and $\varepsilon_{y'y'}$ are the permittivity tensor components of a surface layer along the directions parallel to $[110]$ and $[1\bar{1}0]$, respectively, as depicted in Fig. 5.4. The thickness of the birefringent surface layer has been fixed to 50 nm. The analysis of the eigenmode polarization demonstrates an orientation of the \mathbf{E} -wave along respective $[110]$ and $[1\bar{1}0]$ directions for the whole doublets. One can note that the two consecutive peaks occur at two different frequencies as expected from the linear birefringence and moreover occur for two different calculated amplitude gains, respectively, 0.85 and 0.95 per each quantum well for loss compensation and corresponding to external mirror transmission of about 13% on the electromagnetic wave intensity ($6 \times \text{QWs} \times 2$ on the intensity gain). The relative difference of the gain of about 10% is then representative differential gains $(1 - \Delta^2)$ chosen for this particular example.

Case b) Fig. 6.9a displays the frequency splitting between two consecutive longitudinal modes with and without the linear birefringence $\Delta\varepsilon_{QW}$ in the QWs introduced as an adjustable parameter for a total thickness of 48 nm (for six quantum wells, 8 nm each). Canceling all the birefringence $\Delta\varepsilon_{QW} = 0$, the frequency splitting between longitudinal

	Sample 1	Sample 2
Δf_b	-16.5 MHz	$+69 \text{ MHz}$
$\Delta\varepsilon_{s,1,2} (\Delta = 0.95)$	$+0.0152$	-0.0245
$\Delta\varepsilon_s (\Delta = 0.82)$	$+0.02$	

Table 6.1: Measured polarization modes beat frequency Δf_b [70], extracted anisotropic parameters $\Delta\varepsilon_{s,1,2}$ for experimentally obtained $\Delta = \Delta_1 = \Delta_2 = 0.95$, and anisotropic parameters $\Delta\varepsilon_s = \Delta\varepsilon_{s,1} = \Delta\varepsilon_{s,2} = (\varepsilon_{x'x'} - \varepsilon_{y'y'})/2$ together with $\Delta = 0.82$.

modes $\Delta f = 19.2 \text{ GHz}$ matches pretty well the value $\Delta f = c/(2t_{air}) = 20 \text{ GHz}$ expected from the calculation of the phase matching in a simple air external cavity of thickness t_{air} . The long extension of the air cavity compared to the semiconductor part makes it so that the optical phase develops preferentially in that region.

Fig. 6.9b) shows the details of the two transverse modes from the ones calculated in Fig. 6.9a). One note that switching off any inter-QWs amplification processes (by switching off the off-diagonal elements \mathbf{T}_{du} and \mathbf{T}_{ud}) leads to a certain inaccuracy of the mode splitting Δf in the MHz range for 1/2 cavity VCSELS. Switching on \mathbf{T}_{du} and \mathbf{T}_{ud} off-diagonal components appears then mandatory for a correct determination of the layer-selected anisotropic optical constant Δn (permittivity tensor $\Delta\varepsilon$).

Case c) We now proceed to the investigation of eigenmodes including linear gain anisotropy as relaxed parameters with phase-amplitude correlation (Henry's factor $\alpha = 3$). We do not consider any other linear birefringence $\Delta\varepsilon_{QW}$ than the phase-amplitude coupling. This section refers to the recent work of Seghilani [70] giving opposite sign of the frequency splitting $\Delta f = -16.5 \text{ MHz}$ and $\Delta f = +69 \text{ MHz}$ for S1 and S2. Here, Δf is counted positive when $f_{[110]} > f_{[1\bar{1}0]}$ according to our convention. The two-dimensional maps presented in Figs. 6.10a) (S1 sample) and Fig. 6.10b) (S2 sample) display the particular dependence of the frequency splitting, Δf , between the two orthogonal linear polarizations for the two 1/2-VCSELS vs the gain anisotropy parameter Δ and an additional surface linear birefringence ($\Delta\varepsilon_s$) with an effective surface thickness of 50 nm. In these examples, we fix the value of $\alpha = 3$ [70]. The two linear polarizations are, respectively, found along $[110]$ and $[1\bar{1}0]$ directions with inverted frequency splitting between Samples 1 and 2. One observes separately the dependence of Δf on Δ for fixed $\Delta\varepsilon_s$ (lines from left to right) and the dependence of Δf on the linear gain anisotropy Δ on the horizontal axis. Simple linear parametrization resulting from our calculation gives a phenomenological dependence of $\Delta f[\text{MHz}]$ on $\Delta\varepsilon_s$ and Δ for both samples as:

$$\Delta f_1 [\text{MHz}] = -1220\Delta\varepsilon_{s,1} + 40(1 - \Delta_1) \quad (6.5)$$

$$\Delta f_2 [\text{MHz}] = -1700\Delta\varepsilon_{s,2} + 550(1 - \Delta_2). \quad (6.6)$$

The sensitivity of Δf_2 (S2) on the linear gain dichroism Δ_2 is more than a factor of 13 larger than that of S1. This finding describes the micro-resonance effect in the region of QWs combined with a larger carrier optical pumping due to the particularly high decay rate of the cavity. On the other hand, the birefringence at the surface, delocalized from the optical confinement region, gives about the same equivalent effect on the frequency mode splitting for the two samples. If one assumes that the two samples are characterized

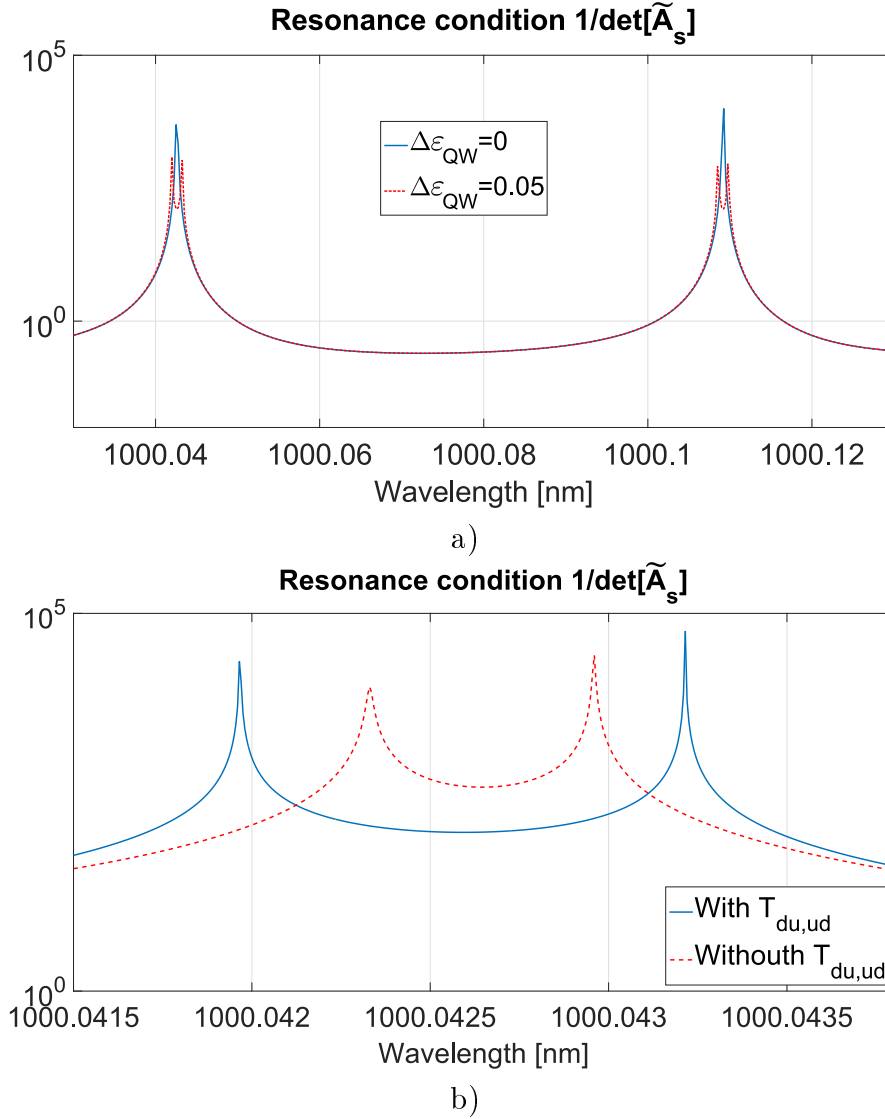


Figure 6.9: a) Calculation of multimode emission and mode splitting for $\Delta\epsilon_{QW} = 0$ (solid blue line) and $\Delta\epsilon_{QW} = 0.05$ (dashed red line with peak doublets), respectively, inside the QW of Sample 1. b) Calculation of mode splitting inside the QW of Sample 1. The solid blue curve ($\Delta f = 359$ MHz) and the dashed red curve ($\Delta f = 195$ MHz) describe the resonance conditions for models with and without off-diagonal elements \mathbf{T}_{du} and \mathbf{T}_{ud} , respectively.

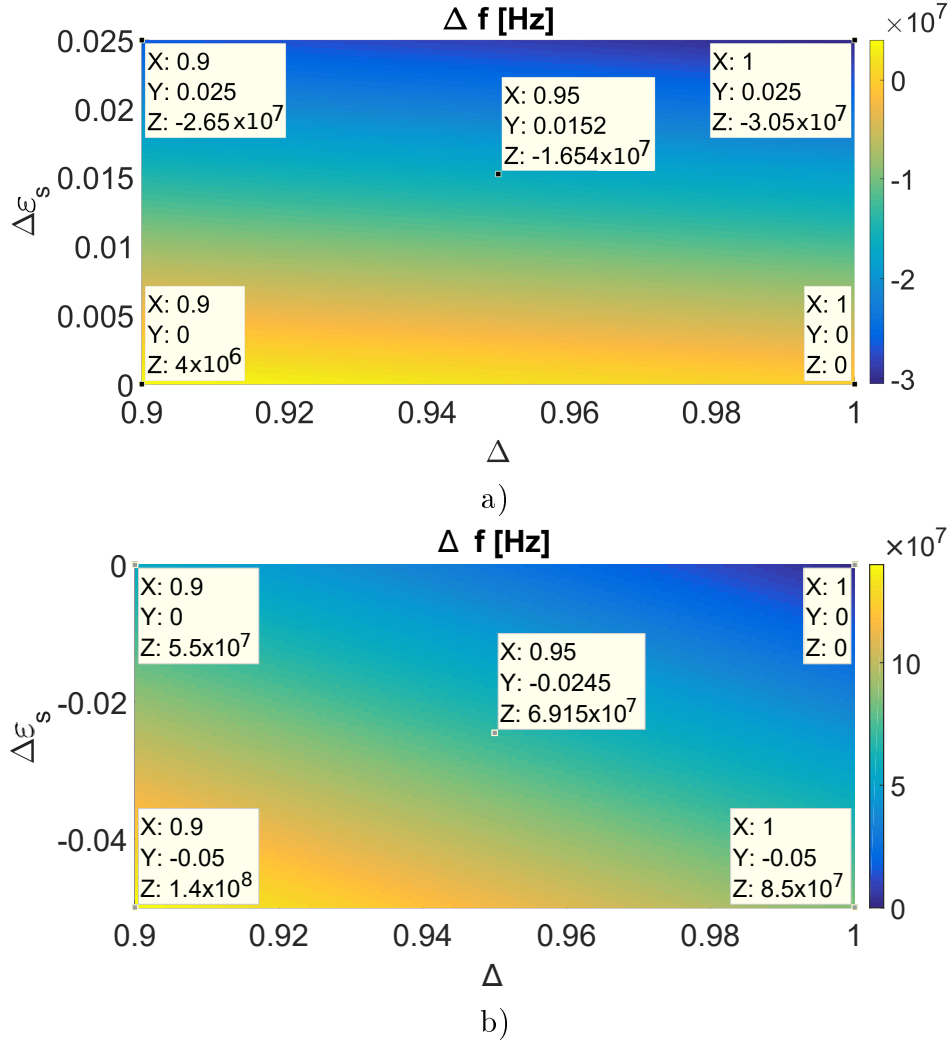


Figure 6.10: Dependence of Δf between two orthogonal linear polarizations on linear gain dichroism Δ and surface anisotropy $\Delta\epsilon_s$ of a) S1 and b) S2.

by an identical surface strain and birefringence $\Delta\epsilon_s = \Delta\epsilon_{s,1} = \Delta\epsilon_{s,2}$, and identical active zones (the same linear gain dichroism $\Delta = \Delta_1 = \Delta_2$), the common solution of the above equations gives $\Delta\epsilon_s = +0.02$ and $\Delta = 0.82$. The change of the sign of the frequency splitting between S1 and S2 may then be understood as 1) an opposite effect of the linear birefringence between surface and active layers together with 2) a main contribution from the surface for S1 due to small optical losses and gain, and small optical confinement, and 3) an enhanced contribution of linear birefringence of QWs for S2 due to larger optical losses and gain together with a strong optical confinement.

The matching of the frequency splitting to the experimental situation under the assumption of the same linear gain dichroism of $\Delta = 0.95$ (linear gain dichroism of 10% on the intensity) for samples S1 and S2, gives a surface strain birefringence $\Delta\epsilon_{s,1}$ of opposite sign of the order of $+0.015$ for S1 and $\Delta\epsilon_{s,2} = -0.025$ for S2. QW gain dichroism of about

10–30 % has been measured in Refs. [70, 135]. On the other hand, a surface birefringence difference with opposite sign between S1 and S2 would be surprising from a technological and physical point of view.

6.3 Case of the circular pumps with local linear anisotropies

In this section, we will focus on a case with spin-injected current. The calculation procedure is following: i) calculation of the resonance condition given by maximum of $1/\det[\mathbf{A}_s]$ by varying the wavelength λ and modal gain per QW g_{00} for each value of surface anisotropy $\Delta\varepsilon_s$ (or linear gain dichroism Δ) and the spin-injection degree \mathcal{P}_s . ii) Calculation of eigenvectors of \mathbf{A}_s in resonance for each value of surface anisotropy $\Delta\varepsilon_s$ and the spin-injection degree \mathcal{P}_s . iii) We will draw the calculated Stokes vector components of the output polarization for three different cases: cases with surface anisotropy without and with phase-amplitude coupling, and case with the linear gain dichroism.

6.3.1 Effect of surface strain and polarization degree spin-injected current

First of all we apply the derived formalism to calculate the dependence of the output polarization state on the spin-injection degree \mathcal{P}_s of the electrons in the conduction band of QWs and the surface strain $\Delta\varepsilon_s = (\varepsilon_{xx} - \varepsilon_{yy})/2$. This corresponds to the situation of a more simpler model described in the beginning of Chapter 5 and published by Alouini [44] (see Fig. 5.2). Figure 6.11 shows the calculated Stokes vector components of two eigenmodes (with subscripts a and b) as a function of the spin-injection degree \mathcal{P}_s and the surface strain $\Delta\varepsilon_s$. One can observe three main regions:

- i) A region with pure circularly-polarized emission $S_{3a} = -1$ and $S_{3b} = 1$. This emission is ensured by considering no linear anisotropy at surface $\Delta\varepsilon_s$ for every value of the spin-injection $|\mathcal{P}_s| > 0$. Moreover, one can see that even for small value of surface anisotropy $\Delta\varepsilon_s$, the emitted light is circularly polarized for a high degree of spin-injection \mathcal{P}_s .
- ii) A region with decreasing degree of circularly-polarized emission with $0 < |S_{3a}| < 1$ and $0 < |S_{3b}| < 1$. This effect is caused by the surface anisotropy $\Delta\varepsilon_s$, which cancels emission of circular polarization and leads to an emission of elliptically polarized light.
- iii) Region with no circular polarization $S_{3a} = 0$ and $S_{3b} = 0$. It can be seen that even high degree of spin-injection $|\mathcal{P}_s| \rightarrow 1$ is not sufficient to force the emission of circularly polarized light when the strong linear anisotropy at surface $\Delta\varepsilon_s$ is present. In that case, both linear polarization are rotated to the direction of -45 degree from birefringence axis leading to $S_{2a} = -1$ and $S_{2b} = -1$. These regions are schematically shown in Fig. 6.12b). The frequency splitting between two eigenmodes is shown in Figure 6.12. In the region with linear eigen polarizations, both modes oscillate with different frequencies. On the other hand, circularly polarized eigenmodes are fully degenerated and oscillate with the same frequency. As can be seen in Fig. 6.11, for real value of surface anisotropy extracted in this thesis $\Delta\varepsilon_s \approx 0.02$, one would need the spin polarization $\mathcal{P}_s > 0.2$ to obtain the elliptically and circularly-polarized eigenmodes. Note that if we would consider $\Delta\varepsilon_s = (\varepsilon_{x'x'} - \varepsilon_{y'y'})/2$, the component S_1 turn to component S_2 and *vice versa*.

We will now turn on the phase-amplitude coupling term α , which originates from the difference of the gain between the two modes for the same population inversion, while n_+ and n_- constitutes a unique reservoir for the two modes. In the case with spin-pumping, n_+ mainly concerns one circular mode and n_- mainly the second one and then the two gains are less correlated. For that reason, we will consider $\alpha = 1.5$ in comparison to $\alpha = 3$ considered in the case with no spin-polarized pump. Figure 6.13 displays the calculated Stokes vector components. One can observe same three regions as in the previous case. However, with nonzero α the transition between linear and circular modes are more rapid and rotation of the linear modes to -45 degree from birefringence axis is more suppressed (see S_{2a} and S_{2b} components). Figure 6.14 also displays the frequency splitting between two modes. In comparison to the case with $\alpha = 0$ (Figure 6.12) one can observe non-degeneracy in frequency also between circular (or elliptical) modes, which due to the phase-amplitude coupling oscillate with different frequencies.

6.3.2 Effect of linear gain dichroism and polarization degree spin-injected current

We will now apply the formalism derived in Chapter 5 and include all material characteristics and cavity properties of real Sample S2 including the linear gain anisotropy Δ . Figure 6.15 shows dependence of the Stokes vector components on the linear gain dichroism Δ and the spin polarization \mathcal{P}_s . One can see observe three main regions:

- i) Region of pure circularly-polarized emission $S_3 = \pm 1$. This emission is ensured by no linear gain dichroism $\Delta = 1$ for every value of the spin-injection $|\mathcal{P}_s| > 0$. Moreover, one can see that even for small linear gain dichroism $\Delta \approx 1$, the emitted light is circularly polarized for high degree of spin-injection \mathcal{P}_s . For real value of the linear gain dichroism $\Delta = 0.95$, one would need the spin polarization $|\mathcal{P}_s| > 0.15$ to obtain the elliptically and circularly-polarized eigenmodes.
- ii) Region with decreasing degree of circularly-polarized emission $0 < |S_3| < 1$. This effect is caused by the linear gain dichroism Δ , which cancels emission of circular polarization and leads to an emission of elliptically-polarized light.
- iii) Region of no circular polarization $S_3 = 0$. It can be seen that even high degree of spin-injection $|\mathcal{P}_s| \rightarrow 1$ is not sufficient for emission of circularly polarized light when strong linear gain dichroism is present. In that case the circularly-polarized eigenmodes change to the linearly polarized modes with polarization along x' and y' axis ($[110]$ and $[\bar{1}\bar{1}0]$) respectively. Note, that for pure isotropic case ($\Delta = 1$ and $\mathcal{P}_s = 0$) $S_1 = \pm 1$. That means, that numerical solution gives two linear modes oscillating along x and y axis. However, in isotropic case all directions are equivalent. For general case ($\Delta \neq 1$ and $\mathcal{P}_s \neq 0$), $S_1 = 0$.

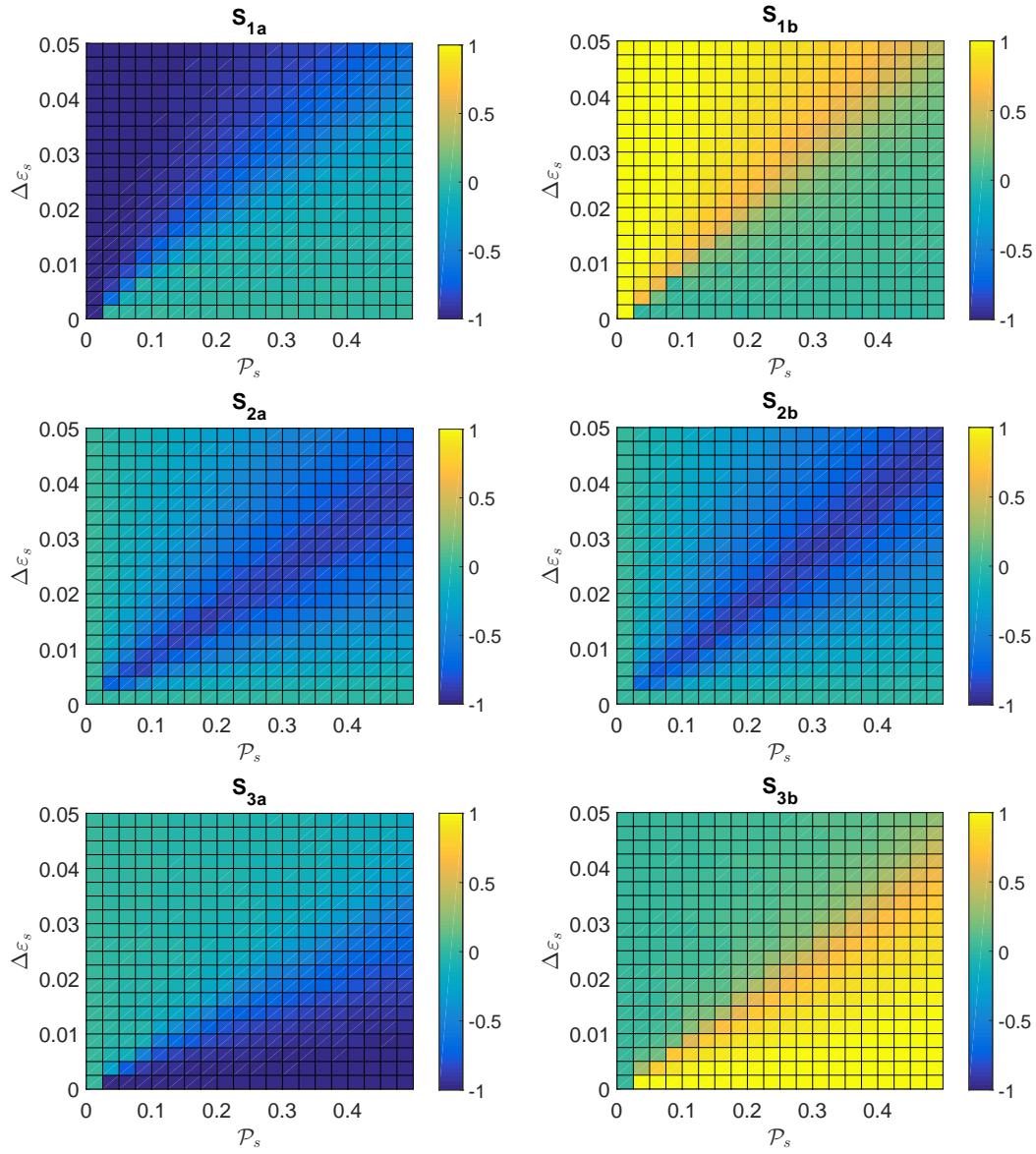


Figure 6.11: Dependence of the Stokes vector components of two eigenmodes (with subscripts a and b) on the spin polarization \mathcal{P}_s and surface anisotropy $\Delta\epsilon_s$ for $\alpha = 0$.

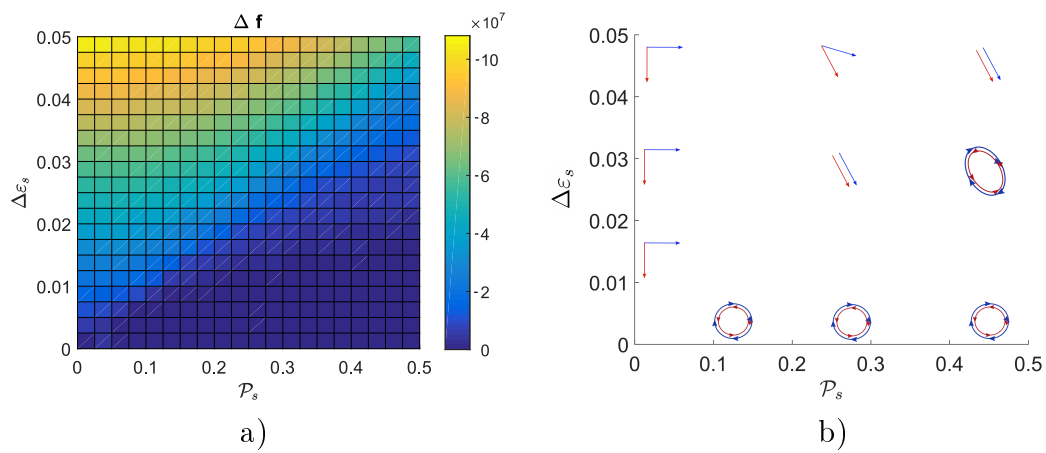


Figure 6.12: a) Dependence of the frequency shift Δf on the the spin polarization \mathcal{P}_s and surface anisotropy $\Delta \varepsilon_s$ for $\alpha = 0$. In the region with linear eigen polarizations, both modes oscillate with different frequencies. On the other hand, circularly polarized eigenmodes are fully degenerated and oscillate with the same frequency. b) Scheme of the evolution of the output polarization state.

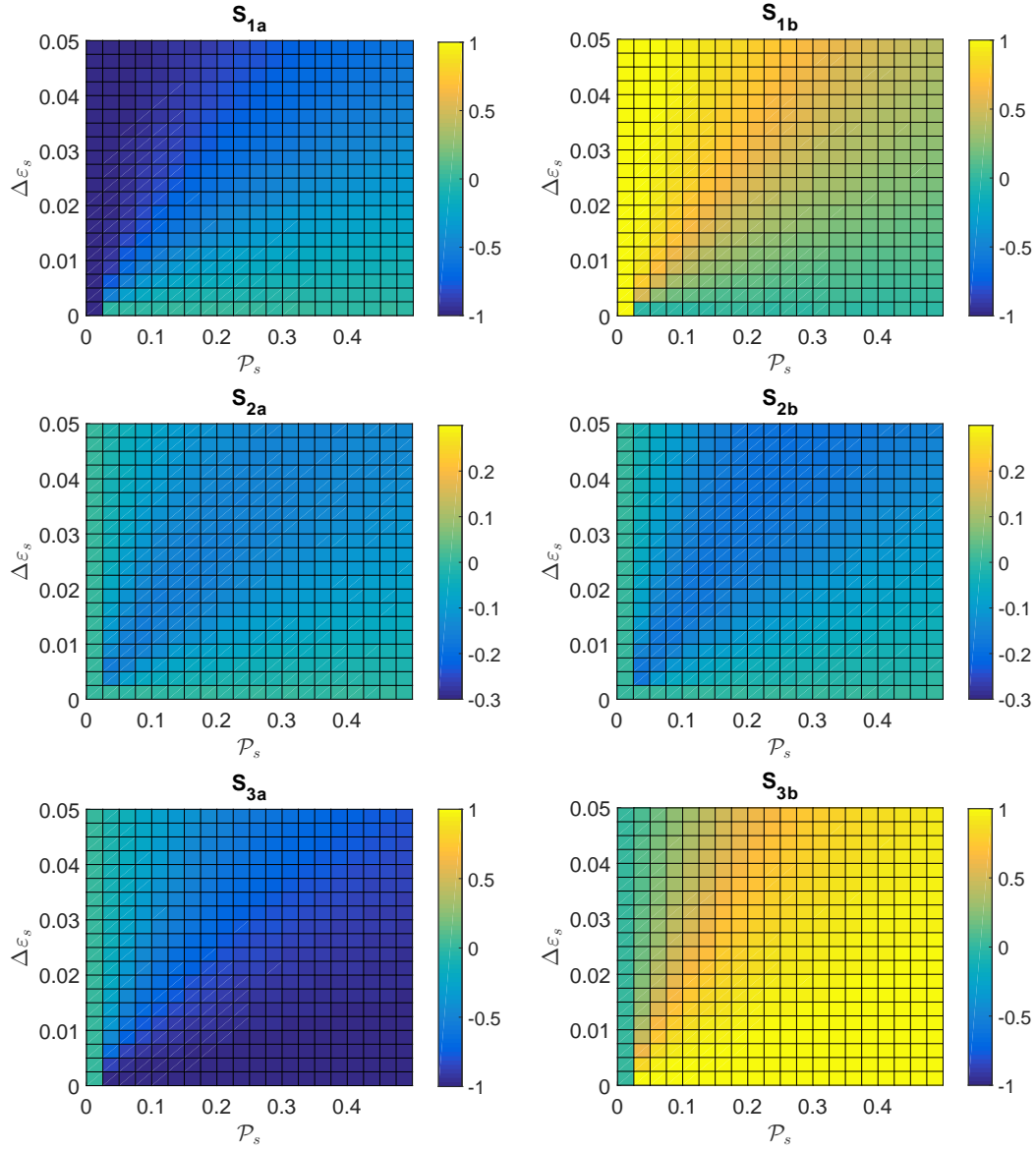


Figure 6.13: Dependence of the Stokes vector components and the spin polarization \mathcal{P}_s and surface anisotropy $\Delta\epsilon_s$ for $\alpha = 1.5$.

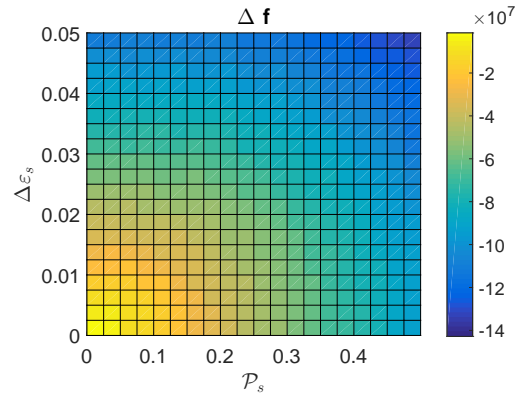


Figure 6.14: Dependence of the frequency shift Δf on the the spin polarization \mathcal{P}_s and surface anisotropy $\Delta\varepsilon_s$ for $\alpha = 1.5$.

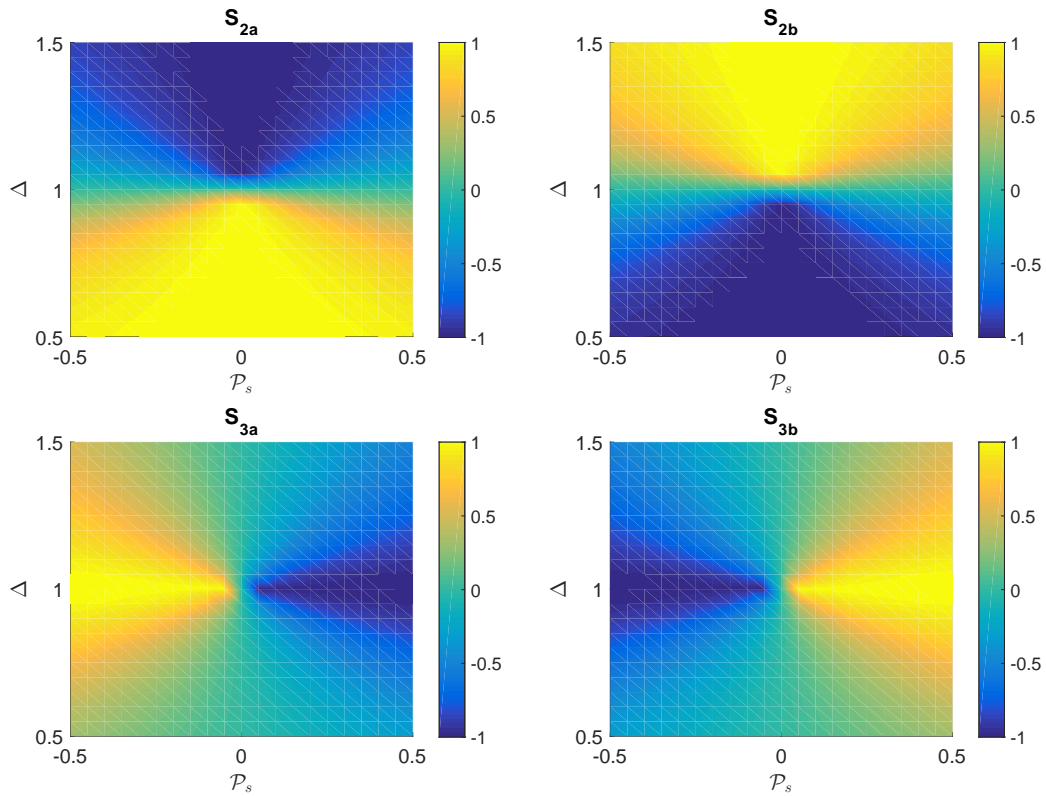


Figure 6.15: Dependence of the Stokes vector components on the linear gain dichroism Δ and the spin polarization \mathcal{P}_s .

Overall conclusion and perspectives

Conclusion

Objective of this thesis is the theoretical and experimental study of spin-polarized lasers and light-emitting diodes such as (spin-)VCSELs and spin-LEDs with the local anisotropies. Achieved results can be summarized as follows:

1. Experimental study of in-plane local anisotropy using the Mueller matrix ellipsometry at multiple angles of incidence and in-plane azimuthal angles. In combination with proper parametrization of optical functions, the optical permittivity tensors of surface strained layers and QWs have been extracted (Figs. 4.7, 4.8, and 4.9 in Sec. 4.4). The Mueller matrix ellipsometry has been presented as the useful method for study of local anisotropies in multilayer semiconductor structures such as 1/2-VCSEL dedicated for optical or electrical pumping. Results discussed in Chapter 4 have been submitted to Applied Physics Letters [43].
2. We have proposed the model which is based on two steps: (i) representation of active quantum well layers with dipole sources and (ii) modeling of light propagation in resonant multilayer structures by using an appropriate matrix approach fulfilling Maxwell equations in each layer and boundary conditions at the interfaces. Results have been published in Physical Review A [37] and in Journal of Optics [40]. Advantages of the proposed model are:
 - (i) The model describes polarization of emitted photons related to the quantum optical selection rules and consider spin polarization of injected current or generally polarized optical pumping field and effects of in-plane symmetry breaking leading to the linear gain dichroism [Eq. (5.73) in Sec. 5.2] and to the possible coupling between modes [Eq. (5.85) in Sec. 5.2].
 - (ii) Our approach describes the propagation of emitted field in general anisotropic multilayer system consisting of locally anisotropic layers affected by the symmetry reduction on the III-V semiconductor interfaces, surface reconstruction, strain and magneto-optical effects. The 4×4 matrix formalism provides effective approach for investigation of the propagation of electromagnetic radiation in anisotropic layered media, where each layer may display anisotropic optical properties and is characterized by the complex relative permittivity tensor. In the case of anisotropic layered media, the electromagnetic field in an individual layer can be expressed as a linear superposition of monochromatic plane waves with four eigenmode polarizations obtained by nontrivial solutions of wave equation in each anisotropic layer.

- (iii) The proposed model correctly defines phases of incoherent spontaneous emission (spin-LED) and coherent stimulated emission (spin-lasers). In the case of spin-LED with in the spontaneous emission regime, we improved the model of Benisty [128] by suppressing possible interference effects originating from spontaneous emission [Eq. (6.3) in Sec. 6.1].
 - (iv) Describes the complete polarization state of emitted field from laser structure and conditions for laser resonance [Eqs. (5.93)-(5.97) in Sec. 5.3.2].
 - (v) New recursive formulas derived in this thesis are used for calculation of the effective active region and enable to include the interference and reflection effects between both active regions together with amplification of multiple reflected light inside the multiple quantum wells (MQWs). Consequently, it enables to model the properties of the emission (threshold, polarization, mode splitting) from the laser with MQW active zones by searching for the resonant eigenmodes of the cavity [Eqs. (5.102)-(5.106) in Sec. 5.3.3].
3. Numerical and experimental investigation of the local anisotropies in a LED and VCSEL cavities. We started with a simple model of multilayer spin-LED structure, which includes magneto-optical spin-injector and we showed the effect of magneto-optical spin injector on a emitted polarization state (Fig. 6.2 in Sec. 6.1). Then we applied S-matrix recursive formalism for modeling of a frequency splitting and we compared with experimentally measured values in order to extract anisotropic permittivity tensors of surface layers and quantum wells of real VCSEL structures (Table 6.1 in Sec. 6.2.2). Results have been published in Physical Review A [37].
 4. Numerical simulation of the polarization states of emitted eigenmodes including local anisotropies such as linear gain dichroism and surface strain. We demonstrated the dependence of the Stokes vector components on the local anisotropies in laser structure. From these calculation, we showed the particular value of the spin-polarization \mathcal{P}_s needed to obtain the emission of circularly-polarized light from the laser structures with local anisotropies.

Perspectives

The approach derived in this thesis is suitable for future development of advanced laser modeling. In particular, we will extend the method for description of dynamical behavior of spin-VCSEL with multiple active quantum well region, including modeling of time-dependent electric field in the cavity described by the Maxwell-Bloch equations. The models of dynamical properties of spin-VCSELs are under development of pregraduate student Mariusz Drong under supervision of the author of this thesis.

One of the most perspective generalization of the approach will be done by implementing of numerical method for the calculation of laser structures with periodic media such as quantum dots, quantum wires, photonic crystals, and gratings. The Maxwell equations in a periodic grating will be solved by using rigorous coupled wave analysis (RCWA) which is based on approximation of the permittivity function and field components by their Fourier series. In this context, the layer-by-layer formalism including the scattering matrix formalism for description of emission from multiple active region, is very suitable for RCWA

implementation. This will lead to advanced model, which enables calculation of properties (threshold, polarization state of the emitted light, mode splitting) of perspective quantum-dot and quantum-wire spin-lasers. However, the model has to be further generalized to avoid spurious interferences between Fourier modes.

We also plan to extend participation on technology of laser preparation and experimental demonstration of spin-VCSELs properties. This will include pump-probe experiments with femtosecond pulse laser by using new experimental setup, which will be built soon at Technical University of Ostrava. Future work will be also focused on a searching for alternative source of (coherent) THz radiation. Main idea of the alternative THz laser is based on a photomixing of two continuous-wave laser modes of VCSEL, which are separated in frequency domain. Such frequency splitting is caused by linear anisotropies which are naturally present in semiconductor layers (interface, surface), externally induced (*e.g.* by electric field), or added to the laser cavity using birefringent optical element. The optical beatnote between two laser modes at different frequencies are then converted into an AC current oscillating at THz frequency and radiated by an appropriately designed antenna.

List of publications

Journals:

- [1] T. Fördös, K. Postava, H. Jaffrès, J. Pištora, H.-J. Drouhin, "Mueller matrix ellipsometric study of multilayer spin-VCSEL structures with local optical anisotropy", *Appl. Phys. Lett.* **112**, 221106 (2018).
- [2] T. Fördös, H. Jaffrès, K. Postava, M. Seghiali, A. Garnache, J. Pištora, H. J. Drouhin. "Eigenmodes of Spin-VECSELs with local linear birefringence and gain dichroism", *Phys. Rev. A* **96**, 043828 (2017)
- [3] T. Fördös, K. Postava, H. Jaffrès, and J. Pištora, "Matrix approach for modeling of spin-polarized light-emitting diodes and lasers", *J. Opt.* **16** (6), 065008 (2014).

Conference proceedings:

- [4] Postava, K., Fördös, T., Jaffrès, H., Halagačka, L., Drouhin, H.J., Pištora, J. Modeling of anisotropic grating structures with active dipole layers *Proc. SPIE* **9516**, 95160O, (2015).
- [5] T. Fördös, O. Životský, K. Postava, D. Hrabovský, J. Pištora, J. Lančok, M. Miglierini, M. Klementová, Ferromagnetic nanoparticulate films studied by optical and magneto-optical ellipsometry, *Journal of Physics: Conference Series* **303**, pp. 012041, (2011).
- [6] T. Fördös, K. Postava, and J. Pištora, Magneto-optical effects in nanostructures with reduced symmetry. *Proc. SPIE* **8306**, 83061F, (2011).

List of conferences

Invited:

T. Fördös; H. Jaffrès; K. Postava; J. Pištora; H. J. Drouhin; Properties of linear birefringence of InGaAs/GaAsP semiconductor spin VECSELS: From experiment to theory and models, Magnetism and Optics Research International Symposium - MORIS 2015, Penang, Malaysia (29 November - 2 December, 2015).

T. Fördös; H. Jaffrès; K. Postava; J. Pištora; A. Garnache H. J. Drouhin; Eigenmodes of semiconductor spin-lasers with local linear birefringence and gain dichroism, SPIE Spintronics X, San Diego, California USA (6 - 10 August, 2017).

T. Fördös; H. Jaffrès; K. Postava; M. Drong; J. Pištora; H. J. Drouhin; Polarization and anisotropic properties of spin-VCSELS, SPIE Spintronics XI, San Diego, California USA (19 - 23 August, 2018).

Oral presentation:

T. Fördös; H. Jaffrès; K. Postava; J. Pištora; H. J. Drouhin; Properties of light emission from multilayer InGaAs/GaAsP semiconductor spin-lasers and VECSELS, SPIE SPINTRONICS VIII, San Diego, California USA (9 - 13 August, 2015).

K. Postava; T. Fördös; H. Jaffrès; L. Halagačka; H. J. Drouhin; J. Pištora; Modeling of anisotropic grating structures with active dipole layers . Proc. SPIE 9516, Integrated Optics: Physics and Simulations II, 95160O. Prague, Czech Republic (13 - 16 April, 2015).

H. Jaffrès, T. Fördös, K. Postava, J.-M. George, J. Pištora, and H.-J. Drouhin. Properties and linear birefringences of InGaAs/GaAsP semiconductor spin-vecsel: from experiments to theory and models, The 3th workshop on VECSELS, Montpellier, France (17 - 19 November, 2015).

T. Fördös; H. Jaffrès; K. Postava; J.-M. George, J. Frougier, J. Pištora; H.-J. Drouhin; Properties of light emission from multilayer InGaAs/GaAsP spin-lasers with optical birefringence, Energy, Materials and Nanotechnology: Summer Meeting 2016, Cancún, Mexico (9 - 12 June, 2016).

T. Fördös; H. Jaffrès; K. Postava; J. Pištora; H. J. Drouhin; Mueller matrix ellipsometric study of multilayer spin-lasers structures with local optical anisotropy, Nano Ostrava 2017,

(22 - 25 May, 2017).

Appendix A

Lamb's model

In Chapter 5 we derived the coupling coefficients $\theta_{(1,2)}^\pm$ and $\beta_{(1,2)}^\pm$ for the most general case involving the spin-polarized carriers together with the linear gain dichroism as depicted in Fig 5.5. The first simple model for the coupling between two modes but without the linear gain dichroism was given by Lamb [119]. For the class-A laser with adiabatically neglected population inversion, the temporal evolution of the two circularly-polarized modes intensities ($I_{(1)} = I_+$ and $I_{(2)} = I_-$) with the respective gains G_+ and G_- can be described by two coupled differential equations:

$$\frac{\partial}{\partial t} I_+ = I_+ (G_+ - \beta_+ I_+ - \theta_\pm I_-), \quad (\text{A.1})$$

$$\frac{\partial}{\partial t} I_- = I_- (G_- - \beta_- I_- - \theta_\mp I_+), \quad (\text{A.2})$$

where β_+ and β_- are the self-saturation coefficients for the right- and left-circularly polarized modes, respectively. θ_\pm and θ_\mp are the cross-coupling coefficients. Depending on the circular gain dichroism $\Delta G = G_+ - G_-$ induced by the injected spin and on the Lamb coupling constant defined similarly to Eq. (5.85) as:

$$\mathcal{C} = \frac{\theta_\pm \theta_\mp}{\beta_+ \beta_-}. \quad (\text{A.3})$$

The laser will then oscillate on one of these eigen polarizations or on both. By using an approximation where $\beta = \beta_+ = \beta_-$, $\theta = \theta_{+-} = \theta_{-+}$, the steady-state intensities can be expressed as:

$$I_+ = \frac{G}{\beta} \frac{(1 - \sqrt{\mathcal{C}}) + \frac{\Delta G}{2G} (1 + \sqrt{\mathcal{C}})}{1 - \mathcal{C}} \quad (\text{A.4})$$

$$I_- = \frac{G}{\beta} \frac{(1 - \sqrt{\mathcal{C}}) - \frac{\Delta G}{2G} (1 + \sqrt{\mathcal{C}})}{1 - \mathcal{C}}, \quad (\text{A.5})$$

where $G = (G_+ + G_-)/2$ is the average gain. The evolution of the two eigenstate intensities are depicted in Fig. A.1 as a function of the normalized gain dichroism for four values of the constant \mathcal{C} . For no coupling ($\mathcal{C} = 0$), two eigen-modes oscillate independently and the intensities are proportional to the normalized gain dichroism. When \mathcal{C} increases, the oscillation of one mode saturates the gain of the other one leading to a limited range of

simultaneous oscillations of the two modes. For strong coupling ($\mathcal{C} = 0.9$), the range of simultaneous oscillations becomes very narrow leading to the easy switch from one eigenstates to another even for a very small normalized gain dichroism (about 10%). This has been observed in recent experiments in the case of spin 1/2 VECSEL structures [32].

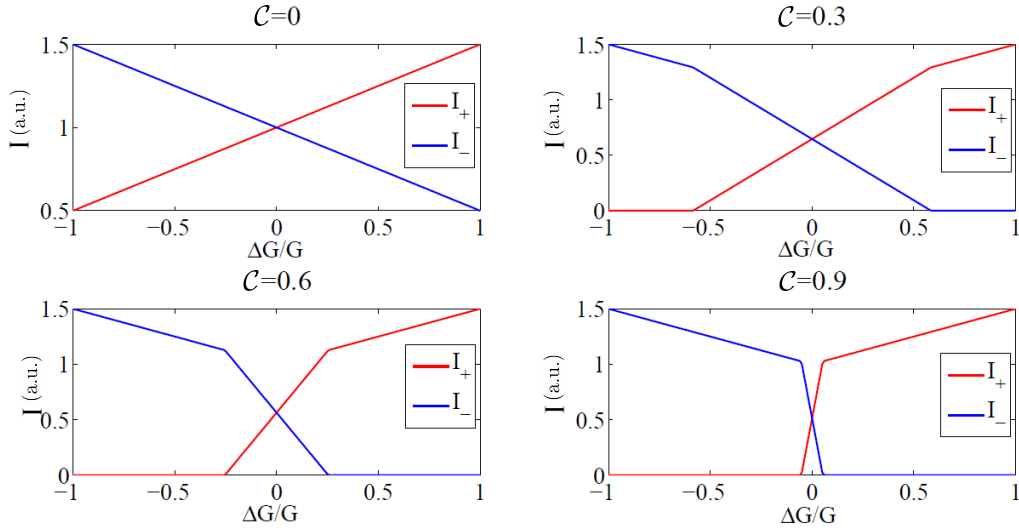


Figure A.1: The evolution of the two eigenstates intensities as a function of the normalized gain dichroism for four values of the constant \mathcal{C} : 0, 0.3, 0.6, and 0.9.

Appendix B

Transfer matrix formalism for multilayer lasers and LED

Figure 5.6 shows the modeled structure consisting of an active dipole layer surrounded by a multilayer system described by the transfer matrices $\mathbf{M}^{(1)}$ and $\mathbf{M}^{(2)}$. The matrices relate the amplitudes of the waves propagating from and toward the system

$$\begin{bmatrix} \mathbf{A}''_{\text{up}} \\ \mathbf{A}''_{\text{down}} \end{bmatrix} = \begin{bmatrix} \mathbf{M}_{\text{uu}}^{(2)} & \mathbf{M}_{\text{ud}}^{(2)} \\ \mathbf{M}_{\text{du}}^{(2)} & \mathbf{M}_{\text{dd}}^{(2)} \end{bmatrix} \begin{bmatrix} \mathbf{A}_{\text{up}}^{(N+1)} \\ \mathbf{A}_{\text{down}}^{(N+1)} \end{bmatrix}, \quad (\text{B.1})$$

$$\begin{bmatrix} \mathbf{A}_{\text{up}}^{(0)} \\ \mathbf{A}_{\text{down}}^{(0)} \end{bmatrix} = \begin{bmatrix} \mathbf{M}_{\text{uu}}^{(1)} & \mathbf{M}_{\text{ud}}^{(1)} \\ \mathbf{M}_{\text{du}}^{(1)} & \mathbf{M}_{\text{dd}}^{(1)} \end{bmatrix} \begin{bmatrix} \mathbf{A}'_{\text{up}} \\ \mathbf{A}'_{\text{down}} \end{bmatrix}, \quad (\text{B.2})$$

and from (B.2) one can obtain by matrix inversion

$$\begin{bmatrix} \mathbf{A}'_{\text{up}} \\ \mathbf{A}'_{\text{down}} \end{bmatrix} = \begin{bmatrix} \widetilde{\mathbf{M}}_{\text{uu}}^{(1)} & \widetilde{\mathbf{M}}_{\text{ud}}^{(1)} \\ \widetilde{\mathbf{M}}_{\text{du}}^{(1)} & \widetilde{\mathbf{M}}_{\text{dd}}^{(1)} \end{bmatrix} \begin{bmatrix} \mathbf{A}_{\text{up}}^{(0)} \\ \mathbf{A}_{\text{down}}^{(0)} \end{bmatrix}, \quad (\text{B.3})$$

where $\mathbf{A}^{(0)}$ and $\mathbf{A}^{(N+1)}$ describe the amplitudes in the superstrate and substrate. Similarly, \mathbf{A}' and \mathbf{A}'' are the amplitudes above and below the active dipole layer. Note that four waves propagate in each layer of the system. Therefore, the amplitudes in (B.1) and (B.2) represent the amplitude vectors corresponding to two orthogonal polarizations, for example, $\mathbf{A}_{\text{down}}^{(0)} = [A_1^{(0)}; A_3^{(0)}]^T$ and $\mathbf{A}_{\text{up}}^{(0)} = [A_2^{(0)}; A_4^{(0)}]^T$. The submatrices in (B.1) and (B.2) are 2×2 matrices and the tilde denotes the blocks of the inverse matrix $\widetilde{\mathbf{M}}^{(1)} = [\mathbf{M}^{(1)}]^{-1}$. Note that in the case of lasers the light is only emitted from the structure: $\mathbf{A}_{\text{down}}^{(0)} = \mathbf{A}_{\text{up}}^{(N+1)} = \mathbf{0}$. Equations (B.1) and (B.2) are compactly written as the 4×4 matrix equations (1) and (2) from Ref. [40].

From (B.1), (B.2), and (5.86) we obtain a compact form of the basic equation (5.93) for the field emitted from the structure, which is used to calculate the amplitudes of the field emitted from the structure $\mathbf{A}_{\text{up}}^{(0)}$ and $\mathbf{A}_{\text{down}}^{(N+1)}$ from the dipole source vectors \mathbf{A}_{up}^d and $\mathbf{A}_{\text{down}}^d$. Equations (5.88), (5.90), and (5.93) are the compactly written 4×4 matrix equations (8)-(10) in Ref. 40.

Appendix C

Scattering matrix formalism for multilayer lasers and LED

While the transfer matrix \mathbf{M} described by Eqs. (B.1) and (B.2) relates the upper and lower field amplitudes, the scattering matrix (S-matrix) is defined using the amplitudes of the waves incoming toward and outgoing from the structure. Let us consider a similar structure shown in Fig. D.1, in which the active dipole layer is surrounded by the multilayer subsystems described using the scattering matrices $\mathbf{S}^{(1)}$ and $\mathbf{S}^{(2)}$. The amplitudes of the waves are related using the matrix formulas

$$\begin{bmatrix} \mathbf{A}_{\text{up}}^{(0)} \\ \mathbf{A}'_{\text{down}} \end{bmatrix} = \begin{bmatrix} \mathbf{S}_{\text{uu}}^{(1)} & \mathbf{S}_{\text{ud}}^{(1)} \\ \mathbf{S}_{\text{du}}^{(1)} & \mathbf{S}_{\text{dd}}^{(1)} \end{bmatrix} \begin{bmatrix} \mathbf{A}'_{\text{up}} \\ \mathbf{A}_{\text{down}}^{(0)} \end{bmatrix} = \mathbf{S}^{(1)} \begin{bmatrix} \mathbf{A}'_{\text{up}} \\ \mathbf{A}_{\text{down}}^{(0)} \end{bmatrix} \quad (\text{C.1})$$

and

$$\begin{bmatrix} \mathbf{A}_{\text{up}}'' \\ \mathbf{A}_{\text{down}}^{(N+1)} \end{bmatrix} = \begin{bmatrix} \mathbf{S}_{\text{uu}}^{(2)} & \mathbf{S}_{\text{ud}}^{(2)} \\ \mathbf{S}_{\text{du}}^{(2)} & \mathbf{S}_{\text{dd}}^{(2)} \end{bmatrix} \begin{bmatrix} \mathbf{A}_{\text{up}}^{(N+1)} \\ \mathbf{A}_{\text{down}}'' \end{bmatrix} = \mathbf{S}^{(2)} \begin{bmatrix} \mathbf{A}_{\text{up}}^{(N+1)} \\ \mathbf{A}_{\text{down}}'' \end{bmatrix}. \quad (\text{C.2})$$

If we expect that light is only emitted from the structure then $\mathbf{A}_{\text{down}}^{(0)} = \mathbf{A}_{\text{up}}^{(N+1)} = \mathbf{0}$. From (C.1), (C.2), and (5.86) we obtain the basic equation (5.93) for the field emitted from the structure with the matrix $\tilde{\mathbf{A}}_{\text{S}}$ in Eq. (5.97) which consists of a more general expression suitable for the recurrent calculation.

Appendix D

Recursive calculation of the effective gain tensor

The S-matrix approach enables us to describe optical amplification, propagation, as well as interferences in multiple QW structure. The recursive S-matrix method we propose here provides a numerical solution scheme to describe any type of multilayered structures. Fig. D.1 schematically shows the structure including two active dipole layers, respectively, (n) and $(n+1)$, the latter being the new one to add by recursion. The composite of the two can be substituted by a single effective active dipole layer described on its own by a single effective matrix $\mathbf{T}^{(n,n+1)}$ and single effective dipole vector $\mathbf{A}^{(n,n+1)d}$ according to the following description.

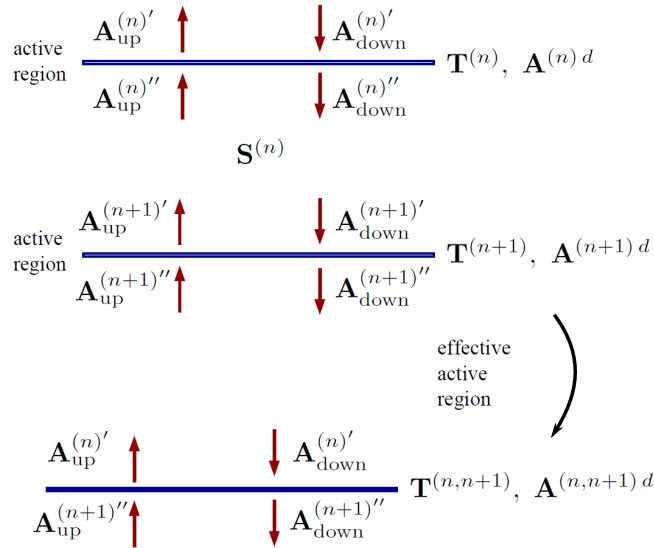


Figure D.1: Schematic description of the application of the recursive formula.

Let us consider that the dipole active layers are described by the dipole source vectors $\mathbf{A}^{(n)d}$ and $\mathbf{A}^{(n+1)d}$ and the optical gain tensor $\mathbf{T}^{(n)}$ and $\mathbf{T}^{(n+1)}$. The definitions of vectors and optical gain are similar to (5.86). The effective dipole layer is found by us-

ing Eqs. (5.102) and (5.103), where the effective dipole source vector $\mathbf{A}^{(n,n+1)d}$ and the effective optical gain tensor $\mathbf{T}^{(n,n+1)}$ appear in the most general case in the following form:

$$\mathbf{T}^{(n,n+1)} = \begin{bmatrix} \mathbf{0} & \mathbf{T}_{ud}^{(n)} \\ \mathbf{T}_{du}^{(n+1)} & \mathbf{0} \end{bmatrix} + \mathbf{B} \begin{bmatrix} \mathbf{T}_{uu}^{(n+1)} & \mathbf{0} \\ \mathbf{0} & \mathbf{T}_{dd}^{(n)} \end{bmatrix}, \quad (\text{D.1})$$

$$\mathbf{A}^{(n,n+1)d} = \mathbf{A}^{(n)d} + \mathbf{B} \mathbf{A}^{(n+1)d}, \quad (\text{D.2})$$

where

$$\mathbf{B} = \begin{bmatrix} \mathbf{T}_{uu}^{(n)} \mathbf{S}_{uu}^{(n)} & \mathbf{T}_{uu}^{(n)} \mathbf{S}_{ud}^{(n)} \\ \mathbf{T}_{dd}^{(n+1)} \mathbf{S}_{du}^{(n)} & \mathbf{T}_{dd}^{(n+1)} \mathbf{S}_{dd}^{(n)} \end{bmatrix} \begin{bmatrix} \mathbf{I} - \mathbf{T}_{ud}^{(n+1)} \mathbf{S}_{du}^{(n)} & -\mathbf{T}_{ud}^{(n+1)} \mathbf{S}_{dd}^{(n)} \\ -\mathbf{T}_{du}^{(n)} \mathbf{S}_{uu}^{(n)} & \mathbf{I} - \mathbf{T}_{du}^{(n)} \mathbf{S}_{ud}^{(n)} \end{bmatrix}^{-1}. \quad (\text{D.3})$$

The effective \mathbf{T} matrix consists of non-zero off-diagonal sub-matrices \mathbf{T}_{ud} and \mathbf{T}_{du} , originating from the interference and reflection processes between consecutive active regions.

Note that the single active layer ($n+1$) added in the recursion procedure does not admit any off-diagonal component $\mathbf{T}_{ud}^{(n+1)} = \mathbf{0}$ and $\mathbf{T}_{du}^{(n+1)} = \mathbf{0}$ because of no internal multiple reflections. Let us demonstrate the recursive calculation for the case of three dipolar layers ($\tilde{n} = 1, 2, 3$) described by the block-diagonal matrix

$$\mathbf{T}^{(\tilde{n})} = \begin{bmatrix} \mathbf{T}_{uu}^{(\tilde{n})} & \mathbf{0} \\ \mathbf{0} & \mathbf{T}_{dd}^{(\tilde{n})} \end{bmatrix}, \quad (\text{D.4})$$

while the optical interactions between first and second, and second and third, dipole layers are characterized by the scattering matrices $\mathbf{S}^{(1)}$ and $\mathbf{S}^{(2)}$, respectively. In the *first step* we calculate the effective dipole layer for the first two active regions, $n=1$: $\mathbf{T}^{(n,n+1)} = \mathbf{T}^{(1,2)}$. According to Eqs. (D.1)-(D.3), the recursion formula gives for the gain tensor components:

$$\mathbf{T}_{uu}^{(n,n+1)} = \mathbf{T}_{uu}^{(1,2)} = \mathbf{T}_{uu}^{(1)} \mathbf{S}_{uu}^{(1)} \mathbf{T}_{uu}^{(2)} \quad (\text{D.5})$$

$$\mathbf{T}_{ud}^{(n,n+1)} = \mathbf{T}_{ud}^{(1,2)} = \mathbf{T}_{uu}^{(1)} \mathbf{S}_{ud}^{(1)} \mathbf{T}_{dd}^{(1)} \quad (\text{D.6})$$

$$\mathbf{T}_{du}^{(n,n+1)} = \mathbf{T}_{du}^{(1,2)} = \mathbf{T}_{dd}^{(2)} \mathbf{S}_{dd}^{(1)} \mathbf{T}_{uu}^{(2)} + \mathbf{T}_{dd}^{(2)} \mathbf{S}_{du}^{(1)} \quad (\text{D.7})$$

$$\mathbf{T}_{dd}^{(n,n+1)} = \mathbf{T}_{dd}^{(1,2)} = \mathbf{T}_{dd}^{(2)} \mathbf{S}_{dd}^{(1)} \mathbf{T}_{dd}^{(1)}, \quad (\text{D.8})$$

where new off-diagonal components $\mathbf{T}_{ud,du}^{(1,2)}$ describe coherent multiple reflections and interference effects between active regions (1) and (2). In the *second step* of the numerical procedure, we set $\mathbf{T}^{(2)} \equiv \mathbf{T}^{(1,2)}$ followed by *third step*, when we calculate the complete

effective gain tensor for $n = 2$: $\mathbf{T} = \mathbf{T}^{(2,3)}$ according to

$$\mathbf{T}_{uu}^{(2,3)} = \mathbf{T}_{uu}^{(2)} \frac{1}{\mathbf{I} - \mathbf{S}_{ud}^{(2)} \mathbf{T}_{du}^{(2)}} \mathbf{S}_{uu}^{(2)} \mathbf{T}_{uu}^{(3)} \quad (\text{D.9})$$

$$\mathbf{T}_{ud}^{(2,3)} = \mathbf{T}_{ud}^{(2)} + \mathbf{T}_{uu}^{(2)} \mathbf{S}_{ud}^{(2)} \frac{1}{\mathbf{I} - \mathbf{T}_{du}^{(2)} \mathbf{S}_{ud}^{(2)}} \mathbf{T}_{dd}^{(2)} \quad (\text{D.10})$$

$$\begin{aligned} \mathbf{T}_{du}^{(2,3)} &= \mathbf{T}_{dd}^{(3)} \mathbf{S}_{dd}^{(2)} \frac{1}{\mathbf{I} - \mathbf{T}_{du}^{(2)} \mathbf{S}_{ud}^{(2)} \mathbf{T}_{du}^{(2)} \mathbf{S}_{uu}^{(2)}} \mathbf{T}_{uu}^{(3)} \\ &\quad + \mathbf{T}_{dd}^{(3)} \mathbf{S}_{du}^{(2)} \end{aligned} \quad (\text{D.11})$$

$$\mathbf{T}_{dd}^{(2,3)} = \mathbf{T}_{dd}^{(3)} \mathbf{S}_{dd}^{(2)} \frac{1}{\mathbf{I} - \mathbf{T}_{du}^{(2)} \mathbf{S}_{ud}^{(2)}} \mathbf{T}_{dd}^{(2)}. \quad (\text{D.12})$$

The present recursive approach can be applied for an arbitrary number of active source layers and arbitrary structures. It can be thus applied for the calculation of the effective gain tensor of any complex light-emitting multilayer structures such as VCSELs and spin-VCSELs.

Bibliography

- ¹M. N. Baibich, J. M. Broto, A. Fert, F. N. Van Dau, F. Petroff, P. Etienne, G. Creuzet, A. Friederich, and J. Chazelas, “Giant magnetoresistance of (001)Fe/(001)Cr magnetic superlattices”, *Phys. Rev. Lett.* **61**, 2472–2475 (1988).
- ²G. Binasch, P. Grünberg, F. Saurenbach, and W. Zinn, “Enhanced magnetoresistance in layered magnetic structures with antiferromagnetic interlayer exchange”, *Phys. Rev. B* **39**, 4828–4830 (1989).
- ³F. Meier and B. Zakharchenia, *Optical orientation*, Modern problems in condensed matter sciences (North-Holland, 1984).
- ⁴R. Fiederling, M. Keim, G. Reuscher, W. Ossau, G. Schmidt, A. Waag, and L. W. Molenkamp, “Injection and detection of a spin-polarized current in a light-emitting diode”, *Nature* **402**, 787–790 (1999).
- ⁵H. J. Zhu, M. Ramsteiner, H. Kostial, M. Wassermeier, H.-P. Schönherr, and K. H. Ploog, “Room-temperature spin injection from Fe into GaAs”, *Phys. Rev. Lett.* **87**, 016601 (2001).
- ⁶C. Adelman, X. Lou, J. Strand, C. J. Palmstrøm, and P. A. Crowell, “Spin injection and relaxation in ferromagnet-semiconductor heterostructures”, *Phys. Rev. B* **71**, 121301 (2005).
- ⁷X. Jiang, R. Wang, R. M. Shelby, R. M. Macfarlane, S. R. Bank, J. S. Harris, and S. S. P. Parkin, “Highly spin-polarized room-temperature tunnel injector for semiconductor spintronics using MgO(100)”, *Phys. Rev. Lett.* **94**, 056601 (2005).
- ⁸Y. Lu, V. G. Truong, P. Renucci, M. Tran, H. Jaffres, C. Deranlot, J. M. George, A. Lemaitre, Y. Zheng, D. Demaille, P.-H. Binh, T. Amand, and X. Marie, “MgO thickness dependence of spin injection efficiency in spin-light emitting diodes”, *Appl. Phys. Lett.* **93**, 152102–152102–3 (2008).
- ⁹S. Hovel, N. C. Gerhardt, M. R. Hofmann, F.-Y. Lo, A. Ludwig, D. Reuter, A. D. Wieck, E. Schuster, H. Wende, W. Keune, O. Petravic, and K. Westerholt, “Room temperature electrical spin injection in remanence”, *Appl. Phys. Lett.* **93**, 021117, – (2008).
- ¹⁰V. G. Truong, P.-H. Binh, P. Renucci, M. Tran, Y. Lu, H. Jaffres, J. M. George, C. Deranlot, A. Lemaitre, T. Amand, and X. Marie, “High speed pulsed electrical spin injection in spin-light emitting diode”, *Appl. Phys. Lett.* **94**, 141109–141109–3 (2009).

- ¹¹J. Zarpellon, H. Jaffrès, J. Frougier, C. Deranlot, J. M. George, D. H. Mosca, F. Freimuth, Q. H. Duong, P. Renucci, and X. Marie, “Spin injection at remanence into III-V spin light-emitting diodes using (Co/Pt) ferromagnetic injectors”, *Phys. Rev. B* **86**, 205314 (2012).
- ¹²A. Fert and H. Jaffrès, “Conditions for efficient spin injection from a ferromagnetic metal into a semiconductor”, *Phys. Rev. B* **64**, 184420 (2001).
- ¹³E. I. Rashba, “Theory of electrical spin injection: tunnel contacts as a solution of the conductivity mismatch problem”, *Phys. Rev. B* **62**, R16267–R16270 (2000).
- ¹⁴G. Schmidt, D. Ferrand, L. W. Molenkamp, A. T. Filip, and B. J. van Wees, “Fundamental obstacle for electrical spin injection from a ferromagnetic metal into a diffusive semiconductor”, *Phys. Rev. B* **62**, R4790–R4793 (2000).
- ¹⁵A. T. Hanbicki, O. M. J. van Erve, R. Magno, G. Kioseoglou, C. H. Li, B. T. Jonker, G. Itskos, R. Mallory, M. Yasar, and A. Petrou, “Analysis of the transport process providing spin injection through an Fe/AlGaAs schottky barrier”, *Appl. Phys. Lett.* **82**, 4092–4094 (2003).
- ¹⁶S. H. Liang, T. T. Zhang, P. Barate, J. Frougier, M. Vidal, P. Renucci, B. Xu, H. Jaffrès, J.-M. George, X. Devaux, M. Hehn, X. Marie, S. Mangin, H. X. Yang, A. Hallal, M. Chshiev, T. Amand, H. F. Liu, D. P. Liu, X. F. Han, Z. G. Wang, and Y. Lu, “Large and robust electrical spin injection into GaAs at zero magnetic field using an ultrathin CoFeB/MgO injector”, *Phys. Rev. B* **90**, 085310 (2014).
- ¹⁷M. Holub and P. Bhattacharya, “Spin-polarized light-emitting diodes and lasers”, *J. Phys. D: Appl. Phys.* **40**, R179 (2007).
- ¹⁸J. Sinova and I. Zutic, “New moves of the spintronics tango”, *Nature Materials* **11**, 368–371 (2012).
- ¹⁹D. Basu, D. Saha, C. C. Wu, M. Holub, Z. Mi, and P. Bhattacharya, “Electrically injected InAs/GaAs quantum dot spin laser operating at 200K”, *Appl. Phys. Lett.* **92**, 091119 (2008).
- ²⁰D. Basu, D. Saha, and P. Bhattacharya, “Optical polarization modulation and gain anisotropy in an electrically injected spin laser”, *Phys. Rev. Lett.* **102**, 093904 (2009).
- ²¹H. Dery, Y. Song, P. Li, and I. Zutic, “Silicon spin communication”, *Appl. Phys. Lett.* **99**, 082502 (2011).
- ²²N. C. Gerhardt, M. Y. Li, H. Jähme, H. Höpfner, T. Ackemann, and M. R. Hofmann, “Ultrafast spin-induced polarization oscillations with tunable lifetime in vertical-cavity surface-emitting lasers”, *Appl. Phys. Lett.* **99**, 151107 (2011).
- ²³S. Hallstein, J. D. Berger, M. Hilpert, H. C. Schneider, W. W. Rühle, F. Jahnke, S. W. Koch, H. M. Gibbs, G. Khitrova, and M. Oestreich, “Manifestation of coherent spin precession in stimulated semiconductor emission dynamics”, *Phys. Rev. B* **56**, R7076–R7079 (1997).

- ²⁴H. Ando, T. Sogawa, and H. Gotoh, “Photon-spin controlled lasing oscillation in surface-emitting lasers”, *Appl. Phys. Lett.* **73**, 566–568 (1998).
- ²⁵M. Holub, J. Shin, D. Saha, and P. Bhattacharya, “Electrical spin injection and threshold reduction in a semiconductor laser”, *Phys. Rev. Lett.* **98**, 146603 (2007).
- ²⁶J. Rudolph, S. Döhrmann, D. Hägele, M. Oestreich, and W. Stolz, “Room-temperature threshold reduction in vertical-cavity surface-emitting lasers by injection of spin-polarized electrons”, *Appl. Phys. Lett.* **87**, 241117 (2005).
- ²⁷M. Holub and B. T. Jonker, “Threshold current reduction in spin-polarized lasers: role of strain and valence-band mixing”, *Phys. Rev. B* **83**, 125309 (2011).
- ²⁸N. Li, D. Alexandropoulos, H. Susanto, I. Henning, and M. Adams, “Stability analysis of quantum-dot spin-VCSELs”, *Electronics* **5**, 83 (2016).
- ²⁹N. Gerhardt, S. Hovel, M. Hofmann, J. Yang, D. Reuter, and A. Wieck, “Enhancement of spin information with vertical cavity surface emitting lasers”, *Electron. Lett.* **42**, 88–89 (2006).
- ³⁰S. Iba, S. Koh, K. Ikeda, and H. Kawaguchi, “Room temperature circularly polarized lasing in an optically spin injected vertical-cavity surface-emitting laser with (110) GaAs quantum wells”, *Appl. Phys. Lett.* **98**, 081113 (2011).
- ³¹K. Schires, R. A. Seyab, A. Hurtado, V.-M. Korpijärvi, M. Guina, I. D. Henning, and M. J. Adams, “Optically-pumped dilute nitride spin-VCSEL”, *Opt. Express* **20**, 3550–3555 (2012).
- ³²J. Frougier, G. Baili, M. Alouini, I. Sagnes, H. Jaffrès, A. Garnache, C. Deranlot, D. Dolfi, and J.-M. George, “Control of light polarization using optically spin-injected vertical external cavity surface emitting lasers”, *Appl. Phys. Lett.* **103**, 252402, – (2013).
- ³³J. Frougier, “Towards spin-LED and spin-VECSEL operation at magnetic remanence”, PhD Thesis, Université Paris-Sud (2014).
- ³⁴A. Joly, G. Baili, M. Alouini, J.-M. George, I. Sagnes, G. Pillet, and D. Dolfi, “Compensation of the residual linear anisotropy of phase in a vertical-external-cavity-surface-emitting laser for spin injection”, *Opt. Lett.* **42**, 651–654 (2017).
- ³⁵M. Dyakonov and V. Perel, “Chapter 2 - theory of optical spin orientation of electrons and nuclei in semiconductors”, in *Optical orientation*, Vol. 8, edited by F. Meier and B. Zakharchenya, Modern Problems in Condensed Matter Sciences (Elsevier, 1984), pp. 11–71.
- ³⁶M. San Miguel, Q. Feng, and J. V. Moloney, “Light-polarization dynamics in surface-emitting semiconductor lasers”, *Phys. Rev. A* **52**, 1728–1739 (1995).
- ³⁷T. Fördös, H. Jaffrès, K. Postava, M. Seghilani, A. Garnache, J. Pištora, and H.-J. Drouhin, “Eigenmodes of spin vertical-cavity surface-emitting lasers with local linear birefringence and gain dichroism”, *Phys. Rev. A* **96**, 043828 (2017).

- ³⁸J.-L. Yu, Y.-H. Chen, C.-G. Tang, C. Jiang, and X.-L. Ye, “Observation of strong anisotropic forbidden transitions in (001) InGaAs/GaAs single-quantum well by reflectance-difference spectroscopy and its behavior under uniaxial strain”, *Nanoscale Res. Lett.* **6**, 210 (2011).
- ³⁹O. Krebs and P. Voisin, “Giant optical anisotropy of semiconductor heterostructures with no common atom and the quantum-confined pockels effect”, *Phys. Rev. Lett.* **77**, 1829–1832 (1996).
- ⁴⁰T. Fördös, K. Postava, H. Jaffrès, and J. Pištora, “Matrix approach for modeling of emission from multilayer spin-polarized light-emitting diodes and lasers”, *J. Opt.* **16**, 065008 (2014).
- ⁴¹S. Cortez, O. Krebs, and P. Voisin, “Breakdown of rotational symmetry at semiconductor interfaces: a microscopic description of valence subband mixing”, *The Europ. Phys. J. B - Cond. Matter Compl. Syst.* **21**, 241–250 (2001).
- ⁴²L. F. Lastras-Martínez, R. E. Balderas-Navarro, A Lastras-Martínez, and K Hingerl, “Stress-induced optical anisotropies measured by modulated reflectance”, *Semicond. Sci. Tech.* **19**, R35 (2004).
- ⁴³T. Fördös, K. Postava, H. Jaffrès, D. Quang To, J. Pištora, and H. J. Drouhin, “Mueller matrix ellipsometric study of multilayer spin-vsel structures with local optical anisotropy”, *Appl. Phys. Lett.* **112**, 221106 (2018).
- ⁴⁴M. Alouini, J. Frougier, A. Joly, G. Baili, D. Dolfi, and J.-M. George, “VSPIN: a new model relying on the vectorial description of the laser field for predicting the polarization dynamics of spin-injected V(e)CSELs”, *Opt. Express* **26**, 6739–6757 (2018).
- ⁴⁵K. Postava, T. Fördös, H. Jaffrès, L. Halagačka, H. J. Drouhin, and J. Pištora, “Modeling of anisotropic grating structures with active dipole layers”, *Proc. SPIE* **9516**, 95160OF (2015).
- ⁴⁶L. Coldren, S. Corzine, and M. Mashanovitch, *Diode lasers and photonic integrated circuits*, Wiley Series in Microwave and Optical Engineering (Wiley, 2012).
- ⁴⁷N. C. Gerhardt and M. R. Hofmann, “Spin-controlled vertical-cavity surface-emitting lasers”, *Advances in Optical Technologies* **2012**, 268949–15 (2012).
- ⁴⁸S. Pfalz, R. Winkler, T. Nowitzki, D. Reuter, A. D. Wieck, D. Hägele, and M. Oestreich, “Optical orientation of electron spins in gaas quantum wells”, *Phys. Rev. B* **71**, 165305 (2005).
- ⁴⁹G Schmidt, “Concepts for spin injection into semiconductors - a review”, *J. Phys. D: Appl. Phys.* **38**, R107 (2005).
- ⁵⁰V. F. Motsnyi, P. Van Dorpe, W. Van Roy, E. Goovaerts, V. I. Safarov, G. Borghs, and J. De Boeck, “Optical investigation of electrical spin injection into semiconductors”, *Phys. Rev. B* **68**, 245319 (2003).
- ⁵¹M Guina, A Rantamäki, and A Härkönen, “Optically pumped VECSELs: review of technology and progress”, *J. Phys. D: Appl. Phys.* **50**, 383001 (2017).

- ⁵²N. Basov, O. Bogdankevich, and A. Grasyuk, “Semiconductor lasers with radiating mirrors”, *IEEE J. Quantum Electron.* **2**, 594–597 (1966).
- ⁵³H. Q. Le, S. D. Cecca, and A. Mooradian, “Scalable high-power optically pumped GaAs laser”, *Appl. Phys. Lett.* **58**, 1967–1969 (1991).
- ⁵⁴M. Kuznetsov, F. Hakimi, R. Sprague, and A. Mooradian, “High-power (>0.5 -w cw) diode-pumped vertical-external-cavity surface-emitting semiconductor lasers with circular TEM₀₀ beams”, **9**, 1063–1065 (1997).
- ⁵⁵J. Lee, R. Oszwaldowski, C. Gøthgen, “Mapping between quantum dot and quantum well lasers: from conventional to spin lasers”, *Phys. Rev. B* **85**, 045314 (2012).
- ⁵⁶I. Zutic and P. E. Faria Jr., “Taken for a spin”, *Nature Nanotechnology* **9** (2015).
- ⁵⁷J. Rudolph, D. Hägele, H. M. Gibbs, G. Khitrova, and M. Oestreich, “Laser threshold reduction in a spintronic device”, *Appl. Phys. Lett.* **82**, 4516–4518 (2003).
- ⁵⁸Š. Višňovský, “Magneto-optical permittivity tensor in crystals”, *Czech. J. Phys. B* **36**, 1424–1433 (1986).
- ⁵⁹M. Dyakonov, *Spin physics in semiconductors*, Springer Series in Solid-State Sciences (Springer International Publishing, 2017).
- ⁶⁰M. V. Durnev, M. M. Glazov, and E. L. Ivchenko, “Spin-orbit splitting of valence subbands in semiconductor nanostructures”, *Phys. Rev. B* **89**, 075430 (2014).
- ⁶¹E. L. Ivchenko, A. Y. Kaminski, and U. Rössler, “Heavy-light hole mixing at zinc-blende (001) interfaces under normal incidence”, *Phys. Rev. B* **54**, 5852–5859 (1996).
- ⁶²K. C. Hall, E. Altunkaya, W. H. Lau, M. E. Flatté, T. F. Boggess, J. J. Zinck, W. B. Barvosa-Carter, and S. L. Skeith, “Spin relaxation in (110) and (001) InAs/GaSb superlattices”, *Phys. Rev. B* **68**, 115311 (2003).
- ⁶³O. Krebs, P. Voisin, D. Rondi, J. Gentner, L. Goldstein, and J. Harmand, “Giant optical anisotropy in semiconductor heterostructures with no-common atom”, *Physica E: Low-dim. Sys. Nanostr.* **2**, 59–64 (1998).
- ⁶⁴O. Hunderi, J.-T. Zettler, and K. Haberland, “On the AlAs/GaAs (001) interface dielectric anisotropy”, *Thin Solid Films* **472**, 261–269 (2005).
- ⁶⁵J. van der Veen, P. Larsen, J. Neave, and B. Joyce, “The GaAs (001)-c(4x4) and (2x4) reconstructions: a comparative photoemission study”, *Solid State Communications* **49**, 659–662 (1984).
- ⁶⁶S. E. Acosta-Ortiz and A. Lastras-Martínez, “Electro-optic effects in the optical anisotropies of (001) GaAs”, *Phys. Rev. B* **40**, 1426–1429 (1989).
- ⁶⁷A. Yariv, *Optical electronics*, The Oxford Series in Electrical and Computer Engineering (Oxford University Press, 1990).
- ⁶⁸M. S. Park, B. T. Ahn, B.-S. Yoo, H. Y. Chu, H.-H. Park, and C. J. Chang-Hasnain, “Polarization control of vertical-cavity surface-emitting lasers by electro-optic birefringence”, *Appl. Phys. Lett.* **76**, 813–815 (2000).

- ⁶⁹J. Frougier, G. Baili, I. Sagnes, D. Dolfi, J.-M. George, and M. Alouini, “Accurate measurement of the residual birefringence in VECSEL: towards understanding of the polarization behavior under spin-polarized pumping”, *Opt. Express* **23**, 9573–9588 (2015).
- ⁷⁰M. Seghilani, “Highly coherent iii-v-semiconductor laser emitting phase-, amplitude- and polarization-structured light for advanced sensing applications: vortex, spin, feedback dynamics”, PhD Thesis, University of Montpellier (2016).
- ⁷¹S. Visnovsky, *Optics in magnetic multilayers and nanostructures*, Optical Science and Engineering (CRC Press, 2006).
- ⁷²B. Saleh and M. Teich, *Fundamentals of photonics*, Wiley Series in Pure and Applied Optics (Wiley, 2007).
- ⁷³M. Freiser, “A survey of magneto-optic effects”, *IEEE Transactions on Magnetics* **4**, 152–161 (1968).
- ⁷⁴R. M. A. Azzam and N. Bashara, *Ellipsometry and polarized light*, North-Holland personal library (North-Holland, 1987).
- ⁷⁵Š. Višňovský, “Magneto-optical ellipsometry”, *Czech. J. Phys. B* **36**, 625–650 (1986).
- ⁷⁶P. Yeh, “Electromagnetic propagation in birefringent layered media”, *J. Opt. Soc. Am.* **69**, 742–755 (1979).
- ⁷⁷D. Aspnes and A. Frova, “Influence of spatially dependent perturbations on modulated reflectance and absorption of solids”, *Solid State Communications* **7**, 155–159 (1969).
- ⁷⁸L. F. Lastras-Martínez, D. Rönnow, P. V. Santos, M. Cardona, and K. Eberl, “Optical anisotropy of (001)-GaAs surface quantum wells”, *Phys. Rev. B* **64**, 245303 (2001).
- ⁷⁹H. Fujiwara, *Spectroscopic ellipsometry: principles and applications* (Wiley, 2007).
- ⁸⁰J. Lee, J. Koh, and R. W. Collins, “Multichannel mueller matrix ellipsometer for real-time spectroscopy of anisotropic surfaces and films”, *Opt. Lett.* **25**, 1573–1575 (2000).
- ⁸¹P. Weightman, D. S. Martin, R. J. Cole, and T. Farrell, “Reflection anisotropy spectroscopy”, *Rep. Prog. Phys.* **68**, 1251 (2005).
- ⁸²D. E. Aspnes, “Above-bandgap optical anisotropies in cubic semiconductors: a visible-near ultraviolet probe of surfaces”, *J. Vac. Sci. Technol.* **3**, 1498–1506 (1985).
- ⁸³E. Garcia-Caurel, A. De Martino, J.-P. Gaston, and L. Yan, “Application of Spectroscopic Ellipsometry and Mueller Ellipsometry to Optical Characterization”, *Appl. Spectrosc.* **67**, 1–21 (2013).
- ⁸⁴R. W. Collins and J. Koh, “Dual rotating-compensator multichannel ellipsometer: instrument design for real-time mueller matrix spectroscopy of surfaces and films”, *J. Opt. Soc. Am. A* **16**, 1997–2006 (1999).

- ⁸⁵G. E. Jellison Jr. and F. A. Modine, “Parameterization of the optical functions of amorphous materials in the interband region”, *Applied Physics Letters* **69**, 371–373 (1996).
- ⁸⁶B Johs, C. Herzinger, J. Dinan, A Cornfeld, and J. Benson, “Development of a parametric optical constant model for $\text{Hg}_{1-x}\text{Cd}_x\text{Te}$ for control of composition by spectroscopic ellipsometry during MBE growth”, *Thin Solid Films* **313-314**, 137–142 (1998).
- ⁸⁷D. W. Marquardt, “An algorithm for least-squares estimation of nonlinear parameters”, *SIAM Journal on Applied Mathematics* **11**, 431–441 (1963).
- ⁸⁸E. D. Palik, ed., *Handbook of optical constants of solids I, II, III* (Academic Press, 1991).
- ⁸⁹M. Bass, C. DeCusatis, J. Enoch, V. Lakshminarayanan, G. Li, C. MacDonald, V. Mahajan, and E. Van Stryland, *Handbook of optics, third edition volume iv: optical properties of materials, nonlinear optics, quantum optics (set)*, *Handbook of Optics* (McGraw-Hill Education, 2009).
- ⁹⁰S. Zollner, “Model dielectric functions for native oxides on compound semiconductors”, *Appl. Phys. Lett.* **63**, 2523–2524 (1993).
- ⁹¹M. Losurdo and K. Hingerl, *Ellipsometry at the nanoscale* (Springer Berlin Heidelberg, 2013).
- ⁹²S. Adachi, *Optical properties of crystalline and amorphous semiconductors: materials and fundamental principles* (Springer US, 2012).
- ⁹³P. YU and M. Cardona, *Fundamentals of semiconductors: physics and materials properties* (Springer Berlin Heidelberg, 2013).
- ⁹⁴I. Khanin, *Fundamentals of laser dynamics* (Cambridge International Science Publishing, 2006).
- ⁹⁵G. Agrawal, “Gain nonlinearities in semiconductor lasers: theory and application to distributed feedback lasers”, *IEEE J. Quantum Electron.* **23**, 860–868 (1987).
- ⁹⁶S. E. Hodges, M. Munroe, J. Cooper, and M. G. Raymer, “Multimode laser model with coupled cavities and quantum noise”, *J. Opt. Soc. Am. B* **14**, 191–199 (1997).
- ⁹⁷J. Martin-Regalado, F. Prati, M. S. Miguel, and N. B. Abraham, “Polarization properties of vertical-cavity surface-emitting lasers”, *IEEE J. Quantum Electron.* **33**, 765–783 (1997).
- ⁹⁸L. Lugiato, F. Prati, and M. Brambilla, *Nonlinear optical systems* (Cambridge University Press, 2015).
- ⁹⁹H. E. Türeci, A. D. Stone, and B. Collier, “Self-consistent multimode lasing theory for complex or random lasing media”, *Phys. Rev. A* **74**, 043822 (2006).

- ¹⁰⁰M. Y. Li, H. Jähme, H. Soldat, N. C. Gerhardt, M. R. Hofmann, and T. Ackemann, “Birefringence controlled room-temperature picosecond spin dynamics close to the threshold of vertical-cavity surface-emitting laser devices”, *Ultrafast spin-induced polarization oscillations with tunable lifetime in vertical-cavity surface-emitting lasers* **97**, 191114 (2010).
- ¹⁰¹H. Fu and H. Haken, “Multifrequency operations in a short-cavity standing-wave laser”, *Phys. Rev. A* **43**, 2446–2454 (1991).
- ¹⁰²A. Cerjan, Y. Chong, L. Ge, and A. D. Stone, “Steady-state ab initio laser theory for n-level lasers”, *Opt. Express* **20**, 474–488 (2012).
- ¹⁰³A. Cerjan, Y. D. Chong, and A. D. Stone, “Steady-state ab initio laser theory for complex gain media”, *Opt. Express* **23**, 6455–6477 (2015).
- ¹⁰⁴A. Fiore and A. Markus, “Differential gain and gain compression in quantum-dot lasers”, *IEEE J. Quantum Electron.* **43**, 287–294 (2007).
- ¹⁰⁵C. Gothgen, R. Oszwaldowski, A. Petrou, and I. Zutic, “Analytical model of spin-polarized semiconductor lasers”, *Appl. Phys. Lett.* **93**, 042513 (2008).
- ¹⁰⁶J. Lee, W. Falls, R. Oszwaldowski, and I. Zutic, “Spin modulation in semiconductor lasers”, *Appl. Phys. Lett.* **97**, 041116, 041116 (2010).
- ¹⁰⁷G. J. de Valcarcel, E. Roldan, and F. Prati, “Semiclassical theory of amplification and lasing”, PhD Thesis, Universite Paris-Sud **52**, 198–214 (2006).
- ¹⁰⁸H. Breuer and F. Petruccione, *The theory of open quantum systems* (Oxford University Press, 2002).
- ¹⁰⁹W. Chow and S. Koch, *Semiconductor-laser fundamentals: physics of the gain materials* (Springer Berlin Heidelberg, 1999).
- ¹¹⁰A. Gahl, S. Balle, and M. S. Miguel, “Polarization dynamics of optically pumped VCSELs”, *IEEE J. Quantum Electron.* **35**, 342–351 (1999).
- ¹¹¹F. Bretenaker and A. Le Floch, “Laser eigenstates in the framework of a spatially generalized Jones matrix formalism”, *J. Opt. Soc. Am. B* **8**, 230–238 (1991).
- ¹¹²A. E. Siegman, *Lasers* (University Science Books, Mill Valley, CA, United States, 1986).
- ¹¹³P. E. Faria Jr., G. Xu, J. Lee, N. C. Gerhardt, G. M. Sipahi, “Toward high-frequency operation of spin lasers”, *Phys. Rev. B* **92**, 075311 (2015).
- ¹¹⁴C. Henry, “Theory of the linewidth of semiconductor lasers”, *IEEE J. Quantum Electron.* **18**, 259–264 (1982).
- ¹¹⁵S. Balle, “Simple analytical approximations for the gain and refractive index spectra in quantum-well lasers”, *Phys. Rev. A* **57**, 1304–1312 (1998).
- ¹¹⁶G. Baili, L. Morvan, M. Alouini, D. Dolfi, F. Bretenaker, I. Sagnes, and A. Garnache, “Experimental demonstration of a tunable dual-frequency semiconductor laser free of relaxation oscillations”, *Opt. Lett.* **34**, 3421–3423 (2009).

- ¹¹⁷S. De, A. E. Amili, I. Fsaifes, G. Pillet, G. Baili, F. Goldfarb, M. Alouini, I. Sagnes, and F. Bretenaker, “Phase noise of the radio frequency (RF) beatnote generated by a dual-frequency VECSEL”, *J. Light. Techn.* **32**, 1307–1316 (2014).
- ¹¹⁸S. De, G. Baili, S. Bouchoule, M. Alouini, and F. Bretenaker, “Intensity-and phase-noise correlations in a dual-frequency vertical-external-cavity surface-emitting laser operating at telecom wavelength”, *Phys. Rev. A* **91**, 053828 (2015).
- ¹¹⁹M. Sargent, M. Scully, and W. Lamb, *Laser physics*, Advanced book program (Westview Press, Boulder, CO, United States, 1978).
- ¹²⁰A. Garnache, B. Sermage, R. Teissier, G. Saint-Giro, and I. Sagnes, “A new kind of fast quantum-well semiconductor saturable-absorber mirror with low losses for ps pulse generation”, in *International conference on Indium Phosphide and related materials*, 2003. (2003), pp. 247–250.
- ¹²¹M. Travagnin, M. P. van Exter, A. K. Jansen van Doorn, and J. P. Woerdman, “Erratum: role of optical anisotropies in the polarization properties of surface-emitting semiconductor lasers [phys. rev. a **54** , 1647 (1996)]”, *Phys. Rev. A* **55**, 4641–4641 (1997).
- ¹²²M Herms, M Fukuzawa, V. Melov, J Schreiber, P Mock, and M Yamada, “Residual strain in annealed GaAs single-crystal wafers as determined by scanning infrared polariscopy, X-ray diffraction and topography”, *Journal of Crystal Growth* **210** (2000).
- ¹²³O Krebs, W Seidel, J. P. André, D Bertho, C Jouanin, and P Voisin, “Investigations of giant ‘forbidden’ optical anisotropy in GaInAs - InP quantum well structures”, *Semicond. Sci. Technol.* **12**, 938 (1997).
- ¹²⁴S. Cortez, O. Krebs, and P. Voisin, “In-plane optical anisotropy of quantum well structures: from fundamental considerations to interface characterization and optoelectronic engineering”, *J. Vac. Sci. Tech. B* **18**, 2232–2241 (2000).
- ¹²⁵E. A. Cerda-Méndez, R. E. Balderas-Navarro, A. Lastras-Martínez, L. F. Lastras-Martínez, A. Garnache, L. Cerutti, and A. Jouillé, “Interfaces in $\text{Ga}_x\text{In}_{1-x}\text{As}_y\text{Sb}_{1-y}\text{Al}_x\text{Ga}_{1-x}\text{As}_y\text{Sb}_{1-y}$ multi-quantum-well heterostructures probed by transmittance anisotropy spectroscopy”, *J. Appl. Phys.* **98**, 066107 (2005).
- ¹²⁶H. Shen, M. Wraback, J. Pamulapati, P. G. Newman, M. Dutta, Y. Lu, and H. C. Kuo, “Optical anisotropy in GaAs/ $\text{Al}_x\text{Ga}_{1-x}\text{As}$ multiple quantum wells under thermally induced uniaxial strain”, *Phys. Rev. B* **47**, 13933–13936 (1993).
- ¹²⁷D. J. English, P. G. Lagoudakis, R. T. Harley, P. S. Eldridge, J. Hübner, and M. Oestreich, “Strain-induced spin relaxation anisotropy in symmetric (001)-oriented GaAs quantum wells”, *Phys. Rev. B* **84**, 155323 (2011).
- ¹²⁸H. Benisty, R. Stanley, and M. Mayer, “Method of source terms for dipole emission modification in modes of arbitrary planar structures”, *J. Opt. Soc. Am. A* **15**, 1192–1201 (1998).

- ¹²⁹Š. Višňovský, M. Nývlt, V. Pařízek, P. Kielar, V. Prosser, and R. Krishnan, “Magneto-optical studies of Pt/Co multilayers and Pt-Co alloy thin films”, IEEE Trans. Magn. **29**, 3390–3392 (1993).
- ¹³⁰R. Jansen, B. C. Min, S. P. Dash, S. Sharma, G. Kioseoglou, A. T. Hanbicki, O. M. J. van ’t Erve, P. E. Thompson, and B. T. Jonker, “Electrical spin injection into moderately doped silicon enabled by tailored interfaces”, Phys. Rev. B **82**, 241305 (2010).
- ¹³¹B. T. Jonker, G. Kioseoglou, A. T. Hanbicki, C. H. Li, and P. E. Thompson, “Electrical spin-injection into silicon from a ferromagnetic metal/tunnel barrier contact”, Nat Phys **3**, 542–546 (2007).
- ¹³²P. B. Johnson and R. W. Christy, “Optical constants of transition metals: Ti, V, Cr, Mn, Fe, Co, Ni, and Pd”, Phys. Rev. B **9**, 5056–5070 (1974).
- ¹³³A. Garnache, A. Ouvrard, L. Cerutti, D. Barat, A. Vicet, F. Genty, Y. Rouillard, D. Romanini, and E. A. Cerda-Mendez, *2-2.7 m single frequency tunable sb-based lasers operating in CW at RT: microcavity and external cavity vcsels, dfb*, 2006.
- ¹³⁴A. Garnache, A. Ouvrard, and D. Romanini, “Single-frequency operation of external-cavity VCSELs: non-linear multimode temporal dynamics and quantum limit”, Opt. Express **15**, 9403–9417 (2007).
- ¹³⁵A. Laurain, M. Myara, G. Beaudoin, I. Sagnes, and A. Garnache, “Multiwatt-power highly-coherent compact single-frequency tunable vertical-external-cavity-surface-emitting-semiconductor-laser”, Opt. Express **18**, 14627–14636 (2010).
- ¹³⁶M. Sondermann, M. Weinkath, and T. Ackemann, “Polarization switching to the gain disfavored mode in vertical-cavity surface-emitting lasers”, IEEE J. Quant. Electr. **40**, 97–104 (2004).
- ¹³⁷M. Schubert, V. Gottschalch, C. M. Herzinger, H. Yao, P. G. Snyder, and J. A. Woollam, “Optical constants of Ga(x)In(1-x)P lattice matched to GaAs”, J. Appl. Phys. **77**, 3416–3419 (1995).

Title : Coherent light source with spin polarized current

Keywords : spin-lasers, VCSELs, Mueller matrix ellipsometry

Résumé : Spin-lasers are semiconductor devices in which the radiative recombination processes involving spin-polarized carriers result in an emission of circularly polarized photons. Nevertheless, additional linear in-plane anisotropies in the cavity generally lead in preferential linearly-polarized laser emission and to possible coupling between modes. In this thesis, a general method for the modeling of semiconductor laser such as vertical-(external)-cavity surface-emitting laser containing multiple quantum wells and involving anisotropies that may reveal *i)* a local linear birefringence due to the strain field at the surface or *ii)* a birefringence in quantum wells (QWs) due to phase amplitude coupling originating from the reduction of the biaxial D_{2d} to the C_{2v} symmetry group at the III-V ternary semiconductor interfaces. A novel scattering S-matrix recursive method is implemented using a gain tensor derived analytically from the Maxwell-Bloch equations. It enables to model the properties of

the emission (threshold, polarization, mode splitting) from the laser with multiple quantum well active zones by searching for the resonant eigenmodes of the cavity. The method is demonstrated on real laser structures and is used for the extraction of optical permittivity tensors of surface strain and quantum wells in agreement with experiments. The method is generalized to find the laser eigenmodes in the most general case of circular polarized pumps (unbalance between the spin-up and spin-down channels) and linear gain dichroism. In addition, the measurement of full 4×4 Mueller matrix for multiple angles of incidence and in-plane azimuthal angles has been used for extraction of optical permittivity tensors of surface strained layers and quantum wells. Such spectral dependence of optical tensor elements are crucial for modeling of spin-laser eigenmodes, resonance conditions, and also for understanding of sources of structure anisotropies.

Titre : Source de lumière cohérente avec courant polarisé en spin

Mots clefs : spin-lasers, VCSEL, ellipsométrie de la matrice de Mueller

Abstract : Les spin-lasers sont des dispositifs semi-conducteurs dans lesquels les processus de recombinaison radiative impliquant des porteurs polarisés en spin résultent en une émission de photons polarisés circulairement. Néanmoins, des anisotropies linéaires supplémentaires dans la cavité conduisent généralement à une émission laser préférentiellement polarisée linéairement et à un éventuel couplage entre modes. Dans cette thèse, une méthode générale pour la modélisation de lasers à semi-conducteurs tels que laser à surface verticale (externe) à cavité et contenant des puits quantiques multiples et impliquant des anisotropies pouvant révéler (i) une biréfringence linéaire locale due au champ de déformation à la surface ou (ii) une biréfringence dans les puits quantiques due au couplage d'amplitude de phase provenant de la réduction du D_{2d} biaxial au groupe de symétrie C_{2v} aux interfaces semiconductrices ternaires III-V. Une nouvelle méthode récursive à matrice S de diffusion est mise en oeuvre en utilisant un tenseur de gain d'érivé analytiquement des équations de Maxwell-Bloch. Il permet de modéliser les propriétés de

l'émission (seuil, polarisation, dédoublement de mode) du laser avec plusieurs zones actives à puits quantiques en recherchant les modes propres résonnants de la cavité. La méthode est démontrée sur des structures laser réelles et est utilisée pour l'extraction de tenseurs de permittivité optique de déformation de surface et de puits quantiques en accord avec des expériences. La méthode est généralisée pour trouver les modes propres au laser dans le cas le plus général des pompes polarisées circulaires (déséquilibre entre les canaux de spin-up et de spin-down) et le dichroïsme à gain linéaire. De plus, la mesure de la matrice de Mueller 4×4 complète pour des angles d'incidence multiples et des angles azimutaux dans le plan a été utilisée pour l'extraction de tenseurs de permittivité optique de couches contraintes superficielles et de puits quantiques. Une telle dépendance spectrale des éléments tensoriels optiques est cruciale pour la modélisation des modes propres du laser de spin, les conditions de résonance, et aussi pour la compréhension des sources d'anisotropies de structure.